Swimming and Swarming of Self-Propelled Particles

Inaugural-Dissertation

zur

Erlangung des Doktorgrades

der Mathematisch-Naturwissenschaftlichen Fakultät

der Universität zu Köln

vorgelegt von

Yingzi Yang

aus Shanghai, China

Köln

2009

Berichterstatter: Prof. Dr. Gerhard Gompper
Prof. Dr. U. Benjamin Kaupp

Tag der letzten mündlichen Prüfung: 10. 08. 2009

Contents

Abstract

A number of micro-organisms and cells, such as sperm and some spieces of roundworms (nematodes), employ a sinusoidal beating motion of their rod-like body to swim though a fluid medium. For the motion of these microscopic swimmers, the viscosity is dominating and the inertia is negligible. They cooperate with each other through hydrodynamic interactions and exhibit complex swarm behaviors, such as aggregation near surfaces and clustering at high density. These interesting and surprising phenomena indicate that, in addition to the individual motion of wandering and struggling alone, there are more efficient cooperative ways for the swimmers to overcome long distance and obstacles to reach their ultimate goal. This applies especially for sperm as one of the most important cells for the reproduction of high animals.

The goal of this work is to explain the importance of hydrodynamic interaction and volume exclusion for the cooperation and swarm behavior of micro-swimmers which employ sinusoidal beating, like sperm and nematodes. We classify the swimmers as rod-like self-propelled particles (rSPP) in a viscous environment, and compare the swarm behaviors of straight self-propelled rods and sinusoidal beating swimmers by simulations. The hydrodynamic interaction between the swimmers is simulated by multi-particle collision dynamics (MPC), a particle-based meso-scopic simulation method for fluid dynamics. We also perform the simulations with anisotropic frictions (AF), an approximation of hydrodynamics, which neglects hydrodynamic interactions between swimmers. The contributions of hydrodynamic interaction and volume exclusion are distinguished by comparing results in a MPC fluid and with AF.

Sperm and nematodes in experiments usually swim in a quasi-two-dimensional space due to the aggregation at the surfaces. Furthermore, from a simulation viewpoint, sperm swimming in a two-dimensional fluid is a less demanding problem than in three dimensions, so that cooperative behaviors can be studied in much more detail. Thus we focus on simulations in two dimensions.

Volume exclusion of the elongated particles is the key factor to induce the alignment and clustering behavior of self-propelled rods in viscous environment in two dimensions. Two kinds of clusters are found: motile clusters with all of their components polarized, which are found for low rod density and strong environmental noise; giant, immobile clusters of blocked rods, which are found for high rod density and weak environmental noise. A stable distribution function of cluster size is reached when the system is balanced between the formation rate and break-up rate. Three types of the distribution functions, corresponding to three states of the system, are

found. For systems of motile clusters, the distribution function always has a power-law-decay part. The average cluster size shows a power-law relation with the variance of environmental noise. Giant density fluctuations, which are a characteristic fingerprint of aggregating systems of self-propelled particles, are also found in our rod simulations.

The main difference between self-propelled rods and flagella systems is that the sinusoidal beating flagella have synchronization and attraction through hydrodynamic interaction. The hydrodynamic synchronization and attraction make the flagella in the same cluster tightly packed and locked in phase. The clusters extend strongly in the direction of motion, and the probability to find small clusters is decreased. Hydrodynamic interaction between clusters acts as the environmental background noise. The swarm behavior of sinusoidal undulating flagella is basically the same as the self-propelled rods. The distribution function of cluster size has a power-law decay. In nature, sperm and nematodes can have a wide distribution of beat frequencies, which can be considered as noise due to internal property. The average cluster size has a power-law dependence on the variance of distribution of beating frequencies.

A sperm is a sinusoidal beating flagellum with a head attached in front. Although the heads generate strong viscous resistance, the hydrodynamic interaction - synchronization and attraction - between beating tails is still dominating. The swarming behavior of a multi-sperm system is the same as a multi-flagellum system. However, the heads make the cluster configuration much looser, thus the stability of large clusters decreases.

Thus we conclude that, in two dimensions, the fundamental elements for the swarming behavior of active rod-like particles like sperm and nematodes are the anisotropic shape and the self-propelled motion. The volume exclusion is a strong mechanism to induce the alignment. The hydrodynamic interaction due to the sinusoidal beating motion regulates the shape of the clusters and the distribution function of cluster size.

In three dimensions, the hydrodynamic interaction is still strong enough to make cooperating clusters of flagella or sperm. The flagella can get synchronized through different pathways - shifting the relative position, or rotating their beating planes. However, the cooperation in three dimensions is not as stable as in two dimensions.

Our results are in good agreements with experimental observations of the swarming of sperm and nematodes in a thin layer of fluid medium near surfaces. Interesting experimental phenomena, such as the elongated cluster of rodent sperm and the vortices of sea-urchin sperm, are reproduced in the simulations.

I. Introduction

1.1 Motivation

Swimming is the active motion of a body in a fluid. Most familiar to us is the swimming of humans on the surface of water, like in a swimming pool. In human swimming, inertia is very important. We push back the water with our arms, and then glide through the water for a while. This inertia effect can be seen very clearly in even larger objects, e.g. a ship continuous to float for a large distance after its engine stops. With increasing fluid viscosity, decreasing swimming velocity, or decreasing size of the swimmer, the viscous forces become more and more important. Imagine a human swimming in honey, where the viscosity is much higher than in water. The motion immediately stops when his arms stop waving.

Studies of swimmers at the length scale of micrometers, such as sperm and bacteria, have profound biological importance. Sperm use a beating flagellum several-ten micrometers long to swim towards the egg. The flagellum has a rod-like structure and pushes the surrounding fluid backwards by a snake-like motion. The flagella of some bacteria are several micrometers long and have a helix structure. The bacteria rotate their flagella as screw propellers to swim through a fluid to find food. Both sperm and bacteria swim in a fluid environment where viscosity is dominant and inertia is negligible [1]. If they stop their propelling motion, the swimming velocity vanishes at the time scale of microseconds [2].

Swimmers propel the surrounding fluids backwards to gain a forward motion. Through the flow field created by it, the swimmer interacts with other particles in the fluid. For example, you feel a strong water flow in the swimming pool when a swimming person passes by. This interaction is called hydrodynamic interaction. Hydrodynamic interaction is significant when the separating distance of two micro-swimmers is comparable to their typical size [3]. For example, experimental observations of two paramecium cells have shown that the changes in the direction of motion between two cells are induced mainly by hydrodynamic forces [4]. The hydrodynamic interaction between two bacterial flagella, has been investigated both experimentally [5] and theoretically [6][7]. For the bacteria using rotating helical flagella, such as *E. coli*, each cell typically has several flagella, which bundle or disperse depending on the sense of motor rotation. The bundling of the bacterial flagella is arising from the interplay of hydrodynamic interactions, and its rate is determined mainly by the rotating period.

Computer simulations have been employed to study the motion of microswimmer models [8], as well as the hydrodynamic interactions between two swimmers [9].

Even studies of a minimal swimming model of three linearly connected spheres [10] show a complex cooperative behavior [11]. The swimmer-swimmer interaction is a complicated function of their relative displacement, orientation and phase, leading to motion that can be attractive, repulsive, or oscillatory. However, despite the considerable progress in modeling elementary structures of those swimmers and the behavior of a single one in a fluid medium [12][13][14], relatively few theoretical studies have examined the hydrodynamic interaction of swimmers with other mesoscopic or macroscopic objects, e.g., the coordinated beating motions of two flagella [15][16], the tendency of accumulation near substrates [17][18][19][20], etc.

Collective behavior, also called swarm behavior, means the way in which an individual unit's activity is coordinated with its neighbors so that all units simultaneously alter their behavior to a common pattern [21]. Swarm behavior is common in nature, such as the group activities of humans, the collectively migration of birds, and the swirling of a fish school. Quite a few cells and organisms on different size scale, such as nematodes (roundworms) and sperm, exhibit similar swarm behavior when their local concentration is high. In experiments, they aggregate at the surfaces and form motile clusters consisting of a large number of individuals with coordinated movements [12][22][23]. Sperm and nematodes have a similar self-propelling mechanism. They employ a snake-like motion to push backwards the surrounding fluid, thus the bodies move forwards. Their aggregation and clustering behaviors correspond to the swarm behavior of self-propelled-rod systems. However, although the phase transition and cluster size distributions for the self-propelled-rod systems have been observed theoretically [24][25], a detailed understanding is still lacking. On the other hand, the distance between individuals in the same cluster is small, thus hydrodynamic interaction plays an important role in aggregation and clustering behavior. The effect of hydrodynamic interaction on the swarm behavior of self-propelled rods [26] was suggested to be important to adjust the orientation of rods. However, the interesting swarm behavior of dense systems of swimmers with hydrodynamic coupling remains to be explored.

1.2 Sperm

Sperm is one of the most important cells for the reproduction of high plants and animals. Their motility is crucial to fertilization. When released, sperm usually have to overcome a large distance compared with their own length before they find the egg. Organisms such as sea urchins that utilize external fertilization, in which egg and sperm cells are released into the surrounding water, demand high swimming efficiency. By contrast, for organisms employing internal fertilization, sperm have to travel much shorter distances but in a much rougher environment with high viscosity

and diverse obstacles. After the exhausting marathon, only a very small fraction of the initial huge number of sperm can reach the egg for fertilization. For the human case, only 300-500 from one injection of 200-300 million sperm will reach the egg at last. The others get lost or died on the way. Thus, the most healthy and energetic sperm are selected and their genes are passed on to the next generation.

1.2.1   High animal sperm structure

Although different from species to species, the basic structure of high animal sperm is quite universal. Usually, sperm of high animal consists of three parts: a head, a beating long tail, and a mid-piece to connect head and tail. Fig. 1.1 illustrates the structure of a human sperm as an example.

The sperm is characterized by a minimum of cytoplasm and the most densely packed DNA. The head part of sperm contains all genetic information to be passed ib to the next generation. Usually the head has a larger diameter than the cross section of the tail, and is covered by a cell membrane rich of membrane proteins for different functions. The head generates viscous resistance when the sperm moves forwards. The shape of the head is not a perfect sphere (see the illustration for human sperm in Fig. 1.1a and rodent sperm in Fig. 1.2a). The anisotropic shape of the head may lead to hydrodynamic effects modifying the swimming trajectories or special functions for the fertilization purpose. The diameter of the head is several micrometers, typically about 1/10 of the total length of the sperm. For example, the head of sea urchin sperm is about 3μm long and 1μm thick [27], while the total sperm length is 50μm. For human sperm, the cell consists of a 5μm by 3μm head and a 50μm tail.

The tail flagellum is the most important part for the motion of sperm. The tail has an axoneme in its center. For most of sperm, the axoneme has a "9+2" structure, which means two central microtubules (stiff polymers, the "bone" of the cytoskeleton) are surrounded by 9 double microtubules as illustrated in Fig. 1.1b. The microtubules are long and stiff polymers which form the backbone of the axoneme. They consist of tubulin monomers that are arranged in a helix to form a hollow tube. The microtubules of the axoneme are connected by motor proteins (dyneins) consume ATP to move along the microtubules. They are the most important active component to generate local bending of axoneme and thereby induce the active beating motion. The other structure elements, such as radial spokes and nexus, are different classes of proteins to regulate the pattern of the beat. The axoneme of the tail is covered with a cell membrane and is decorated with a lot of different functional proteins. Those proteins not only act as ion channels or chemical receptors, but also change the rigidity of the tail. The rigidity is important to the beating pattern of flagella in a viscoelastic media [28].
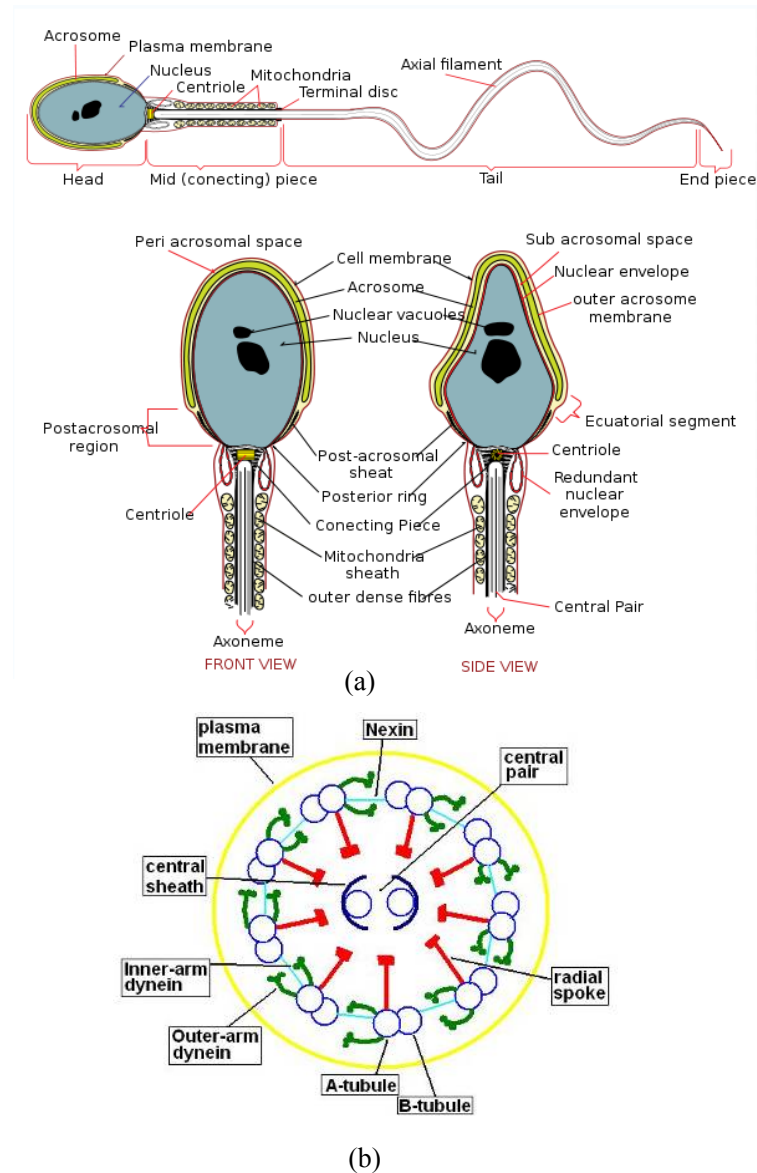
Figure 1.1: (a) Diagram of human sperm. (b) Diagram of "9+2" structure of axoneme. From Wikipedia.org.

The mid-piece of sperm, illustrated in Fig. 1.1a, has an axoneme as the center part. The axoneme of mid-piece is covered with mitochondria sheath and dense fibres. The mid-piece is quite rigid and not actively beating although it has the same axoneme structure as the tail.

1.2.2   Hydrodynamics of sperm

Sperm are swimming in a low Reynolds number fluid environment where the viscosity is dominating and inertia is negligible [1]. A dimensionless number, the Reynolds number (Re = $\rho v l / \eta$) provides a measure of the ratio of inertial (ρv) and viscous (η/l) forces, where v is the fluid velocity, ρ is the fluid density, η is the dynamic viscosity of the fluid and l is a characteristic length scale of the system. In

the high Reynolds number region (Re>2×10^3), e.g. a person swimming in water (Re~10^6) and a large ocean ship (Re~10^9), the inertial force is dominant and flow is turbulent. In the low Reynolds number region (Re<<1), e.g. the sperm (Re~10^{-2}) and the bacteria (Re~10^{-5}) swimming in water, the viscous force dominates. The Reynolds number associated with sperm is on the order of 10^{-2}. Therefore, the sperm exhibit lamellar flow, and the inertial force is negligible.

In the past decades, the effort to quantitatively describe the fluid dynamics of sperm has been very successful [29][30]. For example, the swimming velocity of a sea-urchin sperm has been calculated by assuming a sine-shaped beat-pattern [29]. The hydrodynamics is approximated by two friction coefficients for a rod dragged parallel or perpendicular to its orientation. The friction coefficients are functions of the ratio of rod length and diameter. The average swimming speed is [29]

$$v = \frac{fb^2}{2\lambda}\left(1 + \frac{4\pi^2 b^2}{\lambda^2} - \sqrt{1 + \frac{2\pi^2 b^2}{\lambda^2}\frac{C_H}{n\lambda\gamma_\parallel}}\right)^{-1}$$

where f is the beating frequency, λ is the wave length, b is the amplitude of the beat, n is the number of waves present on the tail, C_H is the drag coefficient of the head, and $\gamma_\parallel$ is the friction coefficient parallel to the rod. The friction coefficient perpendicular to the rod is assumed to be twice the value of $\gamma_\parallel$, which corresponds to the limit of a long and thin rod. The speed is proportional to the beating frequency, and is a complicated function of λ and b. Due to the pre-defined shape assumed in the derivation, the fluid viscosity does not influence the swimming speed. The response
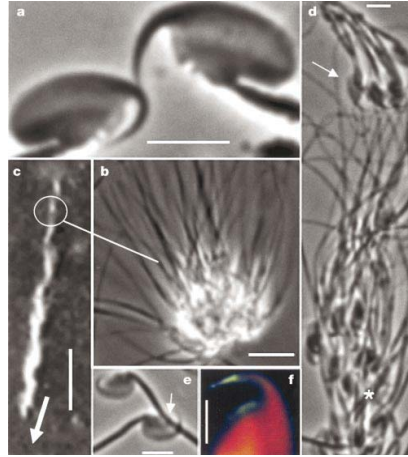
Figure 1.2: (a) the hook structure on head of rodent sperm. (b) Motile aggregation of approximately 50 sperm. (c) A large motile sperm train over 2-mm in length and consisting of thousands of sperm. (d) Image of formalin-fixed sperm from a train. (e) A sperm attached by the apical hook to the flagellum of another cell (indicated by an arrow). (f) Fluorescent immunolocalization of filamentous actin in the sperm head with propidium iodide counterstain. Actin was expressed in the apical hook region more intensely after deployment. Scale bars: a, d, e, f, 5μm; b, 10μm; c, 1mm. (cite from Ref. [23])

of the shape of the sperm tail to the viscous friction in 2D was also studied theoretically.

In a fluid medium, two obstacles at a distance can interact through hydrodynamic interactions. At low Reynolds numbers, hydrodynamic interactions in 3D are not negligible for two swimmers when the separating distance between them is less than 3-5 times their size [3]. In nature, the density of sperm can be extremely high. For example, one injection of human sperm has tens to one hundred million cells inside a small volume of 1cm^3. So the average distance between sperm is around 10μm while the length of sperm is 50μm. In experiments, sperm tend to accumulate at surfaces [17][18][19][20]. The sperm density at substrates is much higher than in the bulk. Thus, hydrodynamic interaction is important and must be taken into consideration for multi-sperm behavior.

The hydrodynamic interaction between sperm was noticed very early. Already in 1951, Taylor [16] has derived the hydrodynamic interaction at Re=0 between two sinusoidal undulating strings in 2D, which corresponds to infinitely large sheets in 3D. He demonstrated the hydrodynamic forces on undulating strings, which leads to phase locking and synchronized beating. The energy consumption decreases if two strings are synchronized and closer. Simulations of two sperm as well as two undulating strings in 2D [15][31] agree with Taylor's results. A strong correlation between sperm beating phase and relative sperm head position was found experimentally in self-organized sea-urchin vortices [32] (for more details see Section 1.2.3 below). This also reflects the "synchronization" effect through hydrodynamics. However, there is no systematic study of hydrodynamic interaction between sperm in 3D yet.

From experimental observations [17][19] and theoretical studies [18][20], sperm is known to have a strong aggregation tendency near substrates due to the self-propelled motion and the hydrodynamic interaction with the boundary. The beat mode is also influenced by the hydrodynamic interaction with the walls. The tail tends to beat parallel to the boundary.

1.2.3   Sperm cooperation in experiments

Sometimes, in order to conquer the tough swimming environment and blocking obstacles, sperm temporarily cooperate. Sperm from a single male have to compete with sperm from another male if present in the female reproductive tract at the same time. Close genetic relatedness predisposes individuals towards altruism, and as haploid sperm cells of an ejaculate will have genotypic similarity of 50%, it is predicted that sperm may display cooperation and altruism to gain an advantage when intermale sperm competition is intense [23][33]. The motile sperm could cooperate with one another through several possible interactions. The most fundamental
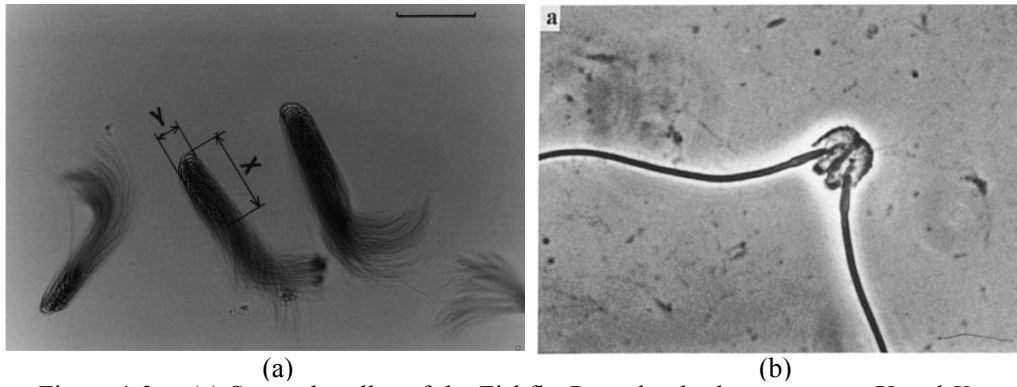
Figure 1.3:   (a) Sperm-bundles of the Fishfly *Parachauliodes japonicus*. X and *Y* are the maximum length and width of the head agglutination part. Scale bar is 0.1mm [35]. (b) Paired sperm of opossum *Monodelphis domestica*. Sperm heads are joined over their flat acrosomal surface to form a hydrodynamic biflagellate unit [37].

interaction is volume exclusion, because sperm cannot penetrate each other. Due to the short distance between two sperm, the hydrodynamic interaction is not negligible. Other possible interactions could be chemical bond connections and electrostatic interactions. Several examples of sperm cooperation have been reported in molluscs [34], insects [34][35][36] and wood mouse [22][23] experiments.

For wood mouse, multiple matings resulting in sperm competition and mixed paternity in littermates are believed to be widespread. In experiments [23], healthy and motile wood mouse sperm are released into an in vitro fertilization medium. Initially, the sperm are in single cell suspension, which means that they are separate in the fluid medium. Within 5 minutes, motile "trains" of sperm comprising hundreds to several thousand cells are formed, as shown in Fig. 1.2. The same experiment was done with different species of mouse sperm [22]. "An advantage in straight-line velocity does not hold in the house mouse where individual sperm were faster than sperm groups. It is possible that although the sperm groups in the house mouse are slower than individual sperm, they have greater thrust force."(From Ref. [22]) In European wood mouse, sperm "trains" exhibit increased thrust force in response to the gelatinous copulatory plugs left by males during copulation. In addition, the main function of a hook structure on the head of rodent sperm appears to be to maintain the stability of sperm groups rather than the actual attachment of sperm to each other [23].

The sperm clusters of fish fly [35] and the sperm pairs of opossum [37] have special agglutination between their heads. A fish-fly-sperm cluster has ten to hundred sperm sticking together at their heads, swimming with synchronized tails, as shown in Fig. 1.3. Two opossum sperm stick together at the flat surface of their heads and form a cooperating pair. The sperm pair has a more straight-forward trajectory than that of a single sperm. It can swim through a highly viscous fluid medium in which a single sperm is trapped locally and unable to escape.
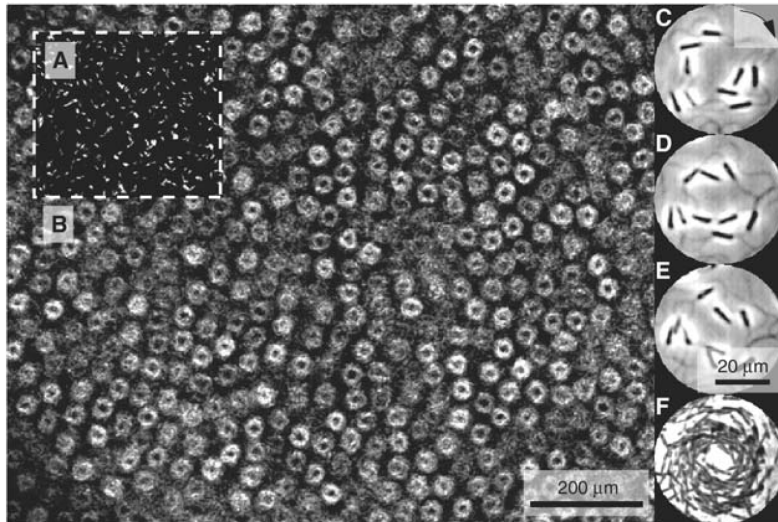
Figure 1.4: Circulating sea-urchin sperm form a 2D array of vortices [32]. (A) Single frame showing the heads of sperm at a surface density of 6000/mm^2. (B) The average intensity of 25 consecutive frames shows an arrangement of rings, each corresponding to a vortex of ~10 sperm. (C to E) Successive frames of a phase-contrast movie showing nine sperm swimming clockwise within a vortex.

A special experiment of cooperation of sea urchin sperm shows self-organized vortices with extremely high cell density near a substrate [32] (Fig. 1.4). The vortices emerge only when the sperm density at the substrate reaches a critical number of 2000/mm^2. In Fig. 1.4, each vortex contains 10±2 sperm, has the radius of 13.2±2.8μm, and diffuses randomly on the substrate. The swimming speed of sperm in the vortex is 125±21μm/s. If the sperm density is extremely high, the vortex density increases until the vortices are packed in a hexagonal array. Although the biological meaning of the vortices arrangement is not clear, at least the experiment indicates a very general interaction between sperm to build up cooperation – volume exclusion and hydrodynamic interactions.

1.3 Swarm behavior

Swarming is the collective motion of a large number of self-propelled agents. The interaction between two agents is simple, but the behavior of a lot of the same agents is complicated. Collective motion can be observed at almost every scale in nature, from human crowds [38][39][40] to fish schools, and unicellular organisms such as amoebae [41] and bacteria [42]. The system has neither an apparent leader, nor long-range communication between agents. However, although the specific biological details can be very different, there is a surprising amount of coordination among the agents in their collective motion.

For the last two decades, there has been a continuing interest in studying simple models to describe swarming. There are a lot of experimental [43][44][45], theoretical [33][46][47][48] and simulation [49][50][51][52][53][54][55][56][57][58] studies,

which analyzed different aspects of the swarm behavior such as orientation, aggregation and energy consumption. In experiments, self-propelled cells such as bacteria [42][59][60][61][62], sperm [22][32][35][36] and keratocyte cells [45] were used to study the swarming behavior on the length scale of micrometers. In simulations, the systems are drastically simplified to self-propelled particles with a defined neighborhood in which the average velocity affects the particle velocity towards alignment.

However, most of the simulations were done by assuming an artificial interaction between particle velocities. Thus the results depend strongly on the set of parameters like the radius of interaction region, and the strength of the interaction. In nature, the alignment mechanism for high animal swarms like fish schools or migratory birds is unknown, but the mechanism for some cells as *E. coli* and sperm is clearer. *Bacillus subtilis* and *E. coli* propel themselves through fluid and obviously the volume exclusion helps to align their directions [61][62]. In sperm experiments [22][32] and simulations [15][63], not only the volume exclusion, but also a hydrodynamic interaction between beating tails adjusts the swimming motion. Simulations of actin filaments on motor protein decorated substrates show that the filaments align and block movement by volume exclusion [64]. This shows the importance of volume exclusion for alignment. However, there are few studies of swarm behavior with volume exclusion induced alignment [25][52][53][64][65].

1.3.1   Swarm behavior of rod-like self-propelled particles

Microscopic organisms swimming in low-Reynolds-number environment are good examples for swarm behavior at small length scales. Those organisms are simple animals or single cells, thus their form of interaction is much simpler than the complex interactions between higher animals. Actively wiggling and self-propelled bacteria, such as *E. coli* and *B. subtilis* [42], show swarm behavior.

Myxobacteria [66] show a very interesting collective behavior. When starved, myxobacteria become elongated with an aspect ratio of approximately 1:7. They glide along the long axis and undergo a process of alignment, rippling, streaming, and aggregation that culminates in a three-dimensional fruiting body, as shown in Fig. 1.5a. The fruiting body formation in bacteria occurs in response to adverse conditions and is critical for species survival [67].

Sperm is another good example of self-propelled rod-like particles in a microscopic scale. When sperm have a high local density, they exhibit interesting cooperation, as introduced in Section 1.2.3. Other than the obvious chemical and electrostatic interactions in fish-fly and opossum sperm, the main aligning and aggregation origin of rodent sperm train and sea-urchin sperm vortices are simply
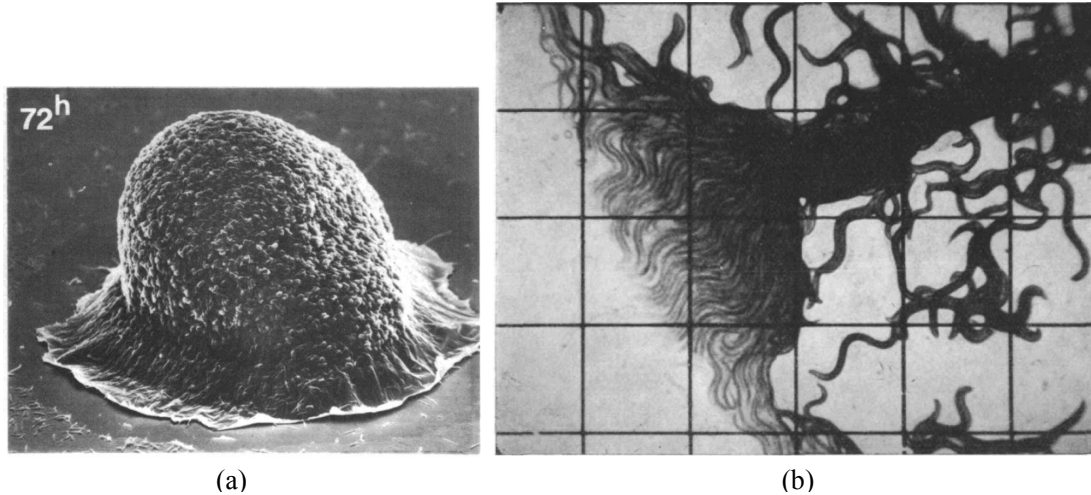
Figure 1.5: (a) A snapshot of the fruiting body of myxobacteria *M. Xanthus* [68]. (b) Co-ordinated movement of an aggregate of Panagrellus when on a damp surface of glass [12]. Scale 1mm.

volume exclusion and hydrodynamic interaction.

Nematodes, which are about 2mm long and propel themselves by a snake-like motion, show a similar swarm behavior as sperm do although they are much larger and swim at a higher Reynolds number of Re≈1. A remarkable tendency for a number of nematodes to adhere together in a thin film of water was found [12], as shown in Fig. 1.5b. When a culture of swimming nematodes is kept in a covered glass container, the animals creep at the walls and form large bundles extending to the boundary of damp region. Inside a bundle, the nematodes seem to have the same type of waves and move in phase with neighbors. The nematodes are moving in a thin layer of fluid at the surface, a quasi-two-dimensional condition, where volume exclusion plays a dominant role. Unfortunately, there is no systematic study of the swarm behavior of nematodes. It is unclear if there is any other interaction like chemical signal or inner mechanism to attune the beat motion for the worms to achieve coordinated movement.

An interesting experiment to study the swarm behavior of propelled rods was designed in Ref. [44]. Copper rods of 4.6mm length and 0.8mm diameter are confined between two hard substrates to form a quasi-two-dimensional space. The driven motion of the rods is introduced by a vibrating external magnetic field. Different from sperm and nematodes, the copper granules do not have a preferred propagating direction. They randomly move forwards or backwards along their extended direction. However, they still exhibit fundamental swarm properties such as giant density fluctuations (see Fig. 1.6). Here, giant density fluctuations are character by a variance ΔN of particle number fluctuations in a given area

$$\Delta N \sim N^{\beta_{\text{dens}}}$$

with $0.5 < \beta_{\text{dens}} < 1$, where N is the average particle number.
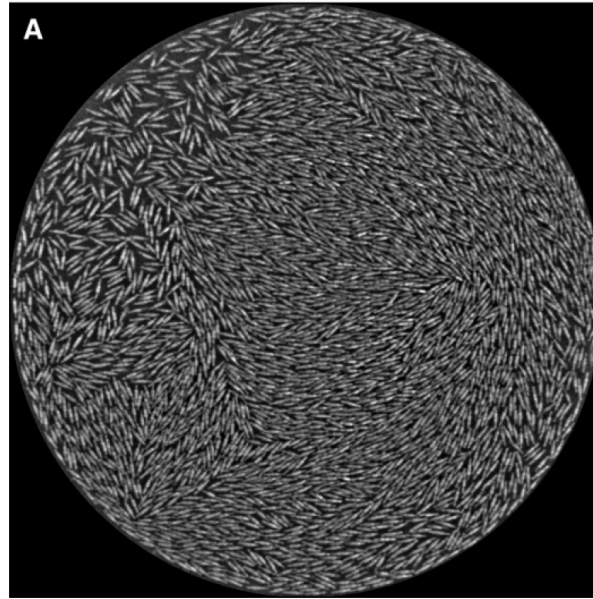
(a)
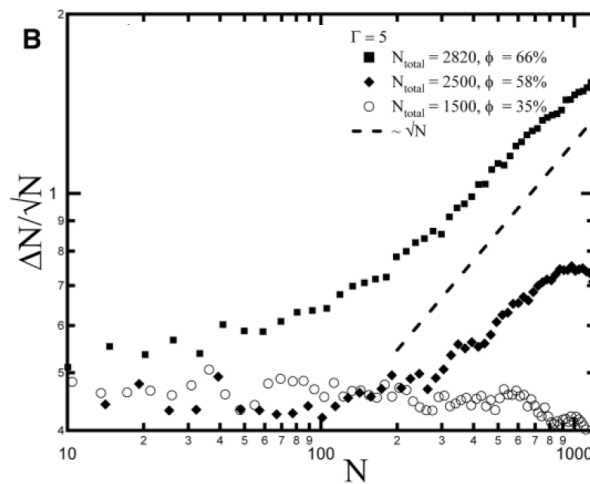
(b)

Figure 1.6: (a) A snapshot of the nematic order of driven rods. (b) The magnitude of the number fluctuations (quantified by ΔN and normalized by $N^{1/2}$) against the mean number of particles, for subsystems of various sizes [44].

1.3.2   Theoretical studies of swarm behavior

In most models of swarm behavior, the mechanism of orientation alignment of agents is artificial and arbitrary. In realistic swarm systems, such as fish school and bird groups, the origin of alignment is often unclear, and is therefore just described phenomenologically. Typically, the agents move with an imposed non-zero speed and tend to align with others in their neighborhood. Although different models have different mechanisms or potential for aligning, the basic properties of swarm behavior is quite universal [56]. The first model, which shows the emergence of a dynamic phase transition from a disordered state (in which agents move in random directions) to an ordered state (where they head in approximately the same direction) as the noise level is decreased or the mean density is increased, is due to Vicsek [58].

The original Vicsek model is defined by

$$\mathbf{r}_i(t + \Delta t) = \mathbf{r}_i(t) + \mathbf{v}_i(t)\Delta t$$

$$\theta_i(t + \Delta t) = \langle \theta(t) \rangle_r + \Delta\theta$$

where $\langle \theta(t) \rangle_r$ denotes the average direction of the velocities of particles (including particle i) within a circle of radius r around $\mathbf{r}_i$. The noise term $\Delta\theta$ is a random number chosen with a uniform probability from the interval $[-\theta'/2, \theta'/2]$. Thus $\theta'=2\pi$ corresponds to the "infinite temperature" limit of the system.

A number of agents are put into the two-dimensional space randomly at the beginning. A transition from the disordered to the ordered state is found by attuning the agent density and noise amplitude, as shown in Fig. 1.7. In a disordered state, the system has a random distribution of agent positions, and has no preferred velocity direction. In the ordered phase, all the agents tend to move in a coordinated direction and aggregate although there is no attractive potential. The transition was originally thought to be of second order [58]. But this result has been disputed in Ref. [53], in which a first order transition is found for large enough system. However, the nature of the phase transition can depend strongly on the way in which the noise is introduced into the system [70]. On the other hand, the difference between a continuous and a discontinuous phase transition can only be observed for very large systems, where it is difficult to carry out extensive numerical computations.

For a system at thermal equilibrium, density is a property that can be measured easily with high accuracy. Consider a system of Brownian particles passively moving with thermal fluctuations. The probability to find k particles in a fixed volume obeys a Poisson distribution,

$$f(k;\lambda) = \lambda^k e^{-\lambda} / k!$$

where $k!$ is the factorial of integer k and λ is the mean particle number in the

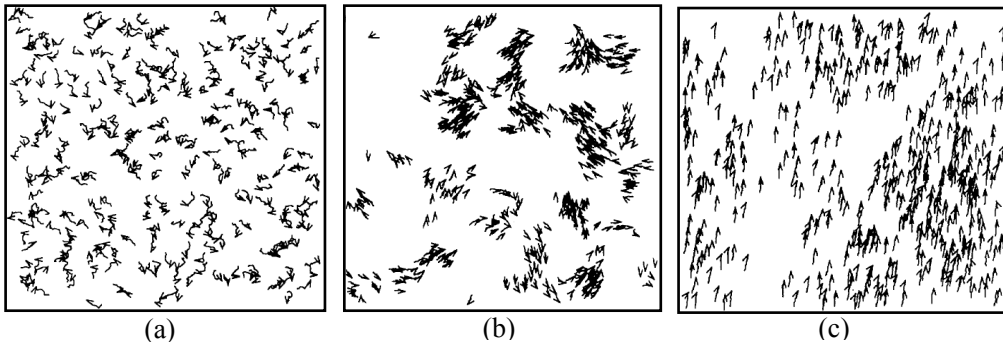| (a) | (b) | (c) |

Figure 1.7: The transition from the disordered to the ordered state by attuning the agent density and noise amplitude in Vicsek model [58]. (a) Disordered state with large noises and small densities; (b) For small densities and noise the particles tend to form groups moving coherently in random directions; (c) For high density and small noise, the motion of particles becomes ordered.
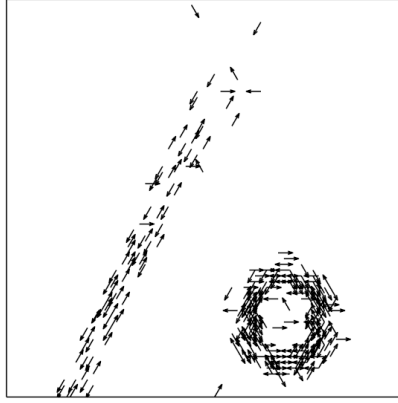
Figure 1.8: A typical stream adjacent to an annular aggregate in myxobacteria simulation [68] .

observation volume, which is the product of particle number density ρ and the volume V. Thus, the standard deviation of the particle number in the observation box is $\lambda^{1/2}$. The accuracy of the density measurement is proportional to $\lambda^{1/2}/V \sim V^{-1/2}$. So, the larger the observed volume is, the more accurately the density can be measured.

In a swarming system, the aligning of velocity directions introduces aggregation. The density fluctuations ΔN are much stronger than in a thermal equilibrium state, a signature of "nonequilibium" systems that form high-density regions. It is the statistical consequence of the complex, coupled, spatiotemporal dynamics of density and orientation in the system [71]. The giant number fluctuations have been analyzed experimentally [43][44] and in simulations [71]. ΔN is found to be proportional to $\lambda^{\beta_{dens}}$, with $\beta_{dens}=1/2$ for a disordered state and $\beta_{dens}>1/2$ for the ordered state. Sometimes β_{dens} approaches to 1, corresponding to a high degree of aggregation.

1.3.3 Theoretical study of self-propelled rods

In some cases on a microscopic scale, the aligning mechanism is well defined. For example, self-propelled spheres embedded in viscous fluids at low Reynolds number swarm though hydrodynamic interaction [57].

Another example is the swarming of rod-like self-propelled particles (rSPP) in 2D. The rods are propelled along the elongated direction in an overdamped environment. When two rods meet, they interact with each other simply by volume exclusion and exchange momentum by collision. Due to the viscous environment, the momentum is not conserved and the energy is dissipated. The result of the collision can be alignment in the same direction, or anti-parallel directions. Thus, the two-dimensional self-propelled-rods system has a natural aligning mechanism due to volume exclusion. The rods aggregate and form clusters as most swarm models do. However, the different aligning mechanisms lead to specific behaviors. In contrast to the power-law distribution of the cluster size of point self-propelled particles with artificial aligning interaction [55], for rods two clustering regions were distinguished by looking at the

transition from unimodal shape to bimodal shape of weighted cluster size distribution functions [25]. In Ref. [24], it was emphasized that the system is incapable of generating a macroscopic polarized state at low density because of the indistinguishable ends of a rod. The only possible bulk states are isotropic and nematic.

The simulations of self-propelled rods successfully reproduce some experimental phenomena. In Ref. [64], the cooperative behavior of cytoskeleton filaments propelled by motor proteins binding to the substrates was studied by simulations. The actively driven systems undergo an analogous phase transition and the motor activity enhances the tendency for nematic order. For myxobacteria, a lattice cell model based on short-range interaction was used in Ref. [68] and reproduced the aggregation mediated by transient streams. The alignment force is the attraction between the front and rear ends of rod cells, which mimics the cell-cell contact at the cell poles of the myxobacteria. The extended structures lead to annular aggregates and streams between two aggregates, as shown in Fig. 1.8.

1.4 Methods

We focus on hydrodynamic interaction and volume exclusion of sperm and rod-like self-propelled particles, and analyze the importance of those interactions for the cooperative behavior.

We first analyze the swarm behavior of rSPP systems, undulating flagella systems and sperm systems in two dimensions. Although the volume exclusion effect is much stronger in two dimensions, and the hydrodynamics is different from that in three dimensions, the results in two dimensions still help to understand the complex non-equilibrium phenomena in these systems. On the other hand, the bacteria, nematodes and sperm have a tendency to aggregate near the experimental substrates due to the self-propelled motion and rod-like configuration. For sperm, hydrodynamic interaction between tails and substrate even strengthen the aggregation [20]. Thus, those active cells and organisms usually swim in a quasi-two-dimensional environment. By comparing results for different systems, we differentiate the fundamental properties of rSPP from other influences such as the sinusoidal undulation and the viscous resistance of large heads. Some of the experimental phenomena such as sperm "trains" and vortices are successfully reproduced in our simulations.

In three dimensions, the system has more degrees of freedom, thus the cooperation is much more complex. The behavior of flagella and sperm systems in bulk and in confined space is simulated.

We use a particle-based mesoscale simulation technique, called multi-particle

collision dynamics (MPC), to model the hydrodynamics [72][73]. MPC is well suited for systems with a wide range of Reynolds number [74][75]. Elgeti et al [20][76] applied MPC to the study of three-dimensional sperm behavior near substrates. We also perform simulations of sperm and flagella models with anisotropic friction, which is a first order approximation of hydrodynamics. The flagella and sperm take advantage of the different friction coefficients to move forwards, whereas the interaction between two swimmers is only the physical volume exclusion. Thus, by comparing the results in MPC fluid and with anisotropic friction, we can separate the effects of purely volume exclusion from hydrodynamic interaction between sperm.

II. Simulation methods and models

2.1 Navier-Stokes equation

The Navier-Stokes equation for incompressible flow of Newtonian fluids is [77]

$$\rho\left(\frac{\partial}{\partial t} + \mathbf{v}\cdot\nabla\right)\mathbf{v} = \eta\nabla^2\mathbf{v} - \nabla p + \mathbf{f}_{ext} \qquad [2.1]$$

where $\mathbf{v}$ is the flow velocity, ρ is the density, η is the dynamic viscosity, p is the pressure, ∇ is the gradient operator, and $\mathbf{f}_{ext}$ represents body forces (per unit volume) acting on the fluid. The term on the left side of equation is inertia force per volume. $\partial\mathbf{v}/\partial t$ is the unsteady acceleration and $(\mathbf{v}\cdot\nabla)\mathbf{v}$ represents the convective acceleration. The first term on right side is the viscous force, and the second term is the pressure gradient.

The dimensionless form of Navier-Stokes equation can be obtained by rescaling all quantities in the equation. If we rescale them by

$$\mathbf{v'}=\frac{\mathbf{v}}{\upsilon}, \quad p'=\frac{p}{\rho\upsilon^2}, \quad \mathbf{f'}_{ext}=\mathbf{f}_{ext}\frac{l}{\rho\upsilon^2}, \quad \frac{\partial}{\partial t'}=\frac{l}{\upsilon}\frac{\partial}{\partial t}, \quad \nabla'=l\nabla ,$$

the dimensionless form of the equation is,

$$\left(\frac{\partial}{\partial t'} + \mathbf{v'}\cdot\nabla'\right)\mathbf{v'}=\frac{\eta}{\rho l\upsilon}\nabla'^2\,\mathbf{v'}-\nabla' p'+\mathbf{f'}_{ext}$$

Here, υ is the velocity of the stream, and l is a typical length of the system, e.g. the diameter of pipe for fluids flow though it. A dimensionless number, Reynolds number, is defined as $Re=\rho\upsilon l/\eta$. Thus,

$$\left(\frac{\partial}{\partial t'} + \mathbf{v'}\cdot\nabla'\right)\mathbf{v'}=\frac{1}{Re}\nabla'^2\,\mathbf{v'}-\nabla p'+\mathbf{f'}_{ext} .$$

According to the law of similarity, flows of the same type with the same Reynolds number are similar. When Re is very large, the viscosity term ($Re^{-1}\nabla'^2\mathbf{v}$) is negligible. The equation becomes Euler's equation for ideal fluid in which thermal conductivity and viscosity are unimportant. For example, Re is about 4×10^6 for a person swimming in water.

Another dimensionless form of Eq. 2.1 is

$$Re\left(\frac{\partial}{\partial t'} + \mathbf{v'}\cdot\nabla'\right)\mathbf{v'}=\nabla'^2\,\mathbf{v'}-\nabla p'+\mathbf{f'}_{ext} . \qquad [2.2]$$

where

$$\mathbf{v}'= \frac{\mathbf{v}}{\upsilon}, \quad p'= \frac{pl}{\eta\upsilon}, \quad \mathbf{f}'_{ext}= \mathbf{f}_{ext}\frac{l^2}{\eta\upsilon}, \quad \frac{\partial}{\partial t'} = \frac{l}{\upsilon}\frac{\partial}{\partial t}, \quad \nabla'= l\nabla.$$

When Re<<1, the terms on the left side of the equation vanishes. The equation becomes Stokes's equation for creeping flow in which viscosity is dominating and the flow velocity is small. For sperm swimming in the fluid medium, Re is approximately 10^{-2}.

2.2 Multi-particle collision dynamics (MPC)

MPC was first introduced by Malevanets and Kapral [78][79] in 1999. It employs a discrete-time dynamics with continuous velocities and local multi-particle collisions. Mass, momentum, and energy are locally conserved quantities by construction and it has been demonstrated that hydrodynamic equations are satisfied. This method is adequate to describe the complex fluid behavior for a wide range of Reynolds numbers (see review in Ref. [72][73]).

The MPC fluid is modeled by N point particles, which are characterized by their mass m_i, continuous space position $\mathbf{r}_i$ and continuous velocity $\mathbf{u}_i$, where $i = 1…N$. In MPC simulations, time t is discrete. During every time step $\Delta\tau$, there are two simulation steps, streaming and collision. In the streaming step, the particles do not interact with each other, and move ballistically according to their velocities

$$\mathbf{r}_i(t + \Delta\tau) = \mathbf{r}_i(t) + \mathbf{u}_i\Delta\tau$$

In the collision step, the particles are sorted into collision boxes of side length a according to their position, and interact with all other particles in same box through a multi-body collision. The collision step is defined by a rotation of all particle velocities in a box in a co-moving frame with its center of mass. Thus, the velocity of the i-th particle in the j-th box after collision is

$$\mathbf{u}_i(t + \Delta\tau) = \mathbf{u}_i(t) + \mathcal{R}_j(\alpha)[\mathbf{u}_i - \mathbf{u}_{cm,j}]$$

where

$$\mathbf{u}_{cm,j}(t) = \frac{\sum_j m_i \mathbf{u}_i}{\sum_j m_i}$$

is the center-of-mass velocity of j-th box. $\mathcal{R}_j(\alpha)$ is a stochastic rotation matrix to rotate a vector around a random direction generated independently for each collision box j. In two dimensions (2D), $\mathcal{R}_j(\alpha)$ rotates a vector by an angle $\pm\alpha$, with the sign chosen randomly. In three dimensions (3D), $\mathcal{R}_j(\alpha)$ rotates a 3D vector by the given angle around a random direction in 3D. There are two schemes for the random collisions in 3D. The first scheme [80] chooses the rotation direction among the three main axis
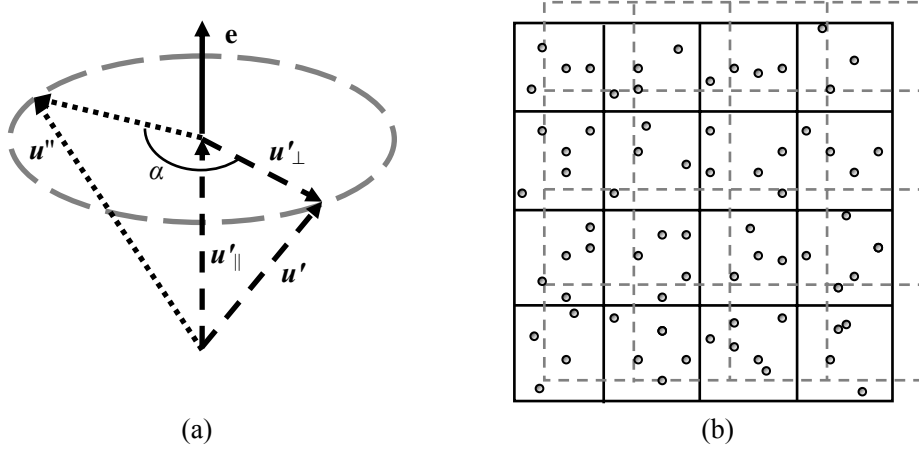
Figure 2.1: (a) Rotation of a vector **u** around a direction given by a unit vector **e**. (b) Diagram of the random shift of the collision grid.

and the rotation is performed by an angle α; in the second one [81], the random direction is generated in each collision box by selecting two uncorrelated random numbers r_1, r_2 from a distribution in the interval $[0, 1]$. The random unit vector **e** has components,

$$\mathbf{e}_x = \sqrt{1-\varphi_1^2}\cos\varphi_2, \quad \mathbf{e}_y = \sqrt{1-\varphi_1^2}\sin\varphi_2, \quad \mathbf{e}_z = \varphi_1$$

where $\varphi_1 = 2r_1 - 1$ and $\varphi_1 = 2\pi r_2$. The new vector $\mathbf{u}_i''$ is the result of rotating $\mathbf{u}_i' = \mathbf{u}_i - \mathbf{u}_{\mathrm{cm},j}$ around **e** by an angle α,

$$\mathbf{u}'' = \mathbf{u}'_{\parallel} + \mathbf{u}'_{\perp}\cos\alpha + \left(\mathbf{u}'_{\perp}\times\mathbf{e}\right)\sin\alpha$$

where $\mathbf{u}'_{\parallel} = (\mathbf{e}\cdot\mathbf{u}')\,\mathbf{e}$ and $\mathbf{u}'_{\perp} = \mathbf{u}' - \mathbf{u}'_{\parallel}$, as shown in Fig. 2.1a. We use the second scheme in our 3D simulation, because it introduces less anisotropy in the system due to the underling lattice.

During the collision each particle changes the magnitude and direction of its velocity, but the total momentum and kinetic energy are conserved within every collision box. In order to ensure Galilean invariance, a random shift of the collision grid has to be performed [82][83]. The collision grid is displaced by a random number uniformly distributed in the interval $(0,a)$ which is chosen independently in each collision. In Fig. 2.1b, the solid grid represents the fixed grid, while the discontinuous grid would be one of the possible displaced grids.

The total kinematic viscosity $v = \eta/\rho$ is the sum of two contributions, the kinetic viscosity v_{kin} and the collision viscosity v_{coll}. The approximate analytical expressions are [80][84]

$$\frac{v_{coll}}{\sqrt{k_B T a^2 / m}} = \frac{1}{12h}\left(1-\cos\alpha\right)\left(1-\frac{1}{\rho}\right)$$

$$\frac{v_{kin}}{\sqrt{k_B T a^2 / m}} = h\left(\frac{1}{1-\cos\alpha}\frac{\rho}{\rho-1}-\frac{1}{2}\right)$$
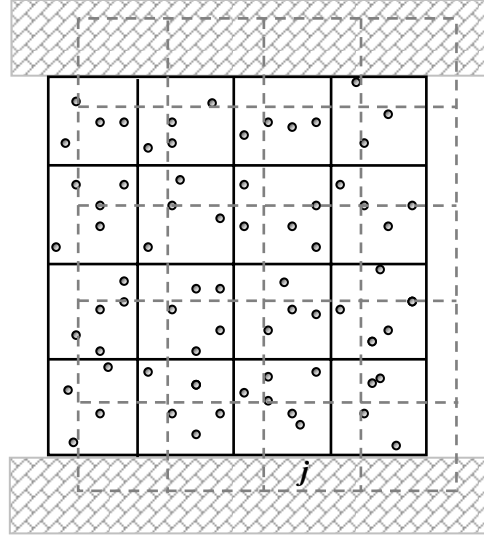
Figure 2.2: Random-shift in the presence of walls.

in 2D, and

$$\frac{v_{coll}}{\sqrt{k_B T a^2 / m}} = \frac{1}{18h} (1 - \cos \alpha) \left(1 - \frac{1}{\rho}\right)$$

$$\frac{v_{kin}}{\sqrt{k_B T a^2 / m}} = h \left(\frac{1}{4 - 2\cos\alpha - 2\cos 2\alpha} \frac{5\rho}{\rho - 1} - \frac{1}{2}\right)$$

in 3D. Here ρ is the average number of solvent particle in each collision box, m is the mass of solvent particle and $h = \Delta\tau\sqrt{k_B T / m a^2}$ is the rescaled mean free path. We use $k_B T$=1, m=1, a=1, ρ=10. This implies, in particular, that the simulation time unit $(ma^2/k_B T)^{1/2}$ equals unity. In 2D simulations, we choose α=90° and $\Delta\tau$=0.025. Thus the total kinematic viscosity of fluid is v=v_{coll} + v_{kin}≈3.02. In 3D simulations, we choose α=130° and $\Delta\tau$=0.05. Thus the total kinematic viscosity of fluid is v=v_{coll} + v_{kin}≈1.60.

In some 3D simulations, we implement fixed walls with no-slip boundary conditions. For MPC solvent particles, standard bounce-back is applied during the streaming step. This means, when a particle hits the walls, it returns in the incoming direction with inverted velocity. Due to the random shift of the collision grid, the walls generally do not coincide with the cell boundaries, as shown in Fig. 2.2. The cells in the boundary are generally partially filled. During the collision step, for all the cells of the channel which are cut by walls, extra virtual particles are added. The number of virtual particles n' in box j at the wall equals the number of solvent particles inside the corresponding cell j' at the opposite wall. Thus the total number of solvent particles and virtual particles in box j still obeys a Poisson distribution. The velocities of the virtual particles are drawn from a Maxwell-Boltzmann distribution of zero average velocity and the same temperature $k_B T$ as the fluid. The collision step is then carried out with the average velocity of all particles in the cell,

$$\mathbf{u}_{\text{cm},j}(t) = \frac{\sum_j m_i \mathbf{u}_i + \mathbf{a}}{\sum_j m_i + n'_j m}$$

where $\mathbf{a}$ is a vector whose components are numbers from a Maxwell-Boltzmann distribution with zero average and variance $n'_j k_B T$. Note that the temperature of virtual particles represents the temperature of the walls. The total energy and momentum of the fluid is not conserved with the presence of walls. The system is in contact with a thermal bath of temperature T.

We use the MPC method to model the hydrodynamics of swimmers. Since energy is injected into the system by the active beating motion, we employ a thermostat to keep the fluid temperature constant by rescaling all fluid-particle velocities in a collision box relative to its center-of-mass velocity after each collision step,

$$\mathbf{u}_{i,thermo} = \mathbf{u}_{\text{cm},j}(t) + \sqrt{\frac{k_B T}{k_B T'}}\left[\mathbf{u}_i - \mathbf{u}_{cm,j}\right]$$

where $\mathbf{u}_{i,thermo}$ is the velocity of the i-th particle after the thermostat, $k_B T'$ is the local temperature of j-th box. Through the thermostat, we extract energy from the system,

$$\Delta E = \sum_i \frac{1}{2} m_i \left(\mathbf{u}_{i,thermo} - \mathbf{u}_i\right)^2$$

which is the energy dissipated by swimmers, in other words the energy consumption of swimmers to propel themselves in the viscous medium. Note that we do not apply the thermostat to swimmer particles.

2.3 Self-propelled rods in two dimensions

N rods of equal length l are put into a 2D simulation box of size $L_x \times L_y$ with random initial positions and random initial orientations without any overlap. The number density of the rod is $\rho_r = N/(L_x \times L_y)$. Each rod is characterized by a direction angle θ_i, center-of-mass position $\mathbf{r}_i$, center-of-mass velocity $\mathbf{v}_i$ and a rotation velocity along the center of mass ω_i. The rods move ballistically according to their velocities,

$$\mathbf{r}_i(t + \Delta\tau') = \mathbf{r}_i(t) + \mathbf{v}_i \Delta\tau'$$

$$\theta_i(t + \Delta\tau') = \theta_i(t) + \omega_i \Delta\tau'$$

The time step is $\Delta\tau' = 10^{-3}$ in rod simulations. The center-of-mass velocity $\mathbf{v}_i$ can be separated into two parts,

$$\mathbf{v}_i = \mathbf{v}_{i,\parallel} + \mathbf{v}_{i,\perp}$$

where $\mathbf{v}_{i,\parallel}$ is the velocity component parallel to the extended axis of a rod, and $\mathbf{v}_{i,\perp}$ is
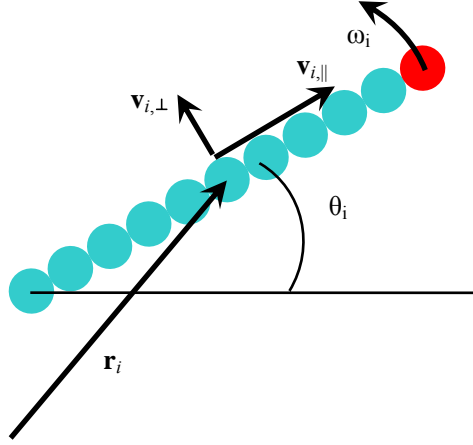
Figure 2.3: Two-dimensional model of a self-propelled rod. The rod is discretized into L_r beads when calculating volume exclusion force.

perpendicular to the extended axis.

A simple first-order approximation of hydrodynamics of rods at low Reynolds number is an anisotropic friction. The viscous resistance force of a rod is

$$\mathbf{F}_\parallel = \gamma_\parallel \mathbf{v}_\parallel , \qquad \mathbf{F}_\perp = \gamma_\perp \mathbf{v}_\perp \qquad\qquad [2.3]$$

where $\gamma_\parallel$ and $\gamma_\perp$ are the parallel and perpendicular friction coefficients, respectively. $\gamma_\parallel$ and $\gamma_\perp$ depend on the rod length as well as the aspect ratio of rod length and diameter. In the limit of long and thin rod, the ratio is $\gamma_\parallel / \gamma_\perp = 1/2$.

The rod performs an overdamped translational motion with anisotropic friction coefficient. The equations of motion are

$$\mathbf{v}_{i,\parallel} = \frac{1}{\gamma_\parallel} \left(\sum_{j \neq i}^{N} \mathbf{F}_{ij,\parallel}^{ex} + \xi_\parallel \mathbf{e}_\parallel \right) + v_{i,0} \mathbf{e}_\parallel$$

$$\mathbf{v}_{i,\perp} = \frac{1}{\gamma_\perp} \left(\sum_{j \neq i}^{N} \mathbf{F}_{ij,\perp}^{ex} + \xi_\perp \mathbf{e}_\perp \right)$$

$$\omega_i = \sum_{j \neq i}^{N} M_{ij} / \gamma_r + \xi_r$$

where $\mathbf{e}_\parallel$ is the unit vector of orientation direction of rod, $\mathbf{e}_\perp$ is the unit vector perpendicular to the rod, $v_{i,0}$ is the forward speed of rod i when it is freely swimming. $\mathbf{F}_{ij}^{ex}$ is the volume exclusion (VE) force on rod i from rod j and M_{ij} is the torque generated by the volume exclusion force on rod i. The friction coefficients are $\gamma_\parallel = l$, $\gamma_\perp = 2\gamma_\parallel$ and the rotational friction coefficient $\gamma_r = \gamma_\parallel l^2 / 6$. $\xi_\parallel$, $\xi_\perp$ and ξ_r are white noise with variances $\sigma^2 l$, $\sigma^2 l$ and $\sigma^2 l^3 / 12$ respectively. Note that the noise here is not due to thermal fluctuation in a fluid with different intensities in different directions. Thermal fluctuations usually are not important for the self-propelled cells and organisms, thus we do not consider them here.

We discretize the rod into L_r particles as illustrated in Fig. 2.3. The distance between neighbor particles is the unit length. To describe the volume exclusion we use the shifted, truncated Leonard-Jones potential between particles in different rods

$$V(r) = \begin{cases} 4\varepsilon\left[\left(\dfrac{1}{r}\right)^{12} - \left(\dfrac{1}{r}\right)^{6}\right] + \varepsilon, & r < 2^{1/6} \\ 0, & r \geq 2^{1/6} \end{cases} \qquad [2.4]$$

where r is the distance between particles. We use the interaction strength $\varepsilon = 1$ for all rod simulations.

We study the rods of length L_r=11, which corresponds to an aspect ratio of approximately 10. The aspect ratio of our rods compares reasonably well with myxobacteria, which aggregation, are elongated with their width of 0.7 to 1.2μm and length of 2 to 12μm [68] . The diversity of rod lengths and propulsion forces, which serve as source of the internal fluctuation of rods, are not taken into consideration here. If not explicitly mentioned, the simulation box size is $L_x \times L_y = 400 \times 400$.

2.4 Flagella and sperm models in two dimensions

We construct the coarse-grained flagellum model by a sequence of connected particles as shown in Fig. 2.4. N_f particles are aligned and linked with neighbors by springs of finite rest length $l_0 = 0.5a$, where a is the length unit of the MPC fluid. Each particle has a mass m'=10m. A bending elasticity is necessary for the flagella to maintain a smooth shape in a fluctuating environment, and to implement the beating pattern. Two flagella can not intersect or overlap. Thus the total potential of the model is

$$E_{total} = E_{bond} + E_{bend} + V_{VE}$$

$$E_{bond} = \sum_{i}^{N_f-1} \frac{1}{2} k \left(|\mathbf{R}_i| - l_0 \right)^2$$

$$E_{bend} = \sum_{i} \frac{1}{2} \kappa \left\{ \mathbf{R}_{i+1} - \mathcal{R}(l_0 c)\mathbf{R}_i \right\}^2$$

V_{VE} is the shifted, truncated Leonard-Jones potential (Eq. 2.4) between particles on different flagella, with $\varepsilon = 15 k_B T$. $\mathbf{R}_i$ is the vector from the i-th particle to the (i+1)-th particle, $\mathcal{R}(l_0 c)$ is a rotation matrix, which rotates a vector anti-clockwise by an angle $l_0 c$, and c is the local spontaneous curvature. The spring constant is chosen to be $k=2\times10^5 k_B T/a^2$, and the bending rigidity $\kappa = 10^4 k_B T/a^2$. They are much larger than the thermal energy $k_B T$ to guarantee that the mechanical forces dominate the thermal forces. The local spontaneous curvature c changes with time t and the position x along the flagellum to create a propagating bending wave,
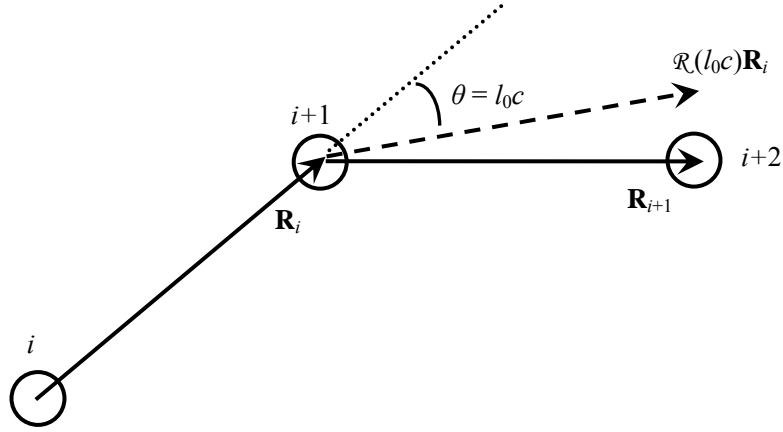
Figure 2.4: The illustration of the basic segment of 2D flagellum model.

$$c_s(x,t) = c_0 + A\sin\left[-2\pi f_s t + qx + \varphi_s\right] \hspace{3cm} [2.5]$$

The detailed analysis of the beating pattern of nematodes [12] and bull sperm [86][87] shows that a single sine mode represents the beat to a very good approximation. The wave number q determines the number of complete waves on the flagellum. For $q=2\pi/l_0 N_f$, one complete wave is present. f_s is the beating frequency of the s-th flagellum. In nature, sperm of the same species always have a wide distribution of beat frequencies. For example, the beat frequency of sea-urchin sperm ranges from 30Hz to 80Hz [29][29], and the frequency of bull sperm ranges from 20Hz to 30Hz [87]. Thus the frequency is chosen from a Gaussian distribution with average frequency f_0 and variance $\sigma_f f_0$ and

$$\sigma_f = \frac{\sqrt{<(f_s - f_0)^2>}}{f_0}$$

Two flagella with different frequencies have a small difference in their forward velocities. The constant c_0 determines the average spontaneous curvature of the flagellum. φ_s is the initial phase of the first particle on the s-th flagellum, and A is a constant related to the beating amplitude. We choose $A=0.2$, which induces a beating amplitude $A_{tail}=3.2a$ when $N_f = 50$ and $q=2\pi/l_0 N_f$. As t increases, a wave propagates along the flagellum from the first to the last particle, pushing the fluid backwards, and at the same time propelling the flagellum forward. We keep A, q, f_s, and φ_s constant for each flagellum during a simulation. Although the spontaneous local curvature is prescribed, the tail is elastic and its configuration is affected by the viscous medium and the flow field generated by the motion of other flagella. For flagellum simulations, we use N_f=50, $q=2\pi/l_0 N_f$ and f_0=1/120 unless mentioned explicitly.

As explained in Section 1.2.1, a sperm usually consists of three parts: a head containing the genetic information, a beating long tail, and a mid-piece to connect head and tail. We constructed a coarse-grained 2D sperm model by adding a head and a mid-part in front of the flagellum model as shown in Fig. 2.5. The head is
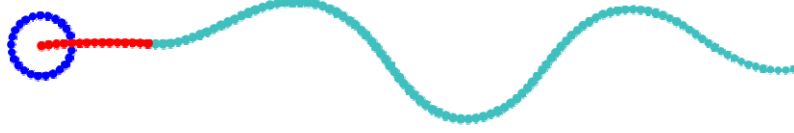
Figure 2.5: Two-dimensional model of sperm. The model consists of three parts, the head (blue), the mid-piece (red) and the tail (cyan). Two sinusoidal waves are present on the beating tail.

constructed of N_{head}=25 particles, where neighboring particles are linked by springs of finite length l_0=0.5a with interaction potential

$$E_{bond,head} = \sum \frac{1}{2} k_{head-mid} (l - l_0)^2$$

into a circle of radius 2a. Each of the head particles has a mass m_{head}=20m. The mid-piece consists of N_{mid}=14 particles of mass m_{mid}=10m connected by springs of length l_0=0.5a. The first particle of the mid-piece, which is fixed to the center of the head, is connected with every particle on the head by a spring of length $l_{head-mid}$=2a, in order to maintain the circular shape of the head, as well as to stabilize the connection between head and mid part. The tail has N_{tail}=100 particles of mass m_{tail}=10m, linked together by springs of length l_0=0.5a. The spring constants are chosen to be $k_{head-mid}$=10$^4 k_B T/a^2$, k_{head}=10$^5 k_B T/a^2$, k_{mid}=k_{tail}=2×10$^5 k_B T/a^2$, where $k_{head-mid}$ is the spring constant for the connection of the head particles and the center, and k_{tail} and k_{mid} are the spring constants for the tail and the mid-piece, respectively. The wave number q=4$\pi/l_0 N_{tail}$ is chosen to mimic the tail shape of sea-urchin sperm [29][29], so that the phase difference between the first and the last particles of the tail is 4π, and two waves are present.

In order to avoid intersections or overlaps of different sperm, the shifted, truncated Leonard-Jones potential Eq. 2.4, is employed, and all other parameters are the same as for 2D flagella.

For the simulations with full hydrodynamics, during the MPC streaming step, the equations of motion of the flagella and sperm particles are integrated by a velocity-Verlet algorithm, with a molecular-dynamics time step $\Delta\tau'$=5×10^{-4}, which is 1/50 of the MPC time step $\Delta\tau$. The coarse-grained model only interacts with the fluid during the MPC collision step. This is done by sorting the particles together with the MPC solvent particles into the collision cells and rotating their velocities relative to the center-of-mass velocity of each cell [73].

In order to distinguish the effects of volume exclusion (VE) and hydrodynamic interaction (HI), we also perform the simulations of the flagellum model with anisotropic frictions (AF) by Eq. 2.3. The friction coefficients are different in tangent and normal directions of the flagellum configuration

$$\mathbf{F}_{\|,i} = -\gamma_\| \mathbf{v}_{i,\|} = -\gamma_\| \left(\mathbf{v}_i \cdot \mathbf{e}_{(\mathbf{R}_{i+1} - \mathbf{R}_{i-1})} \right) \mathbf{e}_{(\mathbf{R}_{i+1} - \mathbf{R}_{i-1})}$$

$$\mathbf{F}_{\perp,i} = -\gamma_\perp \mathbf{v}_{i,\perp} = -\gamma_\perp \left[\mathbf{v}_i - \mathbf{v}_{i,\parallel} \right]$$

where $\mathbf{e}_{(\mathbf{R}_{i+1} - \mathbf{R}_{i-1})}$ is the unit vector along rod direction at i-th particle on flagella.

For sperm or nematodes, thermal fluctuations are negligible due to the large mass of the self-propelled particles (SPPs) relative to mass of the solvent molecules. In fluid dynamics, the Péclet number is a dimensionless number relating the rate of advection of flow to its rate of diffusion. For a self-propelled particle of large size, the Péclet number Pe can be written as,

$$Pe = \frac{Lv}{D} \qquad\qquad [2.6]$$

where L is the characteristic length of the particle, v is the forward velocity and D is its thermal diffusion coefficient. In our MPC fluid, the thermal diffusion coefficient of a Brownian particle of mass M is [88],

$$D = \frac{k_B T}{M} h \left(\frac{1}{\chi} - \frac{1}{2} \right),$$

where χ is the decorrelation factor,

$$\chi = \frac{2}{3}(1 - \cos\alpha)\frac{\rho - 1}{\rho}$$

For a flagellum swimming in a MPC fluid, with the parameters $k_B T$=1, M=500, h=0.025, ρ=10, α=90°, L=25a, we get the velocity of the flagella of v=0.020±0.001. Thus the Péclet number is $Pe = 9.5\times10^4$. For overcome a distance of L=25a, the thermal diffusion takes 9.5×10^4 times longer time than the self-propelled motion. Therefore, in our AF simulation, thermal fluctuations are not considered. In addition, note that in AF approximation, there is no hydrodynamic interaction between two flagella, which plays an important role as environmental fluctuation in MPC simulation.

2.5 Flagellum and sperm model in three dimensions

We construct a 3D flagellum model by three strings of particles connected by springs, as illustrated in Fig. 2.6. The mass of each particle is m_s=5m. The same model was applied to the study of single sperm behavior near the substrate [76]. The flagellum consists of N repeated segments of three point particles and 12 springs. The potential of each spring is,

$$E = \frac{1}{2}k(l - l_0)^2$$

where k=2×10$^4 k_B T/a^2$, which makes the thermal fluctuation of spring length is less then 2% of its rest length l_0. l_0 is different for each spring. The values of l_0 for springs of different color in Fig. 2.6 are
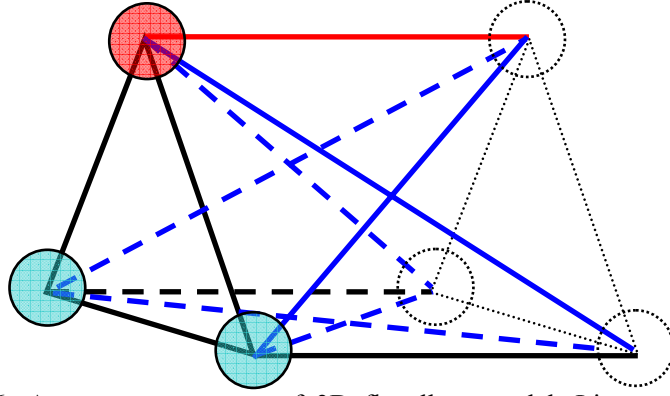
Figure 2.6: A structure segment of 3D flagellum model. Lines of different colors represent springs of different rest length. The dotted lines represent the springs and particles belonging to the next segment.
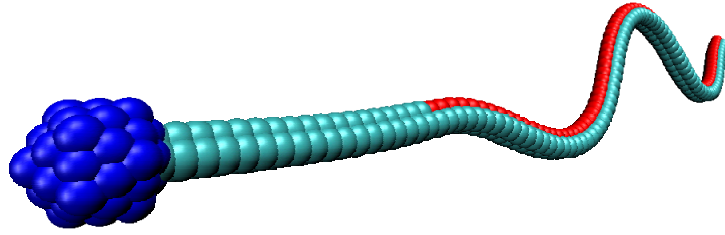

Figure 2.7: The illustration of a 3D sperm model.

$$l_{0,black} = 0.5a$$

$$l_{0,blue} = 0.5\sqrt{2}a$$

$$l_{0,red} = 0.5a + A\sin(qi - 2\pi f_s t + \varphi_{0,s}) + c' \qquad [2.7]$$

where a is the length unit in MPC fluid, i is the number of the segment on the flagellum counted from the front of the flagellum. The red springs are active springs which are changing their rest length with time. Thus a sinusoidal wave propagating along the flagellum is created. As in the 2D model, f_s is the frequency of the s-th flagellum, q is the wave number, $\varphi_{0,s}$ is the initial phase, A is the amplitude of the change of the rest length and determines the amplitude of the sinusoidal configuration of flagellum. An extra constant c' implies a constant curvature of the flagellum.

VE in 3D is applied between the centers of mass of segments on different flagella by the same shifted, truncated Leonard-Jones potential of Eq. 2.4. The force is calculated and divided into three equal components applied to each particle in the segment.

The 3D sperm model is simply the flagellum model plus a mid-part and a head. The mid-part has the same structure as the flagellum model with $l_{0,red}=l_{0,blue}$, because the mid-part is not actively beating. The head is modeled by a sphere, constructed of 43 monomers, which are attached to the front of the mid-part. The head has a radius of $r_h=a$ and is held together by harmonic springs (with spring constants $k_h=10^4 k_B T/a^2$

between center and head monomer, and $k_{h2}=10^5 k_B T/a^2$ between neighbor monomers). The same VE potential of Eq. 2.4 is applied for each head monomer. A snapshot of 3D sperm model is shown in Fig. 2.7.

The motion equation of particles is integrated by a velocity-Verlet algorithm, with the molecular-dynamic time step $\Delta\tau'=5\times10^{-4}$. During the MPC collision step, the particles of each flagellum or sperm are sorted into collision boxes and collide with solvent particles.

2.5 Comparison with real micro-organisms

Our flagellum and sperm models in 2D and in 3D retain the most important features, such as the rod-like structure and the active undulating motion. We neglect many details of these structures, such as the non-uniform thickness and asymmetry of the sperm head. The local spontaneous curvature is simplified as a simple sine wave. We expect that such details will not influence the general self-propelling and cooperation behavior.

However, there are at least one important difference between real micro-organisms and our models, which possibly changes the behavior qualitatively. The spontaneous curvature to generate the beat motion of the flagellum does not change in response to an external force. In our model, the flagellum shape is able to respond to the viscous medium. However, the spontaneous local curvature of a flagellum (Eq. 2.5 and Eq. 2.7) does not have a term to interact with external force. The external force comes from the interaction with solvent particles and the VE with other flagellum or sperm in system. For a real sperm or nematode, there could be some mechanisms to change the frequency and phase of the beat mode, or even the shape, according to local HI and VE contacts with other particles.

III.   Self-propelled rods in two dimensions

In our model, the self-propelled rods (rSPP, rod-like self-propelled particles) of the same length collide and interact through volume exclusion. Due to the overdamped motion and the propelling forces, the result of the collision is neither energy- nor momentum-conserving. The only aligning mechanism is the hard core interaction which does not distinguish the two rod orientations. Thus the volume exclusion (VE) aligns the rods parallel or anti-parallel. After collision, due to the gliding motion along the long axis, two parallel rods move together for a time period until the environmental noise separates them; two anti-parallel rods leave each other very quickly. When the rods form clusters, the environmental noise shakes the clusters and tends to break up them. There is a competition between cluster formation and cluster break-up. The degree of aggregation depends on the system parameters such as the rod length L_r, the gliding speed v_0, the variance of environmental noise σ^2, and the rod number density ρ_r.

3.1 Probability density function (PDF) of cluster size

The simulations start with random states. The rods are put into the simulation box with random orientation and random position without any overlapping. When they start gliding, they aggregate and form clusters. Large clusters are formed by the collisions of smaller ones, at the same time they break up into smaller ones due to the external forces from collisions or the environmental noise. After some time, the system reaches a stationary state that the formation rate of any cluster of size n is balanced by its break-up rate. In the stationary state, the probability density function (PDF) of finding a cluster of size n does not change with time, and all those quantities related to PDF, such as the average cluster size $<n>$ and the average cluster weight $<w>$, are stationary. However, due to the finite simulation box size, these quantities fluctuate around their stationary value.

We define a cluster as follows. We consider two rods to be in the same cluster, if the angle between them is less than $\pi/6$ and the nearest distance is less than $2a$, which is about two times the rod diameter. A cluster is defined here as a set of rods that are connected or neighbor either directly or through other rods at a given moment in time. Its size is the number of rods it contains. A freely gliding rod without any neighbors is considered as a "cluster" of size 1. Three types of PDF, corresponding to three different states of the system, are found.

3.1.1 Three types of PDF

With low rod density ρ_r or strong environmental noise σ^2, we find the first type of PDF (denoted PDF1), as shown in Fig. 3.1. PDF1 decreases as a power law for small cluster size, then deviates from the power-law decay and drops quickly for large n. In a system characterized by PDF1, very large clusters are hardly found. The system is filled with small clusters which glides in all directions and make frequent collisions.

The power-law decay results from the competition of cluster formation and break up. The formation rate depends on the collision rate of clusters, while the break-up rate depends on not only the collision rate, but also the environmental noise and the
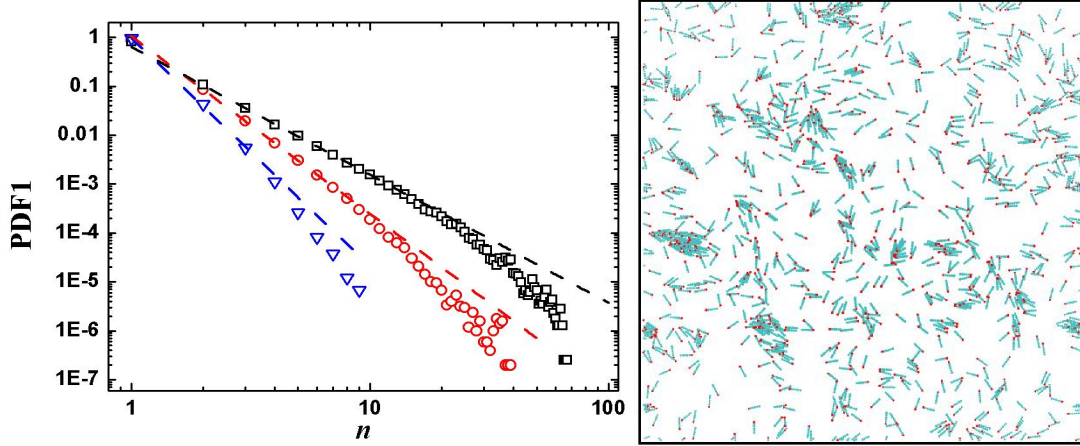

Figure 3.1: The first type of PDF. The parameters are: $\rho_r L_r^2$=0.7744, σ^2=2^6 for black squares ($\square$); $\rho_r L_r^2$=0.7744, σ^2=$2^{7.2}$ for red circles ($\bigcirc$); $\rho_r L_r^2$=0.1936, σ^2=2^6 for blue triangles ($\triangledown$). The dashed lines are fit lines of the power-law-decay part of PDF1. The snapshot on the right is from the system for black squares ($\square$). Red dots in the snapshot denote the front of rods. Note that periodic boundary conditions are employed.

Figure 3.2: The second type of PDF. The parameters are: $\rho_r L_r^2$=0.7744, σ^2=$2^{3.6}$ for black squares ($\square$); $\rho_r L_r^2$=0.7744, σ^2=$2^{4.9}$ for red squares ($\bigcirc$); $\rho_r L_r^2$=2.1901, σ^2=2^6 for blue triangles ($\triangle$). The dashed line is the fit line of the power-law-decay part of black squares ($\square$). The snapshot is from the system for black squares ($\square$). Red dots in the snapshot denote the front of rods. Note that periodic boundary conditions are employed.
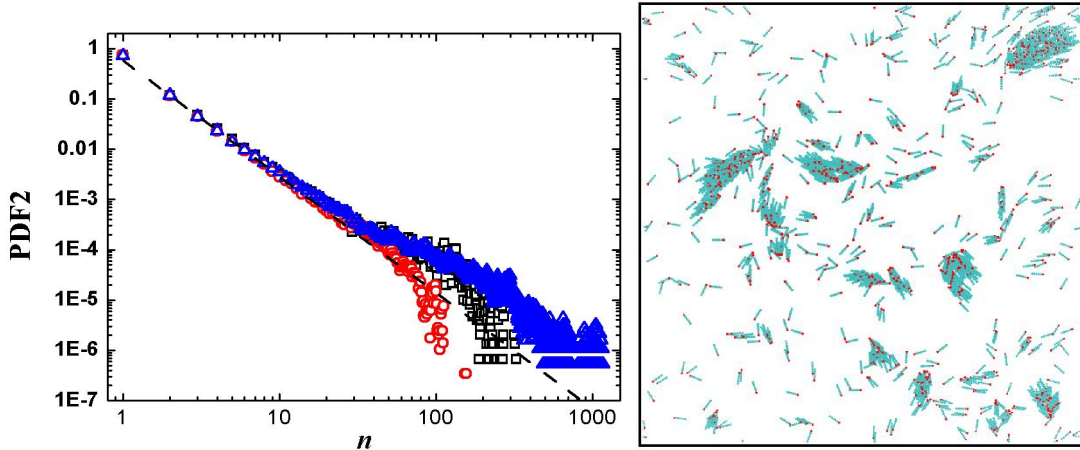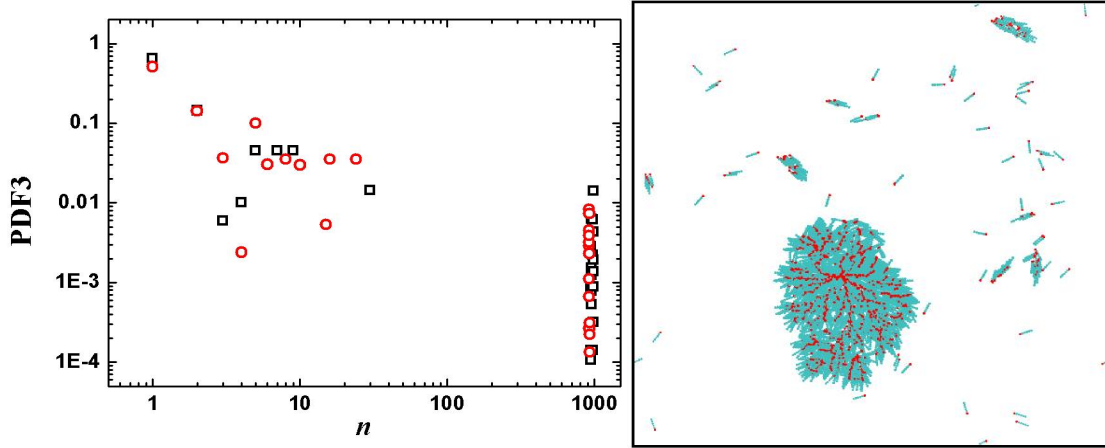
Figure 3.3: The third type of PDF. The parameters are: $\rho_r L_r^2$=0.7744, σ^2=2^0 for black squares ($\square$); $\rho_r L_r^2$=0.7744, σ^2=$2^{0.6}$ for red circles ($\bigcirc$). The snapshot is from the system for red circles ($\bigcirc$). Red dots in the snapshot denote the front of rods.

cluster size. A larger cluster, which contains more rods, has more chance to reduce its size due to the noise and larger scattering cross section. How far the power-law-decay region of PDF1 can extend depends on the rod density ρ_r and environmental noise σ^2.

The second type of PDF (denoted PDF2), shown in Fig. 3.2, is the transition form of PDF1 and PDF3. It is found for intermediate values of ρ_r and σ^2. PDF2 has a power-law-decay part for small clusters, and an increased probability (compared to the power-law decay) for large cluster size. The large clusters are randomly distributed in space, and move in all directions. The rods inside the same cluster are well polarized, thus the cluster still shows a good motility. These large motile clusters generate a large flux of mass inside the system, and thereby cause strong density fluctuations. Increasing ρ_r or decreasing σ^2, shifts the prominent shoulder to larger cluster size.

When ρ_r is high and σ^2 is low, we find the third type of PDF (denoted PDF3), as shown in Fig. 3.3. Giant clusters containing a large fraction of particles are formed. These huge clusters are usually formed by the collision of several large clusters in a short time from different directions. The rods block each other, thus the propelling forces are balanced with each other and the mobility of the giant cluster is very small.

PDF3 has two parts which arise from different spatial regions in the system. A peak at large n represents the size of giant clusters. For small n, PDF3 only has a peak for very small cluster, corresponding to some freely swimming rods not collected by the giant cluster. Since most of the rods are in the giant clusters, the average rod density outside the giant clusters is very low.

3.1.2 The exponent β of power-law decay of PDF

In the rSPP simulations, both PDF1 and PDF2 have a power-law-decay part for small clusters. The exponent β is a function of system parameters like ρ_r and σ^2. In
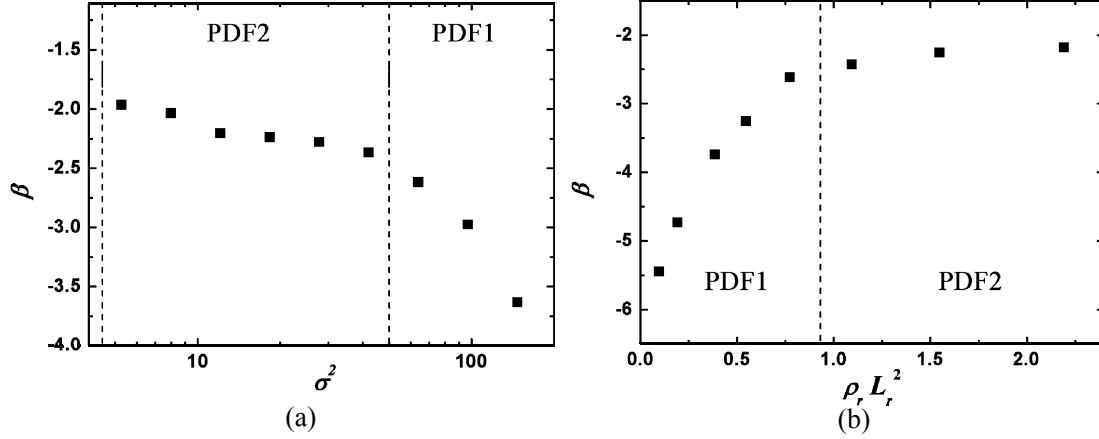
Figure 3.4: The exponent β of the power-law-decay part of PDF as a function of (a) the environmental noise σ^2 with $\rho_r L_r^2 = 0.7744$ and (b) the rod density $\rho_r L_r^2$ with $\sigma^2 = 2^{6.0} = 64$.

both PDF1 and PDF2 regions, β increases with increasing ρ_r and decreases with increasing σ^2 (Fig. 3.4). However, the changing rate of β varies in the PDF1 region always much faster than in the PDF2 region. The exponent β approaches –2 in the PDF2 region.

The power-law distribution of self-propelled rods indicates several basic properties of the system:

(1) The system is far from the thermal equilibrium state, and is not approaching thermal equilibrium. In our simulation, there is an energy input to maintain the particle motion, and energy dissipation due to friction.

(2) The elements of the system are not performing Brownian motion. The particles are self-propelled with directed motion despite of a random noise.

(3) There is cooperation between particles. Although there is no attractive potential between particles, the cooperation tendency is strong enough to aggregate the particles into clusters.

3.1.3 Balance between cluster formation rate and break-up rate

The Smoluchowski coagulation equation is an integral-differential equation introduced by Marian Smoluchowski in 1916, to describe the evolution of the number density of clusters of size n at time t.

Suppose a system consists of monomers which aggregate into clusters of different sizes. The evolution of the number density $\Pi(n, t)$ of clusters of size n at time t is described by Smoluchowski coagulation equation [97]:

$$\frac{\partial \Pi(n,t)}{\partial t} = \frac{1}{2}\sum_{i=1}^{n} K(n-i,i)\Pi(n-i,t)\Pi(i,t) - \sum_{i=1}^{\infty} K(n,i)\Pi(n,t)\Pi(i,t) \quad [3.1]$$

The original Smoluchowski equation only considers the aggregation of clusters. The break-up term is not included in the equation. The first term on the right side of Eq.

3.1 describes the formation of a cluster of size *n* from clusters of size *i* and *n-i*. The second term is the decrease of the number of the clusters of size *n* when they form a larger cluster by aggregation with another cluster of size *i*. The operator, $K(i, j)$, is known as the coagulation kernel and describes the rate at which the clusters of size *i* coagulate with the cluster of size *j*. In most of cases, $K(i, j)$ has a complex form. For example, if all particles and clusters are moving as ideal-gas molecules and aggregate after collisions, then *K* is,

$$K(i,j) = \sqrt{\frac{\pi k_B T}{2} \left[\frac{1}{m(i)} + \frac{1}{m(j)} \right]^{1/2}} \left[d(i) + d(j) \right]^2 ,$$

where $m(i)$ is the mass of cluster and $d(i)$ is the scattering size.

The Smoluchowski equation has two assumptions. First, only two-body coagulation is taken into consideration, multi-body collisions are neglected. In the ideal-gas model, this assumption is valid, because the number density of clusters is very low, thus the chance to have multi-cluster collisions is small. Second, the collision time of two clusters is shorter than the time interval Δt of the discrete form of Eq. 3.1. If one takes the continuous form or $\Delta t \rightarrow 0$, the collision time is negligible to the average time for a cluster to meet another one. This also corresponds to the low density region.

The Smoluchowski equation was also combined with a mean-field approximation to analyze the long-range order and phase behavior of rSPP [24]. By using the Smoluchowski equation, Peruani et al [25] distinguished two clustering regions by looking at the transition from a unimodal shape to a bimodal shape of the weighted-cluster-size distribution function. It is assumed that the cluster only loose one monomer each time and that the speeds of all clusters is the same. However, the one-monomer-loss assumption seems not to be a good approximation of the clustering behavior in our simulation. A large cluster breaks up into any size depending on the collision with other clusters. On the other hand, the swimming speed of different cluster is not unique due to different cluster configurations.

A modified Smoluchowski equation, which takes into account not only cluster aggregation but also break-up, can be written as,

$$\frac{\partial \Pi(n)}{\partial t} = \frac{1}{2} \sum_i^n K_+(i, n-i) \Pi(i) \Pi(n-i) - \sum_i K_+(i,n) \Pi(i) \Pi(n)$$

$$+ \sum_i K_-(i,n) \Pi(n+i) - \frac{1}{2} \sum_i^n K_-(i,n-i) \Pi(n) \qquad\qquad [3.2]$$

The first and second terms are the original terms of the Smoluchowski equation, which represents the collision of clusters. $K_+(i,j)$ is the cluster formation rate of two

clusters of size i and j to form a larger cluster of size $i+j$. The third and fourth term represents the break-up of clusters. $K_-(i,j)$ is the spontaneous break-up rate for a large cluster of size $(i+j)$ into two clusters of size i and j.

Note that we made several assumptions in Eq. 3.2. First, directly inherited from the assumptions of the original Smoluchowski equation, the density of clusters is very low. The cluster size is small enough compared with the average free gliding distance, so that the time interval between two collisions is much longer than the collision time for two clusters. Thus the collisions between more than two bodies are neglected. Second, for the break-up, only the case of a cluster splitting into two parts is considered. The noise of the system is assumed to be low that the decay time of clusters is longer than the collision time, thus the collapse of a large cluster into several small ones can be considered as the result of several break-up steps.

Eq. 3.2 helps to understand the properties of the system. For the stationary state, $\partial\Pi(n)/\partial t=0$ and all coefficients on the right side of Eq. 3.2 are independent of time. In the special case that the formation rate $K_+(i,j)$ equals the break-up rate $K_-(i,j)$, the exponential function $\Pi(n) \propto e^{-An}$ is a stable root of $\partial\Pi(n)/\partial t=0$. Of course, in most cases, $K_+(i,j)$ does not equal $K_-(i,j)$.

The formation rate is the product of two parts, $K_+(i,j)=K'(i,j)\cdot C$, where C is the collision rate of clusters which increases with increasing cluster density. $K'(i,j)$ is the possibility to form the large cluster after collision, which is influenced by the cluster shape, velocity, environmental noise etc. $K_-(i,j)$ increases if the noise is increased.

Consider a stationary system with stable PDF. At an instance, we suddenly increase the rod density by adding new clusters according to the PDF, thus the PDF of the system is not changed at the moment. However, the cluster density increases, consequently the collision rate K_+ increase. The PDF has to adapt accordingly. The increased K_+ makes the probability density decrease for small cluster sizes and increase for large ones. Similarly, if we keep the rod density but increase the environmental noise, K_- increases and number density flows from large size to small size. So, if the system is in the PDF1 region, increasing rod density ρ_r or decreasing environmental noise σ^2 increase the exponent β (Fig. 3.4) and extend the power-law part of PDF1 to larger cluster size (Fig. 3.1). In the PDF2 region, this will slightly increase β (Fig. 3.4), at the same time the peak for large motile cluster increases and shift to larger size (Fig. 3.2).

3.1.4 Phase diagram

By systematically varying the rod density ρ_r and the environmental noise σ^2, we can construct a phase diagram with regions of different type of PDF (Fig. 3.5). From the diagram, we see clearly PDF1 at low density and high noise, PDF3 at high density
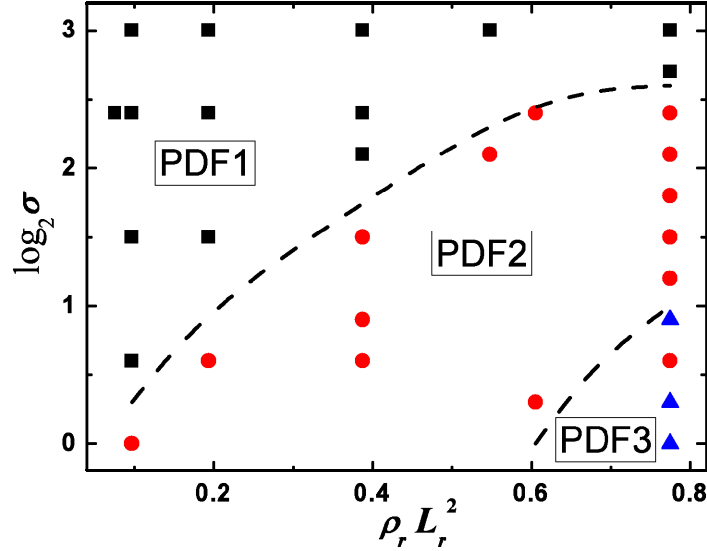
Figure 3.5: The phase diagram of three PDF type. The black squares (■) represent the system with PDF1; the red bullets (●) with PDF2; the blue triangles (▲) with PDF3. The dashed lines indicate the boundaries of different regions.

and low noise, and PDF2 in the transition region between PDF1 and PDF3.

The phase diagram is at the same time the phase diagram of the cluster configuration, from motile ones at low density and high noise region to immobile giant ones at high density and low noise region. The competition of two types of cluster configurations is responsible for the emergence of PDF1 and PDF3 in the different ρ_r and σ regions.

Note that all systems in Fig. 3.5 start from disordered states. The state with PDF2 is similar as the supercooled state of a liquid system below the freezing point. The PDF2 phase can be maintained until a "nucleus" for giant cluster is formed by the collision of several large and motile clusters from different directions. Several motile clusters happened to bounce into each other and form a blocked structure, which is smaller than the "giant" one at last. Then, the seed floats in space and gradually collects all rods through the random collision with other clusters. Then the system will transit to PDF3 phase. The system with $\log_2\sigma = 0.6$ has PDF2 although it has lower noise than the system with $\log_2\sigma = 0.9$ because the "nucleus" is not formed yet.

3.2 Cluster configuration

In the rSPP systems, although there are three kinds of PDF, we find only two types of cluster structures. One is the motile clusters in which the rods are polarized. Another is the giant clusters consisting of large number of rods blocking each other.

Systems of different types of clusters can be identified by analyzing the orientational correlation function. We define the orientation correlation function as

$$G(\mathbf{r}) = \left\langle \hat{\mathbf{u}}_i \cdot \hat{\mathbf{u}}_j \cdot \delta(\mathbf{r} - \mathbf{r}_{ij}) \right\rangle$$

Here $\hat{\mathbf{u}}_i$ is the unit vector of the orientation of rod i, $\mathbf{r}_{ij}(r, \phi)$ is the vector pointing from the center of mass of rod i to rod j, and ϕ is the angle between $\hat{\mathbf{u}}_i$ and $\mathbf{r}_{ij}$, as shown in Fig. 3.6. A clustering system always has high local order parameter as
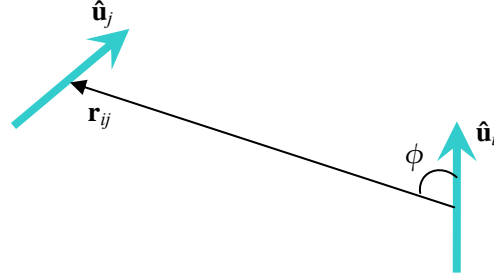

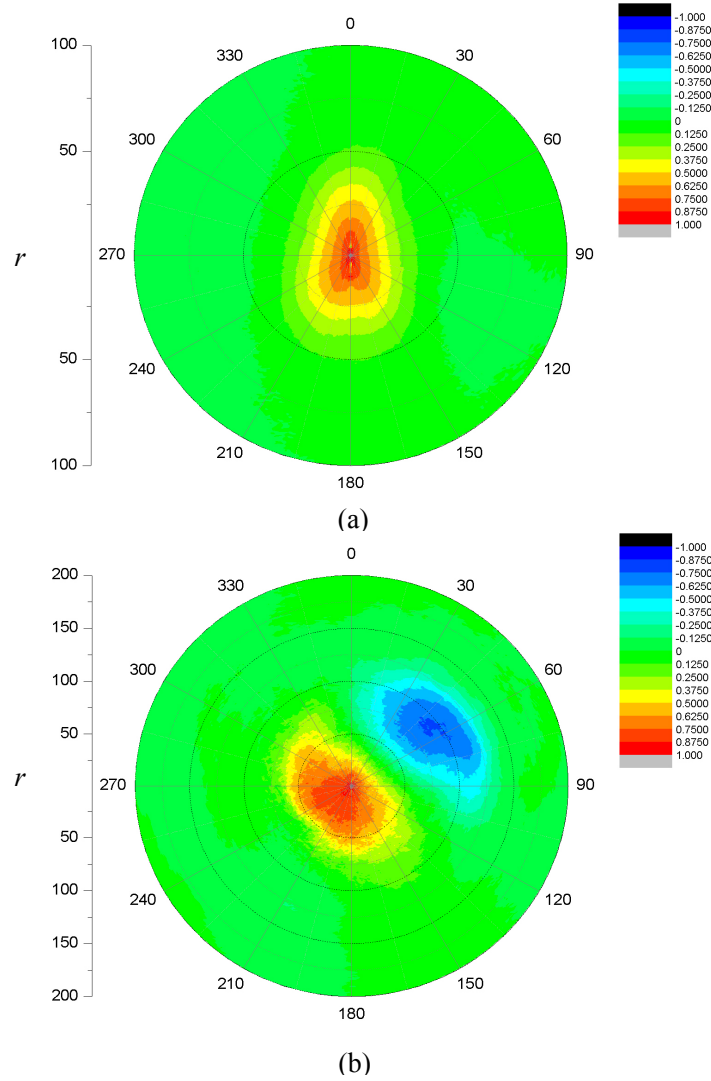Figure 3.6: Illustration of rod j in the coordinate system of rod i.

(a)

(b)

Figure 3.7: The correlation function $G(\mathbf{r})$ as the relative position $r_{ij}(r,\phi)$ to rod i (a) in the system of PDF2, $\rho_r L_r^2 = 0.7744$ and $\sigma^2 = 2^{3.6}$; (b) in the system of PDF3, $\rho_r L_r^2 = 0.7744$ and $\sigma^2 = 2^0$.

shown in Fig. 3.7, so that $G(\mathbf{r})$ has a peak at $r=0$. The correlation decreases with distance, and approaches zero at large distance, since there are no long-range interactions.

When motile clusters are dominant in the system, $G(\mathbf{r})$ is symmetric with a peak at $r=0$, reflecting the polarization inside clusters (see Fig. 3.7a). The correlated region gives information about the cluster configuration. The elongation of $G(\mathbf{r})$ in the directions $\phi=0°$ and $\phi=180°$ indicates that the large clusters extend slightly in the orientation direction. The width is narrower in the front and wider in the end. The large clusters have more chance to collide with other clusters head on than with their tails. The result of the collision can be increasing the cluster size by collecting the other clusters, or changing the directions of each cluster to be anti-parallel. The collision resulting in anti-parallel state is responsible for sharpening the front-end of large clusters.

If the largest cluster in the system is a giant cluster, $G(\mathbf{r})$ shows a very different picture (Fig. 3.7b). The peak with $G>0$ still stays at $r=0$, which stands for the high local-order-parameter for the close neighborhood of a rod. However, a region with negative correlations, $G<0$, develops, with its lowest value at a position (r',ϕ'). The largest r for non-zero $G(\mathbf{r})$ also represents the diameter of the giant cluster. Inside the giant cluster, because all rods point preferentially to the center of cluster, the propelling forces of rods block each other. So the locomotion speed of a giant cluster is far smaller than the gliding speed of a single rod. Also, the body force of the giant cluster implies a rotation motion due to the deviation of the rod orientation from pointing to the center of mass. Thus, ϕ' represents the rotational property. If $0°<\phi'<90°$, the cluster is rotating anti-clockwise; if $-90°<\phi'<0°$, it is rotating clockwise; if $\phi'=0°$, the propelling force inside the cluster are totally balanced, and the giant cluster is not rotating.

3.3 Average cluster size and weight

The average cluster size $<n>$ and weight $<w>$ of the system are

$$< n >= \sum_{n} n\Pi(n)$$

$$< w >= \sum_{n} n^2 \Pi(n) \Big/ \sum_{n} n\Pi(n)$$

where $\Pi(n)$ is the normalized PDF. The average cluster size $<n>$ is the ratio of the total cluster number and the total rod number. Since $\Pi(n)$ usually has much higher value for small n, the small clusters contribute more to $<n>$.

Fig. 3.8 shows the evolution of $<n>$ of PDF1 and PDF2 systems. At $t=0$, $<n>$ is approximately 1 due to the random initial state. $<n>$ increases with t until the system
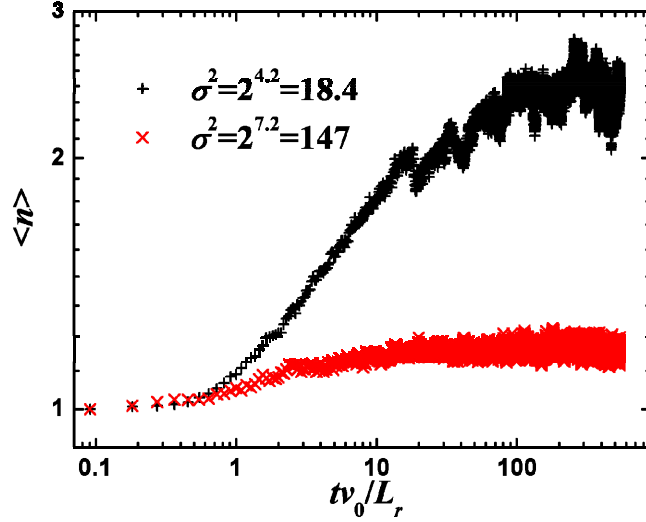
Figure 3.8: The average cluster size $<n>$ as a function of simulation time t. The density for both systems is $\rho_r L_r^2 = 0.7744$. Symbols indicate systems with PDF2 (+), and PDF1 ($\times$).

reaches a stationary state with a stable PDF. For an infinitely large system, $<n>$ is a constant. However, due to the effect of the finite simulation box size, $<n>$ fluctuates around a constant value, which we denote as $\bar{n}$. Similarly, $<w>$ fluctuates around a constant value $\bar{w}$. The amplitude of the fluctuation is inverse to the simulation box size.

We average $<n>$ and $<w>$ over time and obtain $\bar{n}$ and $\bar{w}$ as a function of the environmental noise σ^2 and the rod density ρ_r, as shown in Fig. 3.9 and Fig. 3.10. $\bar{n}$ and $\bar{w}$ increase with increasing ρ_r and decreases with increasing σ^2. In the low-density limit, the rods hardly can find each other. In the high σ^2 limit, the noise quickly separates rods in the same cluster. So, the values of $\bar{n}$ and $\bar{w}$ approach 1 in these limits, which means a suspension of single particles.
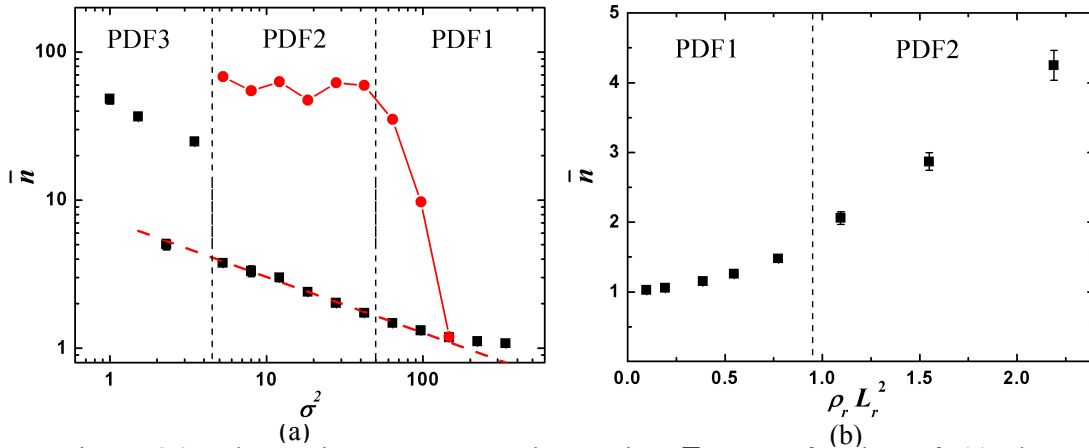
Figure 3.9: The stationary average cluster size $\bar{n}$ as a function of (a) the environmental noise σ^2 with $\rho_r L_r^2 = 0.7744$ and (b) the rod density $\rho_r L_r^2$ with $\sigma^2 = 2^{6.0} = 64$. The black squares (■) represent systems start with disordered state, while the red bullets (●) represent systems start with the initial state of a giant cluster. The dash line is the power-function fitting.
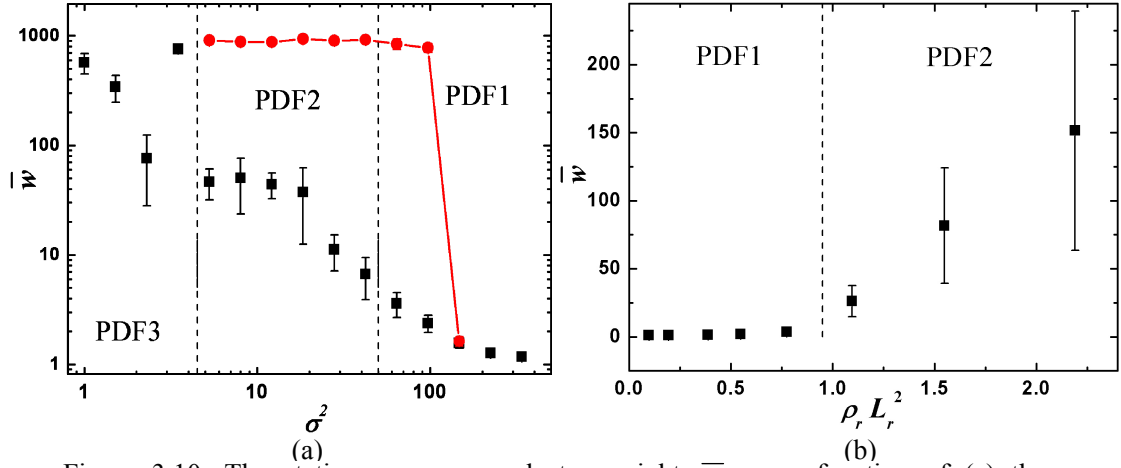
Figure 3.10: The stationary average cluster weight $\overline{w}$ as a function of (a) the environmental noise σ^2 with $\rho_r L_r^2 = 0.7744$ and (b) the rod density $\rho_r L_r^2$ with $\sigma^2 = 2^{6.0} = 64$. The black squares (■) represent systems start with disordered state, while the red bullets (●) represent systems start with the initial state of a giant cluster.

Interestingly, $\overline{n}$ shows a power-law decay with σ^2 in the PDF1 and PDF2 regions if the system starts from a disordered state, see Fig. 3.9a. The PDF2 phase is the "supercooled" state which will transit to PDF3 phase once a nucleus of a giant cluster is formed. If the initial state has a giant cluster, the system stays in the PDF3 phase unless the noise is large enough to break the giant cluster, as indicated in Fig. 3.9a and Fig. 3.10a. The power-law relation suggests that the cluster size diverges when the noise approaches zero, even though the system is in "supercooled" state.

3.4 Density fluctuation

The variance of density fluctuation in a fixed volume V is

$$\Delta N = \sqrt{<\left(N - \lambda\right)^2>} \sim \lambda^{\beta_{dens}} \qquad [3.3]$$

where N is the particle number in volume V, and $\lambda = \rho_r V$ is the anticipated particle number in a fixed volume V. ΔN grows as $\lambda^{\beta_{dens}}$.

Fig. 3.11 plots ΔN as a function of the anticipated number λ in a log-log scale. For systems in PDF1 and PDF2 regions in the phase diagram, the density fluctuations have two parts. If we analyze the density in a small observation volume (corresponding to small λ), the exponent β_{dens} is much larger than 1/2. With increasing observation volume, the exponent β_{dens} decreases and approaches 1/2. ΔN gradually transforms from the giant-fluctuation region to the normal-fluctuation region. The transition occurs at larger λ for system with smaller noise.

Fig. 3.12 shows the exponent β_{dens} of Eq. 3.3 as a function of the environmental noise σ^2 and the rod density ρ_r. At high density or low noise, β_{dens} approaches 1, corresponding to the strong aggregation limit. At very high σ^2, the fluctuations dominate the self-propelled motion and the aggregation tendency. At low density, the time for a freely gliding rod to find another to form a cluster is much longer than the
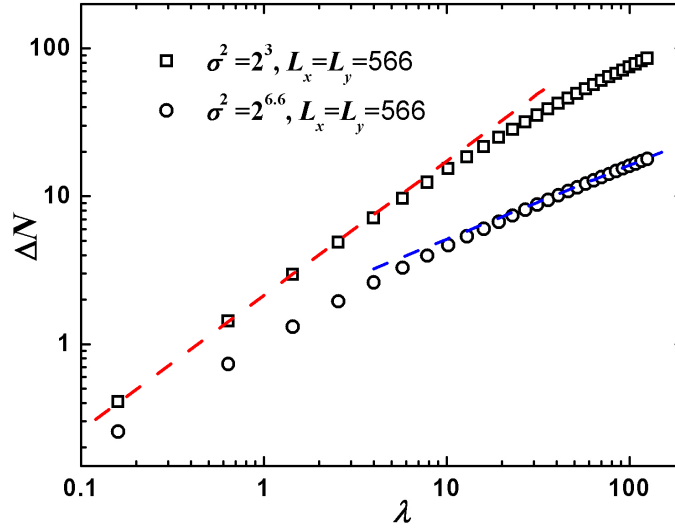
Figure 3.11: The mean square root of rod number variance ΔN as a function of the mean number of rods λ in a volume of size V. The slopes of the red and blue dashed lines are 0.91 and 0.50, respectively. Two sequences of data correspond to systems with the same rod density $\rho_r L_r^2 = 0.7744$ and the same simulation box size $L_x \times L_y = 566 \times 566$, but different noise level as indicated. Symbols indicate systems of PDF2 ($\square$) and PDF1 ($\circ$).

average time of two rod cooperation before the environmental noise separates them. Thus, the exponent β_{dens} decreases with increasing σ^2 and decreasing ρ_r.

Since β_{dens} is related to the degree of aggregation, we also plot it as a function of average cluster size $\bar{n}$ (Fig. 3.13). Both β_{dens} and $\bar{n}$ are quantities reflecting the aggregation degree of the system. Thus β_{dens} increases with $\bar{n}$. The stronger the system aggregates, the larger is β_{dens}.

The density fluctuations obey a Poisson distribution for a thermal equilibrium system with $\beta_{\text{dens}} = 1/2$. In a swarming system, there are giant density fluctuations for which β_{dens} is greater than $1/2$ and sometimes approaches 1. The giant number fluctuations are a signature of an aggregating system [44].

(a)

(b)
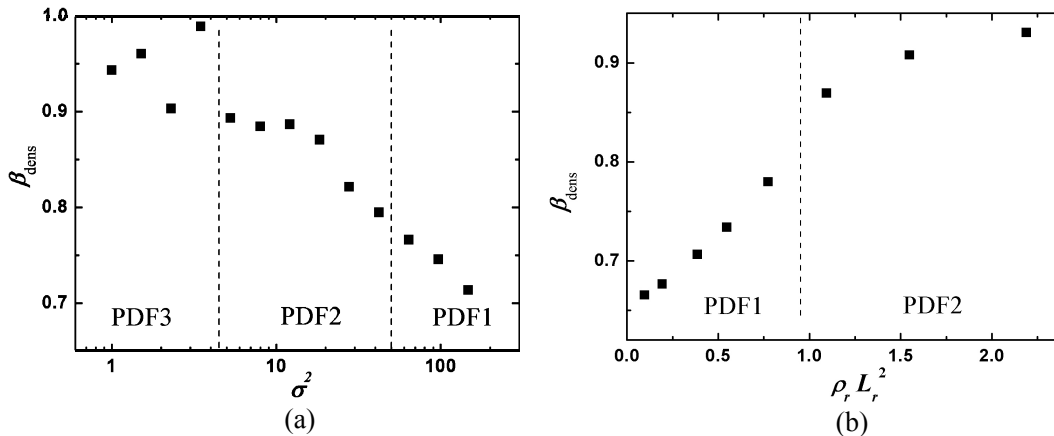
Figure 3.12: The exponent β_{dens} of $\Delta N(\lambda)$ for small rod numbers λ as a function of (a) environmental noise amplitude σ^2 with $\rho_r L_r^2 = 0.7744$ and (b) the average rod density $\rho_r L_r^2$ with $\sigma^2 = 2^{6.0} = 64$. The corresponding PDF type is marked on the diagram.
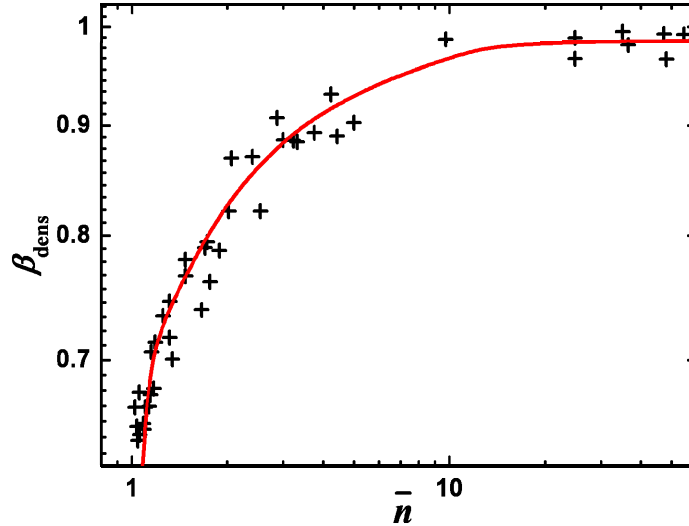
45

Figure 3.13: The exponent β_{dens} as a function of average cluster size $\bar{n}$ of systems in the phase diagram.

Usually, $\beta_{\text{dens}}=1/2$ represents a disordered state with no aggregation. However, PDF1 and PDF2 systems still have a strong aggregation tendency, although the density fluctuations approach the same behavior as disordered system at large observation volume. For a system with stronger aggregation, we need a larger observation scale to see the normal density fluctuation region. The transition point between normal density fluctuation and giant density fluctuation can be used to characterize the degree of aggregation of the system. If we observe below this characteristic size-scale, the fluctuations are strong, the swarming behavior is dominant and the aggregation tendency is strong. Above that size-scale, the density fluctuations increase as the square root of observation box size as in thermal equilibrium systems, and the system behaves more like a disordered system.

3.5 Cluster speed

We calculate $<\mathbf{v}^2>^{1/2}$ as a function of cluster size n, as shown in Fig. 3.14. The velocity $\mathbf{v}$ is determined from the displacement of the center of mass in a time interval $\Delta t=100$. As shown in Fig. 3.14, $<\mathbf{v}^2>^{1/2}$ decreases with the cluster size. For the motile clusters, shown in the snapshots in Fig. 3.1 and Fig. 3.2, $<\mathbf{v}^2>^{1/2}$ decreases quite slowly. For the giant clusters shown in Fig. 3.3, the rods block each other strongly, so that the velocity decreases much faster. Since the rods are arranged like an inner radius structure, the moving velocity and the rotating speed depends on the structure defects of the giant cluster.

The motility of a cluster strongly depends on its configuration. The average velocity vector of all clusters vanishes, because the system does not have long-range order of velocity orientations. Although the rods are polarized locally, the orientation of the whole cluster changes with time. The forward speed $v_0=0.01$ of a freely gliding
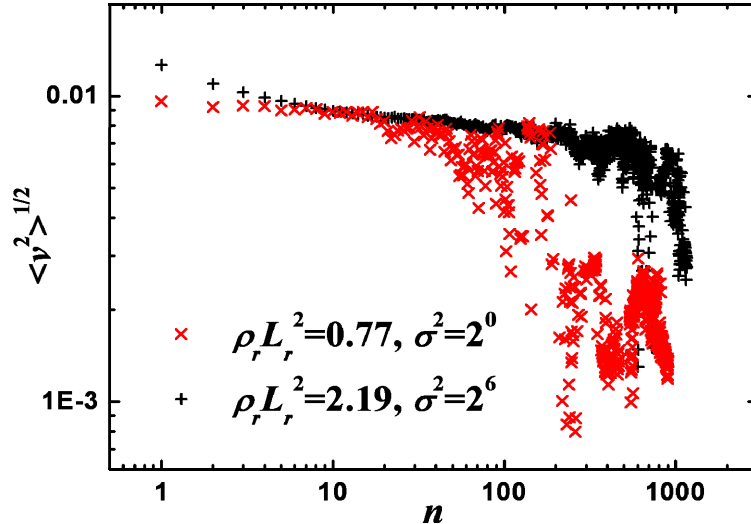
Figure 3.14: The center-of-mass velocity as a function of cluster size. The system with $\rho_r L_r^2$=0.7744 and $\sigma^2=2^0$=1 has PDF3 and giant clusters are formed (×). The system with $\rho_r L_r^2$=2.1901 and $\sigma^2=2^6$=64 has PDF2 and does not have giant clusters (+).

rod is a system parameter. $<\mathbf{v}^2>^{1/2}$ is greater than v_0 for small n when the environmental noise is strong. As the cluster size increases, the noise has less influence on the cluster velocity. If the particles are passive, then the variance of velocity distribution of a cluster is proportional to the inverse of the square root of n. For a cluster consisting of n rSPP, the center-of-mass velocity is not only influenced by the environmental noise, but also by the cluster configuration. The rods can block each other because they are self-propelled by a constant force along their long axis. The slowing-down of motile clusters with mid size is due to a few rods which partially block the motion of the cluster, so that the cluster as a whole still keeps a reasonable moving speed.

3.6 Cluster life time

We define the life time of a cluster as the length of the time during which its members do not change. Fig. 3.15 and Fig. 3.16 show T_{life}(n) as a function of cluster size n. The average life time of clusters, $T_{\text{life}}(n)$, is not only a function cluster size n, but also of the rod density ρ_r and the environmental noise σ^2. The higher the cluster number density, the higher is the collision rate, thus the shorter the average cluster life time will be. The noise σ^2 determines the rate of cluster break-up. Thus their life time is shorter with larger σ^2.

Note that the life time of a cluster is analyzed with time interval Δt=100. Thus, cluster life times $T_{\text{life}}(n)<\Delta t$ cannot be resolved. The average life time decreases with the size of cluster. Usually, we have much more samples for small clusters than larger ones due to the power-law PDF. Also, larger clusters have more possible configurations. Thus, $T_{\text{life}}(n)$ for small n has much better statistics. The life time for size n=1 is always much higher than other cluster sizes.
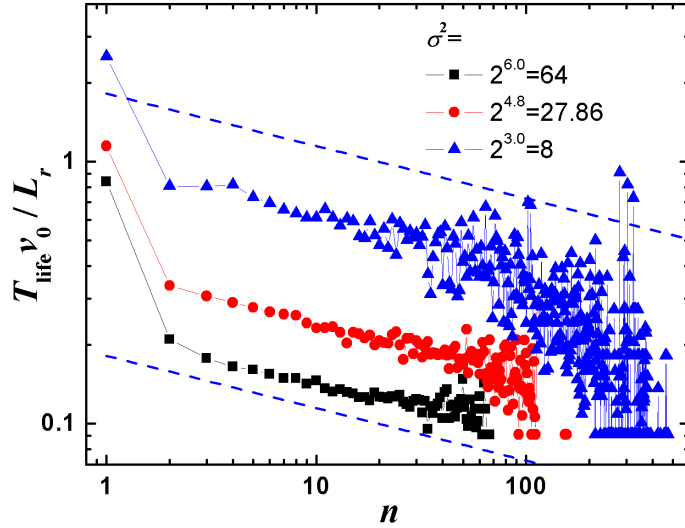
Figure 3.15: The cluster life time $T_{life}(n)$ of different size in systems with same rod density $\rho_r L_r^2 = 0.7744$ but different noise, as indicated. The dashed lines are power law functions with exponent -0.20.

The "cluster" of size $n=1$ is special because a single rod can not "break up" into smaller clusters. results in a much longer life time than cooperating clusters. For $n \geq 2$, $T_{life}(n)$ decreases smoothly with the cluster size. For $n > 30$, the data become very noisy due to bad statistics. Also, the data for $T_{life}(n) \sim 100$ is strongly influenced by our analyzing time step size $\Delta t = 100$. The data for mid-size clusters ($2 < n < 30$) shows an interesting power-law dependence

$$T_{life} \sim n^{\beta_{life}}$$

The exponent β_{life} is plotted as a function of σ^2 and ρ_r in Fig. 3.17. β_{life} stays near the value -0.2, except for a low density $\rho_r L_r^2 = 0.0968$, essentially independent of ρ_r and σ^2.

Fig. 3.18 shows $T_{life}(n)$ for $n=1$ to $n=5$ as a function of ρ_r and σ^2. The life time
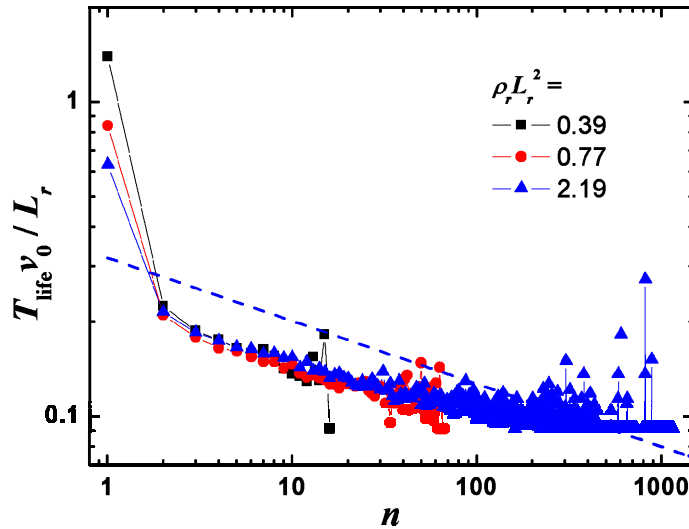

Figure 3.16: The cluster life time $T_{life}(n)$ of different size in systems with same noise $\sigma^2 = 2^{6.0} = 64$ but different rod density, as indicated. The dashed lines are power functions with exponent -0.20.
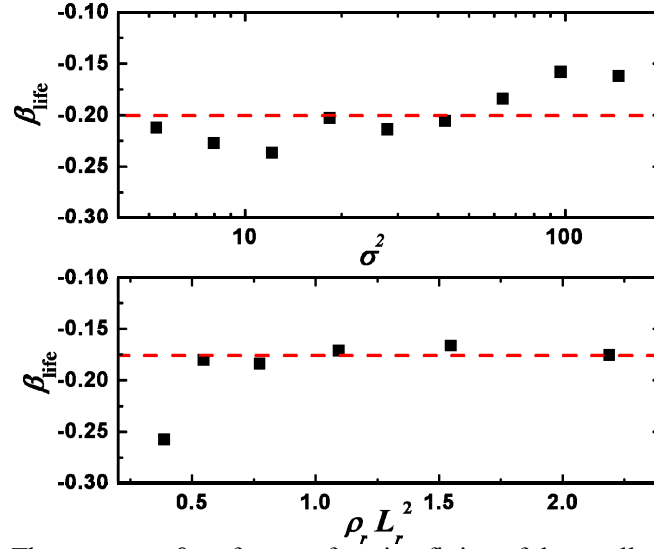
Figure 3.17: The exponent β_{life} of power-function fitting of the small size part of cluster life time function.

$T_{\text{life}}(n)$ for n≥2 is independent of ρ_r, in agreement with Fig. 3.16. In contrast, $T_{\text{life}}(1)$ decreases strongly with increasing density.

The life time of single rods reflects their cluster forming rate by collision. A simple explanation of the relation between life time and rod density can be obtained as follows. Suppose that all clusters and single rods are distributed randomly in the space. According to Fig. 3.14, the forward velocities of the motile clusters do not change too much with the cluster size. Thus, we assume that all clusters have a same velocity v_0=0.01. Suppose the average distance between clusters is large, so that the clusters move ballistically. Then, the frequency of collisions of a single rod is

$$f_{collision} \sim v_0 \cdot \sum_n \sqrt{n} \rho'_c(n) \qquad [3.3]$$

where $\rho'_c(n)$ is the number density of clusters of size n. We approximate the scattering cross section of a cluster of size n by $\sqrt{n}$. Since the collision is between an "immobile" cluster of size n and a single rod, we neglect the rod width which is small comparing with the scattering section of the cluster. Rewriting Eq. 3.3, we obtain
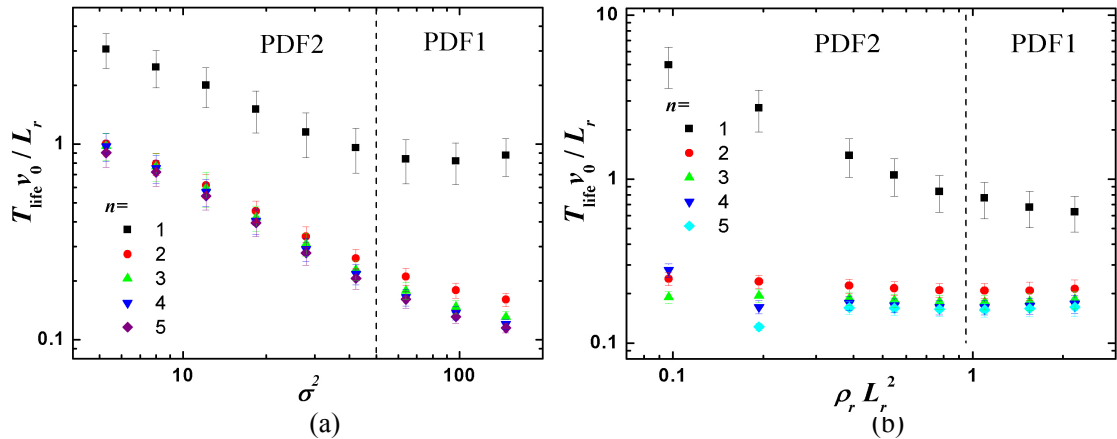

Figure 3.18: The life time T_{life} of clusters of size n=1~5 as functions of (a) the environmental noise σ^2 with $\rho_r L_r^2$=0.7744 and (b) the rod density $\rho_r L_r^2$ with $\sigma^2=2^{6.0}$=64.
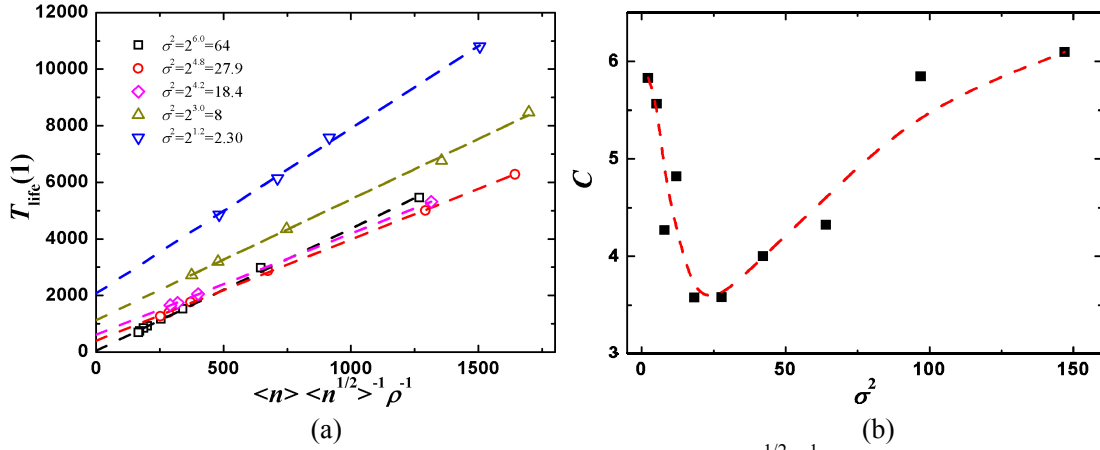
Figure 3.19: (a) The linear relation between $T_{\text{life}}(1)$ and $<n><n^{1/2}>^{-1}\rho$. (b) The slope C of fit lines in (a) as a function of the environmental noise σ^2.

$$f_{collision} \sim <v> \cdot \sum_n \sqrt{n} \frac{\rho'_c(n)}{\rho_c} \rho_c = <v> \cdot \rho_c \cdot \sum_n \sqrt{n}\Pi(n) = <v> \cdot \rho_c \cdot <\sqrt{n}>$$

where $\rho_c = \sum \rho'_c = \rho_r/<n>$ is the total cluster number density. The life time is proportional to the inverse of the collision rate,

$$T_{life}(1) = \frac{1}{f_{collision}} \sim C \frac{<n>}{<v> <\sqrt{n}> \rho_r^{-1}}$$

where $<n>$ is the average cluster size, $C(\cdot)$ is a function of quite a few parameters, such as environmental noise σ^2, the rod length and width, etc, but not a function of rod density ρ_r. So, if we fit all the system parameters, C is just a constant.

We plot $T_{\text{life}}(1)$ versus $<\sqrt{n}>^{-1} \rho_r^{-1} <n>$ in Fig. 3.19a. The data fit a linear relation quite well. The fit lines have an off-set for small noise σ^2. The off-set is due to the assumptions and approximations of the calculation. The slope of the fitting line as a function of the environmental noise σ^2 is shown in Fig. 3.19b. It decreases for small σ^2 and increases for large σ^2.

3.7 Finite-size effects

In our simulations, we employ periodic boundary conditions. The finite box size implies a finite number of particles. The cluster size can never be larger than the total particle number [89]. Thus, all quantities related to cluster size, such as PDF, average cluster size and weight, are affected accordingly. Similarly, the density fluctuations at the scale of the simulation box are suppressed. The statistical results approach their value for infinitely large systems with increasing the simulation box size.

3.7.1 Effects on PDFs

The effect of simulation box size on PDFs is shown in Fig. 3.20. The lack of the contribution of break-up of clusters larger than total particle number reduces the PDF
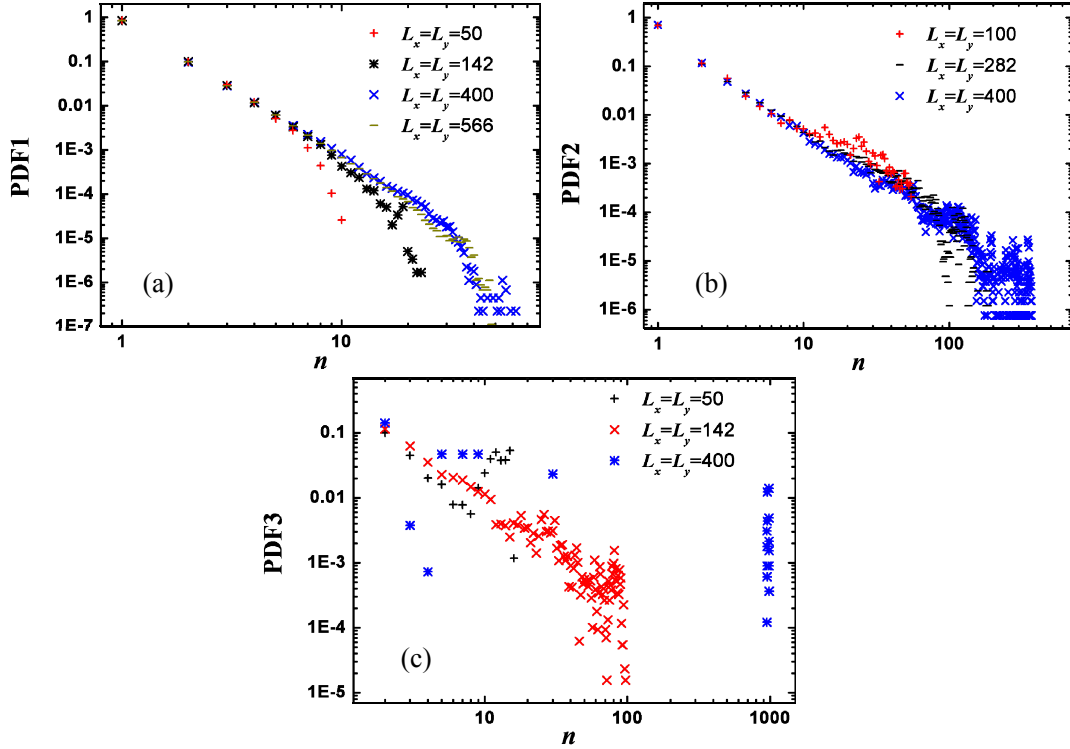
Figure 3.20: PDFs with different simulation box sizes of systems (a) $\rho_r L_r^2 = 0.7744$ and $\sigma^2 = 2^{6.6} = 97$ with PDF1, (b) $\rho_r L_r^2 = 0.7744$ and $\sigma^2 = 2^{3.0} = 8$ with PDF2 and (c) $\rho_r L_r^2 = 0.7744$ and $\sigma^2 = 2^0 = 1$ with PDF3.

for large n. This shortage can affect the exponent of the power-law part.

Fig. 3.20a shows PDFs of a system of $\rho = 6.4 \times 10^{-3}$, $\sigma^2 = 2^{6.6} = 97$ and different simulation box size. The simulation of the largest box ($L_x = L_y = 566$) has a PDF of type PDF1. The PDFs of small box size ($L_x = L_y = 50, 142$) still obey a power law decay for small clusters without obvious change of the exponent, and they deviate when n approaches the total particle number. When the simulation box is large ($L_x = L_y = 400$, 566), the PDFs almost overlap each other, and show the drop-off for large cluster sizes at the same place. Thus systems larger than $L_x = L_y = 400$ are large enough for PDF1 to be unaffected by finite size effects.

Fig. 3.20b shows the finite-size effects on PDF2. Similar as for PDF1, the power-law part extends with increasing box size. The exponents of the power-law stay near $\beta = -2$. The shoulder moves to larger cluster size when the simulation box size is enlarged.

Fig. 3.20c shows the finite-size effects on PDF3. The limited total particle number has the most profound influence to PDF3 systems, comparing with the other types. When the system is too small, the total rods number is not sufficient to form a blocked structure. The PDF is of type 2 instead of type 3 in an insufficiently large system. Thus, the total number must be large enough for a blocked cluster. In most of our simulation, the total number of rods is more than 1000, which is enough for a blocked cluster.
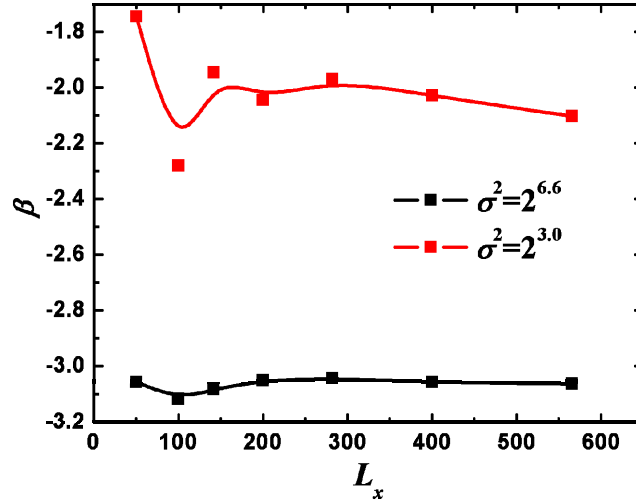
Figure 3.21: The exponent β of power-law part in PDF is plotted as a function of side length L_x of simulation box. The rod density is $\rho_r L_r^2 = 0.7744$. The system of red square (■) sits in PDF2 region on the phase diagram, while the system of black square (■) in PDF1 region.

By looking at the influence of box size to PDF, we found that, except for PDF3, the basic shape and type of PDF1 and PDF2 does not change. The transition point to the drop-off in PDF1, and the peak or shoulder of PDF2, shift their position with box size.

Fig. 3.21 shows the exponent β of PDF1 and PDF2 as a function of the side length L_x of the simulation box. It fluctuates strongly with small simulation boxes, and converges for large box sizes.

3.7.2 Influence on average cluster size and weight

The dependence of stationary cluster size $\bar{n}$ and $\bar{w}$ on the side length L_x of the simulation box is shown in Fig. 3.22. For the systems of PDF1 and PDF2, $\bar{n}$ increases with small L_x and converge, while $\bar{w}$ is divergent. For the system of PDF3, both $\bar{n}$ and $\bar{w}$ are divergent.

Suppose the cluster-size distribution of an infinitely large system obeys a power law,

$$\Pi(n) = \frac{1+\beta}{N^{1+\beta}-1} n^{\beta}, \quad \beta < -1 \tag{3.5}$$

$$\sum_{n=1}^{N} \Pi(n) = 1$$

N is the total number of rods in the system and $N \gg 1$. We assume that the system is not large enough to exhibit the strong decay for large cluster numbers. The sharp drop due to the limited box size is neglected. The average cluster size of the system is then easily calculated to be
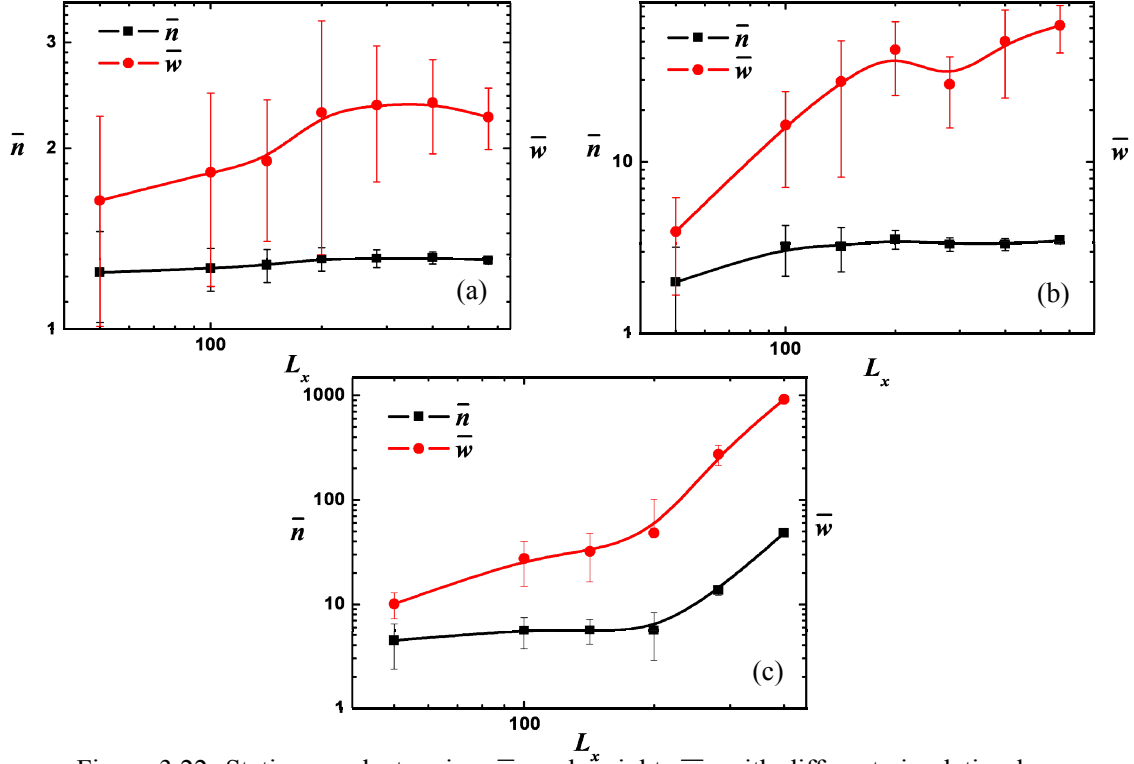
Figure 3.22: Stationary cluster size $\bar{n}$ and weight $\bar{w}$ with different simulation box sizes of systems (a) $\rho_r L_r^2=0.7744$, $\sigma^2=2^{6.6}=97$ and $\beta=-2.98$ with PDF1, (b) $\rho_r L_r^2=0.7744$, $\sigma^2=2^{3.0}=8$ and $\beta=-2.04$ with PDF2 and (c) $\rho_r L_r^2=0.7744$ and $\sigma^2=2^0=1$ with PDF3.

$$
<n> = \begin{cases} \dfrac{1+\beta}{2+\beta}\dfrac{N^{2+\beta}-1}{N^{1+\beta}-1}, & \beta \neq -2 \\[2ex] \dfrac{1}{1-N^{-1}}\ln N, & \beta = -2 \end{cases}
$$

If N is sufficiently large, the average cluster number takes the simpler form,

$$
<n> = \begin{cases} \dfrac{-\beta-1}{2+\beta}N^{2+\beta}, & -2<\beta<-1 \\[2ex] \dfrac{-\beta-1}{-\beta-2}, & \beta<-2 \end{cases}
$$

[3.6]

When $\beta>-2$, the average cluster size strongly depends on the total number of rods in the system. But $<n>$ is independent of N if β is smaller than -2. For very large β, $<n>$ approaches 1, which means nearly all rods are gliding freely.

From the size distribution, it is easy to obtain the weight distribution,

$$
\Pi_w(n) = \frac{2+\beta}{N^{2+\beta}-1}n^{\beta+1}, \quad \beta<-2
$$

Similarly, the average weight of clusters for sufficiently large N is

Figure 3.23: The density deviation ΔN as a function of average particle number λ in the observed space. The data is for system with same parameters ρ_r and σ^2 but different box size in systems of (a) $\rho_r L_r^2 = 0.7744$ and $\sigma^2 = 2^{6.6} = 97$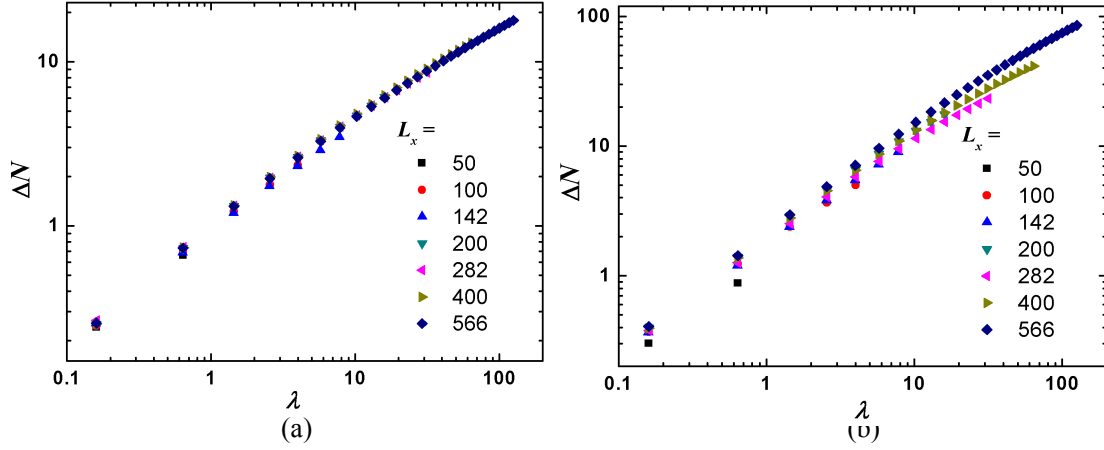 with PDF1 and (b) $\rho_r L_r^2 = 0.7744$ and $\sigma^2 = 2^{3.0} = 8$ with PDF2. These are the same systems as in Fig. 3.20.

$$
<w> = \begin{cases} \dfrac{-\beta-2}{3+\beta} N^{2+\beta}, & -3 < \beta < -2 \\[2mm] \dfrac{-\beta-2}{-\beta-3}, & \beta < -3 \end{cases}
$$

Thus, in the PDF1 region, if the total rod number is large, but not large enough to exhibit the crossover to an exponential decay, the average cluster size $<n>$ is convergent when $\beta < -2$, and the average cluster weight $<w>$ is convergent when $\beta < -3$.

3.7.3 Influence on density fluctuations

The giant density fluctuations at small observation scale are a typical signature of aggregation of rSPP systems. At large scale, the fluctuations are the same as in a thermal equilibrium state. Since the total particle number is a constant, the density fluctuations on the scale of simulation box size are zero. Thus the density fluctuations are suppressed at that size scale.

The density fluctuations $\Delta N(\lambda)$ of different box size are shown in Fig. 3.23. The system of $\rho_r L_r^2 = 0.7744$ and $\sigma^2 = 2^{6.6} = 97$ is located in the PDF1 region in the phase diagram. The systems with large size ($L_x = L_y \geq 282$), which have PDFs exhibiting the correct transition point, also have $\Delta N(\lambda)$ functions overlapping each other and have the same transition point from the giant density fluctuation region to normal fluctuations. For small systems ($L_x = L_y < 282$), the curves deviate before the transition point due to the constant rod number. Similarly, all $\Delta N(\lambda)$ in Fig. 3.23b deviate at different places. Thus, all systems of PDF2 have not yet reach a large enough size to show a correct $\Delta N(\lambda)$ function.

3.8 Conclusions

We have simulated systems of rSPP which are propelled by a constant force along their long axis. Without any attractive potentials, the rSPP exhibit aggregation behavior. Started from a random initial state, the system reaches a stationary state when the rate of cluster forming is balanced by the rate of break-up.

We found three types of PDF by changing the environmental noise σ^2 and rod density ρ_r, and get a state phase diagram by judging the type of PDF. At high σ^2 and low ρ_r, the system has PDF1, which shows a power-law distribution for small cluster sizes. The probability to find clusters larger than a critical size drops fast. At low σ^2 and high ρ_r, giant clusters consisting of the blocked rods are formed. The system has PDF3, which has a peak at the cluster size near the total particle number and a few floating rods and small clusters. Systems in an intermediate region of ρ_r and σ^2 have PDF2 which is a transit form between PDF1 and PDF3. The state of PDF2 is comparable to the supercooled state of a liquid system below the freezing point. Clusters in PDF1 and PDF2 systems retain high motility, whereas the giant clusters in PDF3 system is nearly immobile due to the blocked configuration.

Quantities directly related to PDF, such as average cluster size and weight, change with the system parameter ρ_r and σ^2. Especially, the average cluster size shows a power-law relation with σ^2 before entering the PDF3 state. Giant density fluctuation, which is an important character of SPP systems, is also found in our rSPP simulation.

Inspired by the two regions of PDF1 (power law decay for small size and a faster decay for large size) and two regions of density fluctuations of PDF1 systems (giant density fluctuation and normal density fluctuation), we make a hypothesis that there is a characteristic observation size for rSPP system. Below that size, the swarming behavior is dominant and the aggregation tendency is strong, while above that size the system behaves more like a disordered system.

IV.   Sinusoidal beating flagella in 2-dimensions

Flagella with their sinusoidal traveling wave of deform action, are the simplest systems in which the self-propulsion mechanism is taken into account explicitly. We consider here flagella of length $25a$ are embedded in a two-dimensional (2D) multi-particle collision dynamic (MPC) fluid. The viscosity of MPC fluid is $v=3.02$. The flagella of length $L_f=25a$ have an average spontaneous curvature $c_0=0$ and the beat frequency $f_0=1/120$, and swim forwards with the velocity $u_{single}=0.020\pm0.001$. The other parameters of the system are given in Chapter II. Thus, we estimate a Reynolds number $Re=2A_{tail}u_{single}/v \approx 0.04$ for our flagella model, where $A_{tail}=3.2a$ is the beating amplitude.

For the simulation with the anisotropic friction (AF), we choose the friction coefficient $\gamma_{\parallel} = 5$ and $\gamma_{\perp} = 8.4$. Thus the flagellum model moves forwards with a velocity of $u_{single}=0.020$ when $f_0=1/120$.

4.1 Single flagellum simulation in MPC fluid

We put a single flagellum in the simulation box of side length $L_x=L_y=100a$, which is four times the flagellar length and about 30 times the beating amplitude. Thus the simulation box is relatively large compared to the size of our flagellum.

Fig. 4.1 shows the square of the flagellum displacement, $<\mathbf{r}^2>$, as a function of the observation time interval Δt. On the diagram, there are two distinct regions. At the short time intervals, the flagellum mainly shows a linear motion with constant velocity, so that $<\mathbf{r}^2>$ is approximately proportional to Δt^2. When Δt is large, the flagellum behaves like a Brownian particle with random steps, $<\mathbf{r}^2>\sim\Delta t$. The
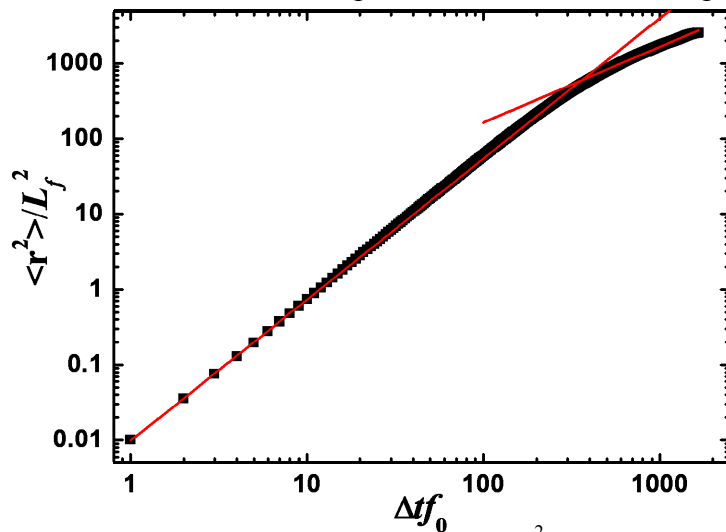
Figure 4.1: The square of displacement of flagella, $<\mathbf{r}^2>$, as a function of the time interval Δt. The power-law fit lines (red) have the exponent 1.9 and 1, respectively. The blue dashed line indicates the intersection of the fit lines located at $\Delta t f_0 \approx 360$.

intersection of the fit lines for different parts of the curve is located at $\Delta tf_0 \approx 360$. The persistence length of the oriented motion is about 25 flagellar lengths. Thus the effect of the thermal fluctuations on the self-propelled motion is negligible in our simulation for $\Delta tf_0 < 360$. Thermal fluctuations are important only for very long time intervals.

4.2 Two flagella cooperation through hydrodynamic interaction (HI)

Two flagella are put into a MPC fluid with straight and parallel configurations with a distance of $1.5a$ in between, as shown in Fig. 4.2a. They start to beat with the same initial phases ($\varphi_1=\varphi_2=0$), but different frequencies ($f_1=1/120 \times 0.999$ and $f_2=1/120$ with only 0.1% difference). Due to the synchronization and attraction effects, they swim together for a long time, keep in touch and gradually change the relative positions according to the increasing phase difference $\Delta\varphi$. The flagella are always synchronized when the phase difference is small, as shown in Fig. 4.2b-d. In Fig. 4.2e, the phase difference is too large to maintain the cooperation. So the flagella separate and go in different directions.

We track the distance (d) between the front particles of two flagella, and plot it as a function of the simulation time, as shown in Fig. 4.3. The phase difference $\Delta\varphi$ is proportional to time,

$$\Delta\varphi = 2\pi(f_2 - f_1)t .$$

Therefore, the x-axis in Fig. 4.3 is also $\Delta\varphi$. A remarkable linear relation between the distance d and the simulation time t, or between d and phase difference $\Delta\varphi$, is shown, which indicates the cooperating flagella pair with their shape locked in phase. Although there are some fluctuations in the data, the linear part extends until $tf_2 \approx 416$ and $\Delta\varphi \approx 0.83\pi$. Then the distance increases suddenly because the cooperation between the flagella is disrupted, and two flagella are swimming separately. Due to the periodic boundary condition, these flagella can meet again later and make a new cooperating pair. The linear part with negative slope on the right side of the diagram corresponds to the time that the cooperation is rebuilt.

(a)   (b)   (c)   (d)   (e)
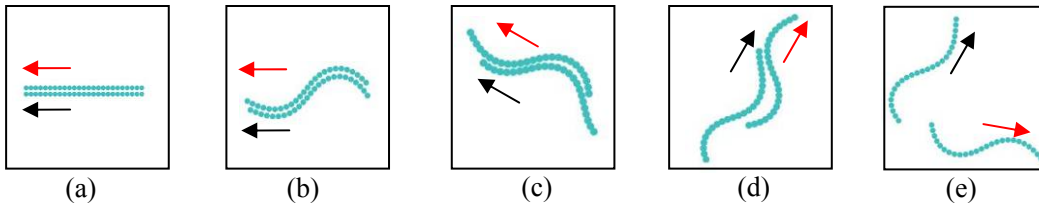
Figure 4.2: The snapshots of two flagella simulation with 0.1% difference of beat frequency. The frequency of the flagella are $f_1=1/120 \times 0.999$ (the swimming direction is indicated by black arrows) and $f_2=1/120$ (the swimming direction is indicated by red arrows). (a) $tf_2=0$, $\Delta\varphi=0\pi$, (b) $tf_2=1$, $\Delta\varphi=0.002\pi$; (c) $tf_2=200$, $\Delta\varphi=0.4\pi$; (d) $tf_2=400$, $\Delta\varphi=0.8\pi$; (e) $tf_2=460$, $\Delta\varphi=0.92\pi$.
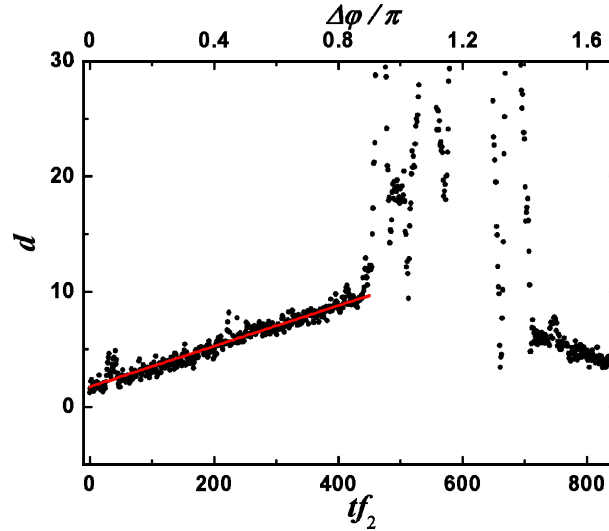
Figure 4.3: The distance d between the front particles of two cooperating flagella as a function of time t and phase difference $\Delta\varphi$. The red line is the linear fitting of the data when two flagella are cooperating.
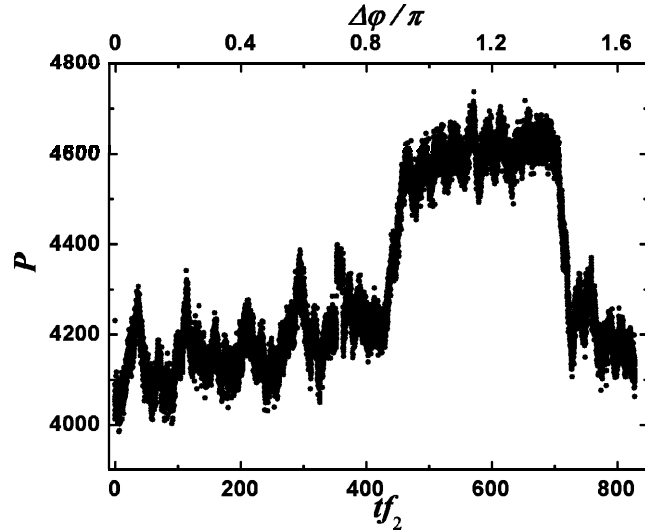
Figure 4.4: The energy consumption P per beat of two cooperating flagella system as a function of time t and phase difference $\Delta\varphi$.

Fig. 4.4 shows the energy dissipation or energy consumption P per beat of the two-flagellum system. Each data point is averaged over 10 beats, in order to smooth the curve. However, the data still fluctuates a lot. P increases with increasing $\Delta\varphi$ for the cooperating flagella pair. Near $tf_2 \approx 416$ or $\Delta\varphi \approx 0.83\pi$, it suddenly jumps to a plateau at the value double of single flagellum energy consumption $P_{single}=(2.3\pm0.2)\times10^3$, which refers to the separation of the cooperating pair. And there is a sudden drop afterwards due to the reformation of the flagella pair. By the cooperation, about 10% of energy is saved for a flagella pair in a MPC fluid.

In 2D, a string of finite length corresponds to an infinitely large sheet in 3D. Two undulating strings in a low Reynolds number fluid can adjust the irrelative positions to synchronize the phase of the beat through HI. The phase-locking arises from

hydrodynamics forces along [96]. Taylor [16] predicted this synchronization effect for sinusoidal undulating strings. In Taylor's calculation, the strings are infinite and their beating motion is prescribed by shape functions. The force density encountered on two strings through hydrodynamics is calculated as a function of the phase difference between the strings. Taylor found that, the force dipole on the strings always push them to the direction of phase locking. Also, the energy dissipated on the strings is less when the phase difference is smaller. The hydrodynamic synchronization effects between sinusoidal beating flagella, predicted by Taylor [16], was validated by several experimental [32][63] and simulation studies [15][31][63]. Another result of HI between two undulating strings is an effective attraction. The synchronized strings will gradually get closer and stay together for a long time if they have no beat frequency difference [63].

In our simulation, different from Taylor's calculation, we use a flagellum model of finite length instead of an infinite one, with only one full sine wave. Furthermore, the motion is generated by a defined spontaneous curvature instead of a prescribed shape. Thus, the shape of the flagellum can respond to the viscous environment and noises. The short flagella with only one complete sine wave - different from the infinitely long strings considered by Taylor - show strong cooperative behavior in 2D. The synchronization and attraction effects come purely from HI between undulating motions of flagella when they are separate. If two flagella are touching, the strong volume exclusion (VE) effect in 2D also strengthens the synchronization effect.

4.3 Swarm behavior of multi-flagellum systems

There are several factors influencing the swarm behavior of a multi-flagellum system, such as HI, VE, the sinusoidal beat and the distribution of beat frequencies.

HI is very important for the cooperation of flagella, as shown in the two-flagellum simulations. The attraction and synchronization effects of sinusoidal beating flagella pull the nearby flagella closer and attune the relative positions to lock in phase. At the same time, a flagellum feels HI from all other flagella distributed in space, which it is not cooperating with. Thus, the flagellum is exposed to a strong environmental noise generated by others. This noise reduces the flagellar cooperation. Thus it is hard to say whether the hydrodynamic interaction favor or disfavor the cooperation and clustering behavior in a multi-flagellum system.

On the other hand, in 2D, VE plays a very important role for rSPP, as we discussed in Chapter III. VE has a strong effect on alignment of rSPP in a viscous environment such as a low-Reynolds-number fluid. This alignment is crucial to the emergence of the swarm behavior [24][25].

In systems of sinusoidal undulating flagella, the effect of VE on alignment should

be similar as for rSPP. When two flagella swimming in different direction meet, they are aligned parallel or anti-parallel, instead of bouncing back as in elastic collisions. Although VE is crucial for swarming system of rSPP, the influence of the sinusoidal beat has to be investigated. Also, the distribution of frequencies as an internal diversity of rSPP properties, affects the swarm behavior of flagella. In the multi-flagellum simulations, we hope to understand the influence of those factors, especially the contribution of hydrodynamic interactions.

In our simulation, N flagella are put into the simulation box with random initial positions and orientations, without any overlap. If not explicitly mentioned, the side length of a simulation box is $L_x=L_y=200a$, which is eight times of the contour length of a flagellum. The number density of flagella is $\rho_f=N/(L_x\times L_y)$. The configuration of flagella is straight before they start beating. At $t=0$, each flagellum starts to swim with a random initial phase and a frequency selected from a Gaussian distribution. The Gaussian distribution of the frequencies has an average $f_0=1/120$ and a rescaled variance $\sigma_f= <(f-f_0)^2>^{1/2}/f_0$. The frequency of a flagellum remains constant during the simulation. Each system runs for the simulation time $t>4\times10^5$, corresponding to more than 3000 beats.

In a multi-flagellum system, large clusters are formed by the combination of small ones. At the same time large clusters break up into small ones due to the environmental noise or the diversity of the flagella frequencies. As discussed in Section 3.1 above for rod-like self-propelled particles, the system reaches a dynamically stationary state when the forming rate balances the break-up rate.

4.3.1   Configuration of clusters

A multi-flagellum system in 2D has VE as alignment mechanism and hydrodynamic interactions as attraction between the motile agents. It shows the swarm behaviors as SPP systems, with alignment in the moving direction. In both MPC and AF simulations, we see aggregation and clustering (Fig. 4.5) for not too large σ_f values. In addition, flagella strongly fluctuate due to environmental noise in a MPC fluid. Thermal fluctuations are not important for flagella motion although it is naturally included in MPC method. The environmental noise for a flagellum mainly arises from HI with all other flagella in the system. Flagella with AF have smooth trajectories due to the absence of noise.

The difference in the configurations of large clusters in MPC fluid and with AF is remarkable. In MPC simulations, a large cluster is usually strongly extended in its moving direction. The flagella inside the cluster are well synchronized, as shown in Fig. 4.5a. This structure is reminiscent of the "sperm-train" structure observed in the rodent sperm experiments. As explained in Section 1.2, rodent sperm which are
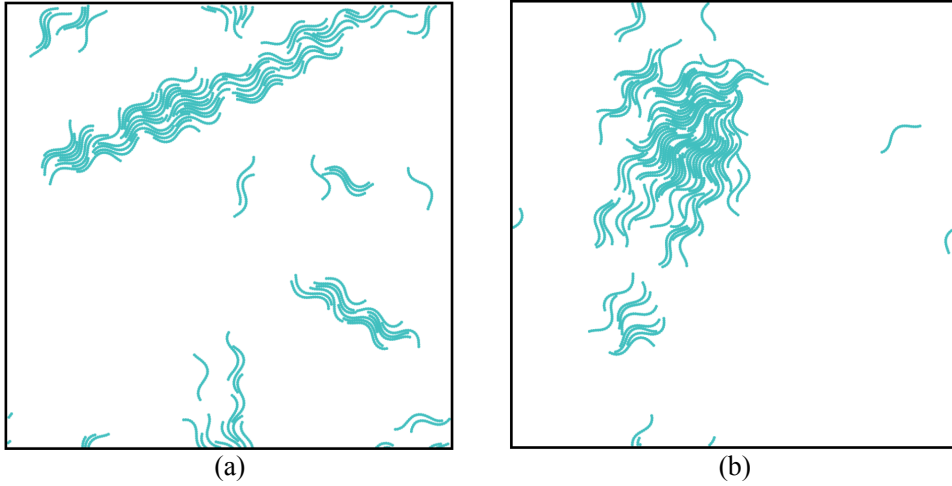
Figure 4.5: The snapshots of the multi-flagellum system (a) in a MPC fluid and (b) with AF. The parameters are $\rho_f L_f^2$=1.5625, σ_f=0.1%. The black box denotes the boundary of the simulation box. The periodic boundary condition is employed.

initially in a single suspension, aggregate and form huge clusters with strongly elongated shape [23]. In AF simulations (shown in Fig. 4.5b), flagella in a large cluster are synchronized only due to VE, but not as well polarized as in MPC fluids. The configurations of large clusters in this case are more similar to the motile clusters of rSPP (Fig. 3.2), and extend slightly in the direction of motion.

In order to compare the cluster structure, we define a correlation function of

Figure 4.6: The orientational correlation function of flagella as a function of the relative position of two flagella in polar coordinates (a) in MPC fluid and (b) with AF with $\rho_f L_f^2$=1.5625 and σ_f=0.1%; (c) in MPC fluid and (d) with AF with $\rho_f L_f^2$=1.5625 and σ_f=3%.

Figure 4.7: The orientational correlation function G in the parallel and perpendicular directions with $\rho_f L_f^2 = 1.5625$ and $\sigma_f = 0.1\%$. G in all directions of same systems are shown in Fig. 4.6ab.

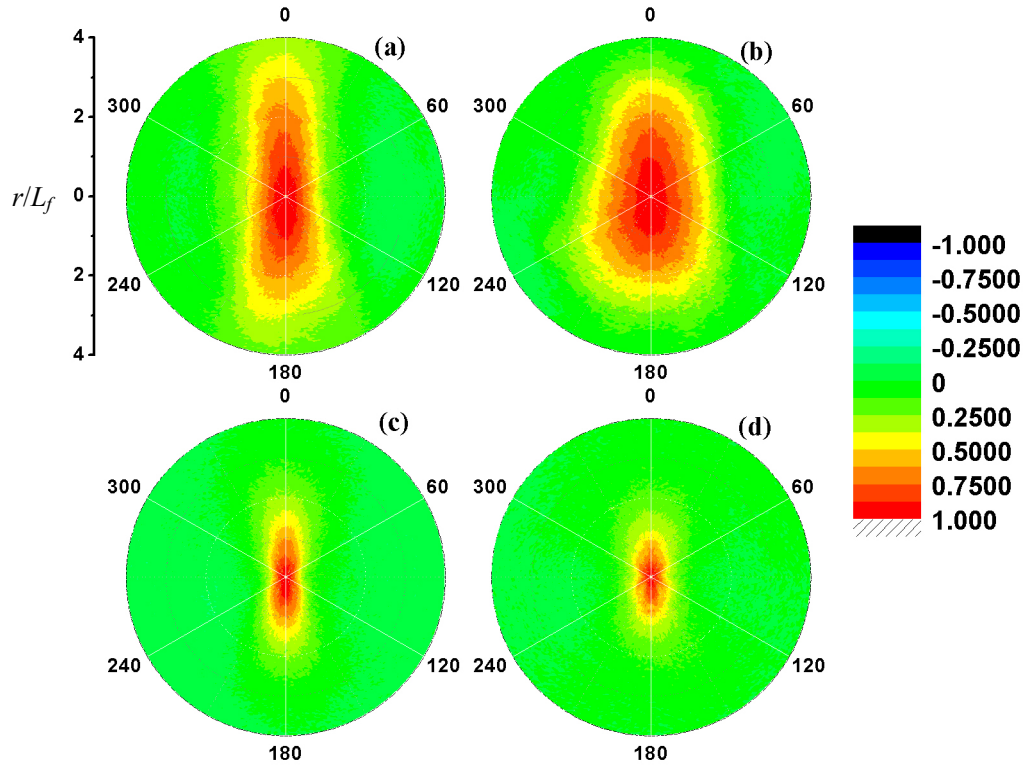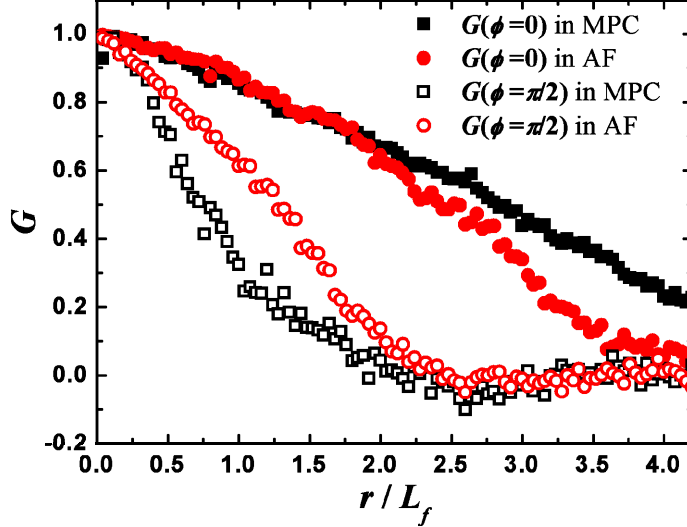flagella orientation, the same as that for rods in Section 3.2,

$$G(\mathbf{r}) = <\hat{\mathbf{u}}_i \cdot \hat{\mathbf{u}}_j \cdot \delta(\mathbf{r} - \mathbf{r}_{ij}) >.$$

The unit vector $\hat{\mathbf{u}}_i$ pointing from the end to the front of the i-th flagellum represent the flagellar orientation. The vector $\mathbf{r}_{ij}$ points from center-of-mass of flagellum i to flagellum j in a polar coordinate system where $\hat{\mathbf{u}}_i$ is the direction of $\phi = 0°$ (Fig. 3.6). Thus $G(\mathbf{r})$ is the orientational correlation of another flagellum at the relative position $\mathbf{r}$.

Fig. 4.6 shows the correlation function G for different systems. The flagella in the same cluster are polarized (Fig. 4.5), whereas the orientation correlation between different clusters is weak. Thus, $G(\mathbf{r})$ vanishes for large $\mathbf{r}$. $G(0)=1$ because a flagellum is trivially correlated with itself. Near $\mathbf{r}=0$, $G(\mathbf{r})$ is positive since the neighbor flagella have to attune their orientation due to VE. The correlated region is larger for small σ_f (Fig. 4.6ab) than for large σ_f (Fig. 4.6cd) in both MPC and AF simulations, which shows the stronger aggregation in systems with smaller σ_f. When the correlated region extends to $r>100$, the correlation function is strongly affected by the periodic boundary conditions in our simulations.

The difference in the correlation functions demonstrates the large difference of the cluster configurations in MPC and AF simulations. The correlations with AF, similar as Fig. 3.7a, show a larger range in the parallel directions than in the perpendicular directions due to the rod-like structure of the flagellum. Compared with AF simulations, G in MPC simulations extends more in the parallel directions ($\phi=0°$ and $\phi=180°$) and shrinks in the perpendicular directions ($\phi=90°$ and $\phi=270°$). In MPC fluid, a clear reduction of G is found in the perpendicular direction even for large σ_f. The reduction is due to the hydrodynamic attraction. The synchronization

elongates the clusters, thus G extends strongly in the parallel direction.

G in parallel and perpendicular directions are shown in Fig. 4.7. With same σ_f and ρ_f, G in the parallel directions decreases slower in MPC fluid than with AF, while in the perpendicular directions G in MPC fluid decreases faster. This indicates a larger aspect ratio of clusters in MPC fluid than in AF simulations.

4.3.2   Probability density function (PDF) of cluster size

We define a cluster as follows. If the angle between unit vectors of flagellar orientations $\hat{\mathbf{u}}_i$ and $\hat{\mathbf{u}}_j$ is smaller than $\pi/6$, and at the same time the nearest distance between two flagella is smaller than $4a$, which is on the scale of the amplitude of the flagellar beat, we consider these two flagella neighbor to each other and in the same cluster. A cluster is defined as a set of flagella that are connected or neighbor either directly or through other agent at a given moment in time. Its size is the number of flagella it contains.

Figures 4.8 and 4.9 show examples of different types of PDF in MPC and AF simulations. Each PDF has a power-law-decay part for small n. Such a power-law distribution agrees with Huepe et al's results [55][56] of the swarm behavior simulation of point SPP and with our results for rSPP presented in Chapter III. In the rSPP simulations, PDFs are sorted into three types. PDF1 (Fig. 4.8) has a power-law part for small n and approaches to exponential or Poisson distribution for large cluster size. In PDF2 (Fig. 4.9), there is a peak at high n corresponding to the large, motile clusters.

The exponent β of the power-law part of PDF is a function of a set of system parameters such as the flagellum density, the flagellar length and the frequency distribution, etc. We only investigate the influence of the flagellum density ρ_f and the
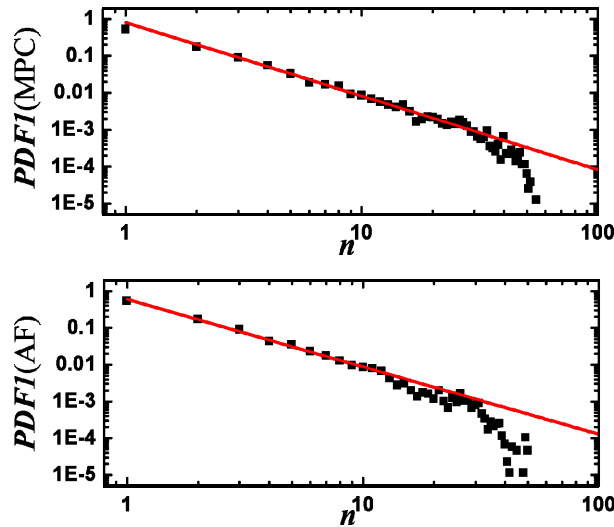

Figure 4.8: The first type of probability density functions (PDF1) of cluster size n for MPC (top) and AF (bottom) simulations. The flagella number density is $\rho_f L_f^2 = 1.5625$ and $\sigma_f = 2\%$.
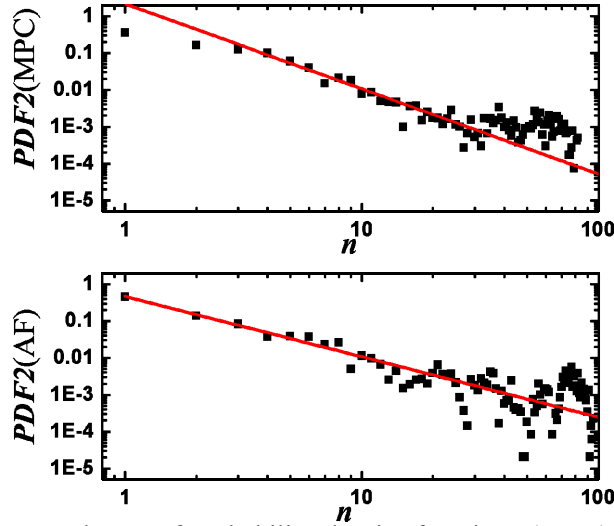
Figure 4.9: The second type of probability density functions (PDFs) of cluster size n for MPC (top) and AF (bottom) simulations. The flagella number density is $\rho_f L_f^2$=1.5625 and σ_f=0.1%.

variance of the frequency distribution σ_f here.

Fig. 4.10 shows β as a function of the flagellum density in MPC fluid. β increases with increasing density ρ_f, which corresponds to a higher probability to find larger clusters at higher density. Fig. 4.11 shows β as a function of the frequency variance σ_f. Although the distribution of beating frequencies is an internal property of the swimmers, the influence of σ_f on β is similar to the external noise of self-propelled rods (as discussed in Section 3.1). β is nearly constant for σ_f<3%, then decreases smoothly with an increasing σ_f. The relation of β and ρ_f is very similar as for rods (Section 3.1).

In our flagellum simulations, we found PDF1 and PDF2 in both MPC and AF simulations, but no PDF3 with giant clusters as rSPP system. The number of flagella

Figure 4.10: The exponent β of cluster size distribution function is plot as a function of flagella density in the system in MPC fluid. The simulation box size is $200a \times 200a$, and the frequency deviation σ_f = 3%.

Figure 4.11: The exponent β of cluster size distribution function is plot as a function of the variance of frequency distribution. The simulation box size is $200a \times 200a$, and the flagellum density $\rho_f L_f^2 = 1.5625$. Symbols represent the results in MPC fluid (■) and with AF (●).
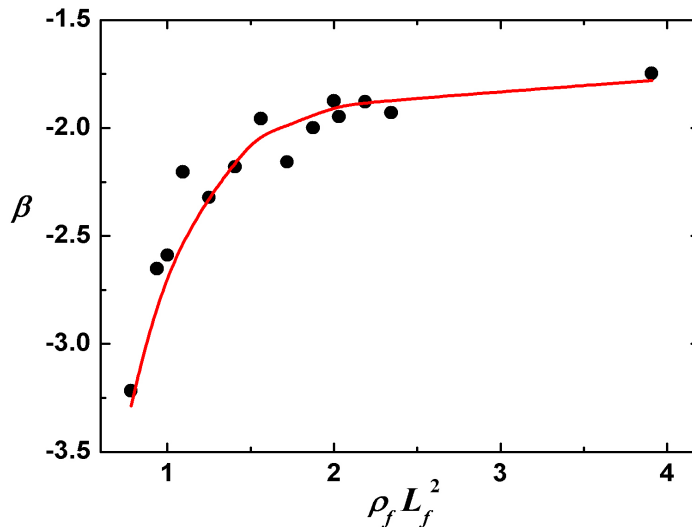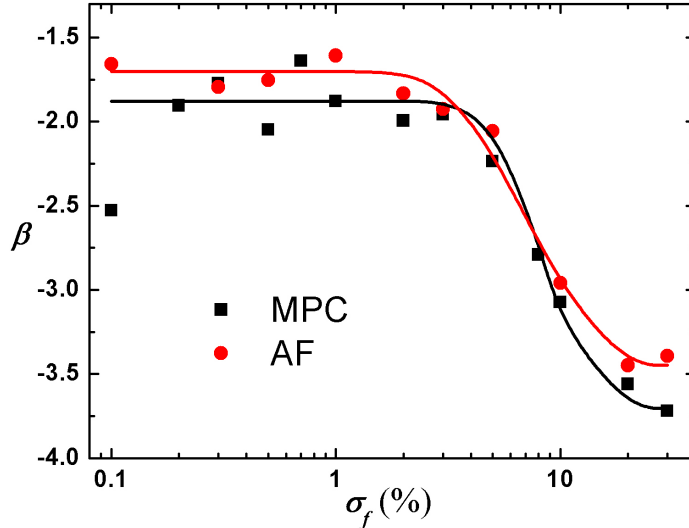
is not large enough in our simulation to form the blocked structure of a giant cluster. The similarity of PDFs of flagella clusters with those of rSPP indicates that the flagellar beat, and HI as environmental noise and synchronization / attraction effects do not destroy the fundamental swarm behavior. The crucial elements of swarm behavior are the self-propulsion and the mechanism of alignment, mainly induced by VE of the rod-like configuration.

PDFs are influenced by system parameters such as the flagellar length, density, the frequency distribution, etc. Decreasing the flagellar length and density, or increasing the width of the frequency distribution, decreases the probability to form a large cluster. At the same time, PDFs transit from type 2 to type 1, and then decrease the range of power-law decay until the flagella are randomly distributed.

The difference between PDFs of MPC and AF simulation is seen for small n. The power-law decay starts from $n=1$ in AF simulation, while it does not in MPC simulation, especially with small σ_f (see Fig. 4.9). The probability to find clusters of size $n=1$ and 2 in a MPC fluid is lower than expected from the power law for larger n. A possible explanation of this behavior is as follows. The large clusters in MPC simulation are more elongated (Fig. 4.5a) and can sometimes even extend to a distance as large as the side length of the simulation box. So the scattering cross section of these clusters is large. They create a strong flow field, and easily collect nearby small clusters. However, the extended configuration is also more likely to break up if there is a frequency distribution, and the larger clusters have lower swimming velocities in MPC fluid (as discussed in Section 4.3.4). Before an extended cluster can absorb another large but slowly moving cluster, it may already have broken up. Thus the large cluster mainly collects nearby small clusters.

4.3.3 Stationary average cluster size $\bar{n}$ and weight $\bar{w}$

As explained in Section 3.3 for rSPP, the stationary average cluster size and the stationary average cluster weight are defined as,

$$\bar{n} = \sum_t <n>/T =< \sum_n n\Pi(n,t) >_t$$

$$\bar{w} = \sum_t <w>/T =< \sum_n n^2 \Pi(n,t)/\sum_n n\Pi(n,t) >_t$$

where $< >_t$ is the average over time t. Due to the random initial conditions, the average cluster size $<n>$ and weight $<w>$ are about 1 at the beginning, and increase when the flagella start to beat and aggregate. Due to the finite simulation-box-size, $<n>$ and $<w>$ fluctuates with time when the stationary state is reached. The average value of $<n>$ and $<w>$, denoted by $\bar{n}$ and $\bar{w}$ respectively, approaches $<n>$ and $<w>$ in the infinite system if we increase the simulation box size.

$\bar{n}$ and $\bar{w}$ change with σ_f and ρ_f, as shown in Fig. 4.12 and Fig. 4.13. Decreasing σ_f, the break-up rate of clusters is decreased; hence the chance to find the large clusters, and the average cluster size, increase. At large σ_f, $\bar{n}$ and $\bar{w}$ approach 1, corresponding to a disordered state of the randomly distributed flagella. However, in both cases, the remarkable power-law decay emphasizes the fundamental property of the swarm behavior of rSPPs (Section 3.3). The power law of $\bar{n}$ implies a divergence for $\sigma_f \to 0$, which is valid for the AF simulation without any system noise. In the low density limit, when ρ_f approaches 0, $\bar{n}$ and $\bar{w}$ approaches 1. With increasing ρ_f, $\bar{n}$ and $\bar{w}$ also increase as a power law function of ρ_f, as indicated by the fit lines. The absolute values of $\bar{n}$ and $\bar{w}$ in MPC and AF simulations are not easily comparable, e.g. due to the different cluster velocity profiles and the
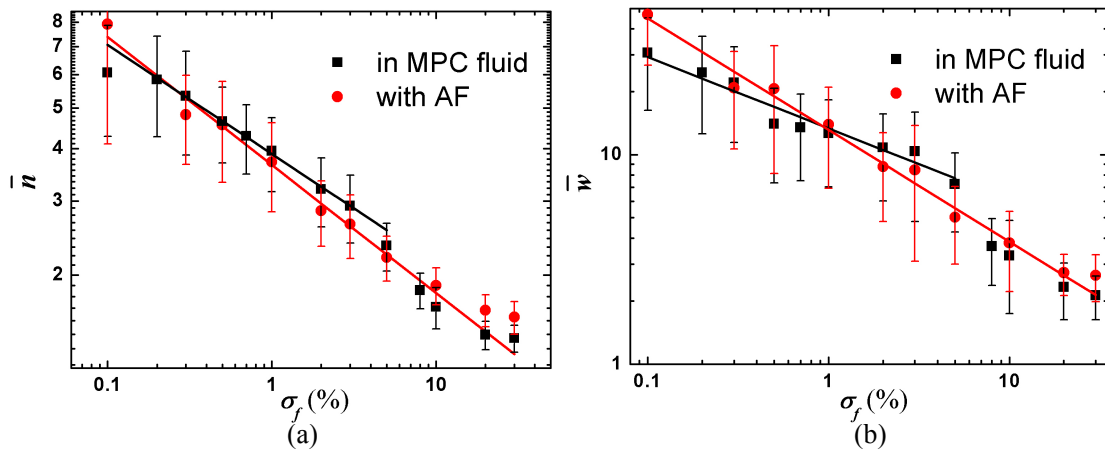

Figure 4.12: The stationary average cluster size $\bar{n}$ and the stationary average cluster weight $\bar{w}$ as a function of the variance of frequency distribution σ_f with $\rho_f L_f^2 = 1.5625$. Symbols represent the result in MPC fluid (■) and with AF (●). The error bars represent the standard deviation of the fluctuations with time. The fit lines indicate the power-law decay.
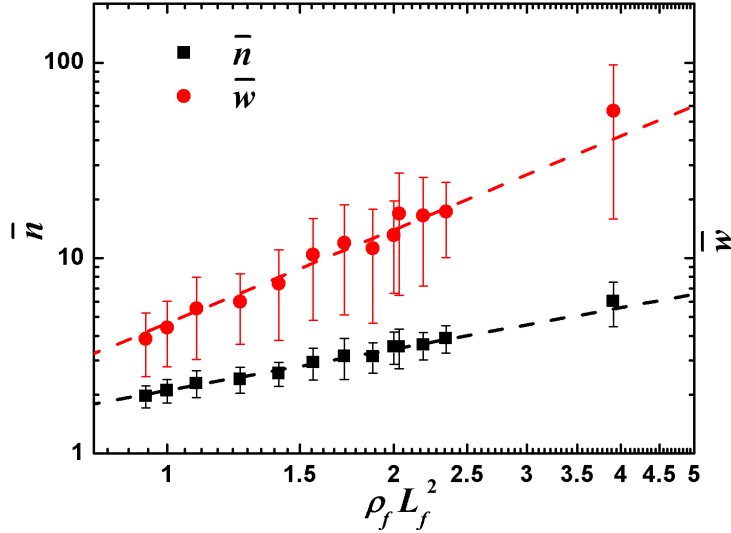
Figure 4.13: The stationary average cluster size $\overline{n}$ and the stationary average cluster weight $\overline{w}$ as functions of flagella density $\rho_f L_f^2$. The variance of the frequency distribution is σ_f=3%.

environmental noise.

The power-law decay of $\overline{n}$ with σ_f in MPC simulation is different from that in AF simulation. The exponent of the power law is a single value in AF simulations, while there seem to be two regimes in MPC simulation. The transition occurs at σ_f=3%. It can be understood in this way. As discussed in Section 4.3.2, due to the extended configuration of the large clusters, the PDF for MPC simulation has a deviation from the power-law decay at small cluster size. HI of flagella elongates the cluster configuration and decreases the probability density of small clusters, thus increases <n>. With increasing σ_f, the break-up rate of clusters increases, and the probability to find large clusters decreases. The effect of elongation fades quickly with the cluster size, thus the PDF deviation from a power law at small n gradually
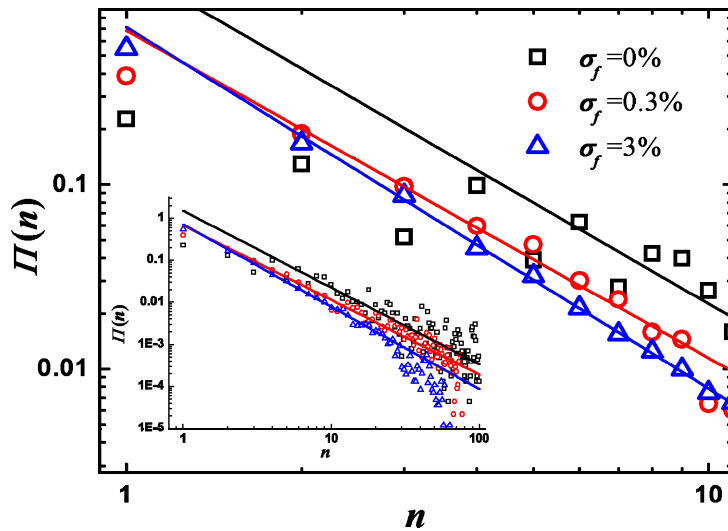
Figure 4.14: Cluster size distribution $\Pi(n)$ for various variances σ_f of the frequency distribution. The lines fit the power-law part of each PDF of systems with same flagellum density $\rho_f L_f^2$=1.5625, as indicated in the inset.

disappears with increasing σ_f, as shown in Fig. 4.14. On the other hand, if the phase difference between flagella is large, the hydrodynamic synchronization effect will draw them apart. Even though a cluster may form by chance, it will break down soon after due to the large difference in beat frequencies of its members. The increasing number of clusters in the system causes an increasing environmental noise which also increases the break-up rate. This effect is strong when σ_f is really large. It makes the system with MPC approach the disordered state faster than AF simulations, and it leads to a lower $\bar{n}$ near 1.

Thus, in MPC simulation with different σ_f, $\bar{n}$ is determined by the competing mechanisms. For small σ_f, HI elongates cluster configurations and decreases the number of small clusters, while for large σ_f it plays the role of a system noise and an internal mechanism to break up the clusters. In Fig. 4.12, σ_f=3% is the transition point of the competition of these two mechanisms. In AF simulations, there is neither hydrodynamics nor other system noise. So we see only one power-law decay of $\bar{n}$.

4.3.4 Cluster velocity

We start to analyze the velocity of a cluster of size n when it is formed, and stop data collection when the cluster breaks down or collides and forms a cluster of different size or with different members. Fig. 4.15 shows the displacement Δs of the center-of-mass of the clusters per beat. Due to the power-law decay of PDF, the data for the small clusters has more samples with a lot of different configurations than the large clusters. Although we choose the parameters to make the same forward velocities of a single flagellum in MPC fluid and with AF, the cluster velocities are very different. In MPC fluid, despite the weak effect of environmental noise on large clusters, Δs decreases with cluster size n. With AF, the cluster velocity is nearly a constant.

The scatters of the data in MPC simulations for large cluster sizes indicate not only the small number of samples, but also a wide distribution of velocities. The velocity of large cluster depends on several factors such as the cluster configuration, the frequency distribution and the noise. Although the scatter is large, the reduction of Δs for large n is still clear.

The decrease of Δs with cluster size n in a MPC fluid has several reasons. First, $\Delta s(1)$ in a multi-flagellum simulation is higher than in a single-flagellum simulation, because HI with other clusters generates an environmental noise which strongly affects the small clusters. The influence of the environmental noise decreases with n due to the increasing size. Second, a large "train" cluster in MPC fluid can be considered as a huge "flagellum". The flagella are synchronized and tightly packed due to the hydrodynamic synchronization and attraction effects. Such a huge
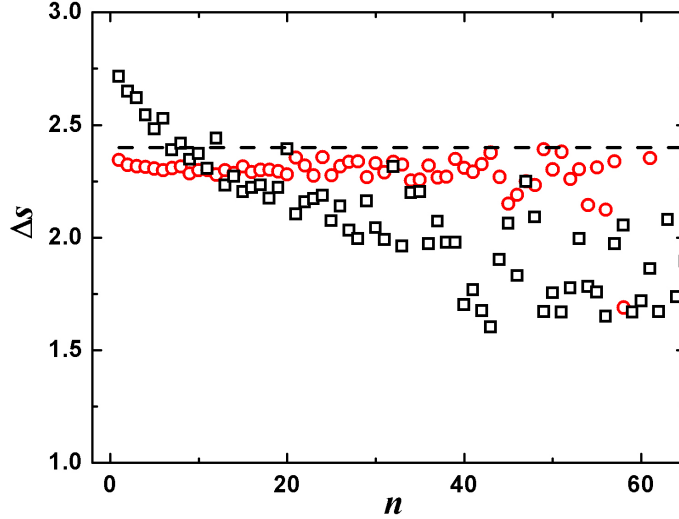
Figure 4.15: The average center-of-mass displacement Δs of the clusters per beat as a function of cluster size n in MPC fluid ($\square$) and with AF ($\bigcirc$). The variance of frequency distribution σ_f=3%. The dash line indicates the displacement per beat of a single flagellum of the average beat frequency in the single-flagellum simulation.

"flagellum" has same frequency and wave length, but the propelling force is mainly contributed by the flagella at the cluster boundary. Thus the smaller propelling force and the larger body produce a lower velocity than for a single flagellum.

Δs with AF is much smoother than that in a MPC fluid. For large n, although the number of samples in our simulation is on the same scale of that in MPC fluid, Δs stays near the plateau of single flagellum value with only a little scatter. In AF simulations, the propelling forces do not change when the flagella form clusters, and the hydrodynamic interaction between flagella is absent. Also, there is no environmental noise. The velocity difference of flagella is averaged out for large clusters. Therefore, Δs approaches the value of a single flagellum of the average frequency. Our rSPP simulations in Section 3.5 have shown that the cluster velocity decreases for large clusters due to a blocking of the motion of individual particles. However, in our flagellum simulations, the cluster size is not large enough yet to show this effect.

Our results of flagella motion in MPC fluid are consistent with mouse-sperm cluster experiments [22]. The cooperative behavior of mouse sperm does not always increase the swimming speed. In most of the cases, a single sperm has higher speed in the fluid medium then cooperating sperm pairs or clusters.

4.3.5   Cluster life time

We define the life time of a cluster in the same way as we did for the rod simulations, see Section 3.6.

Fig. 4.16 shows the average cluster life time T_{life} as a function of cluster size n. Note that the system size is not as large as for the rod simulations. The total number
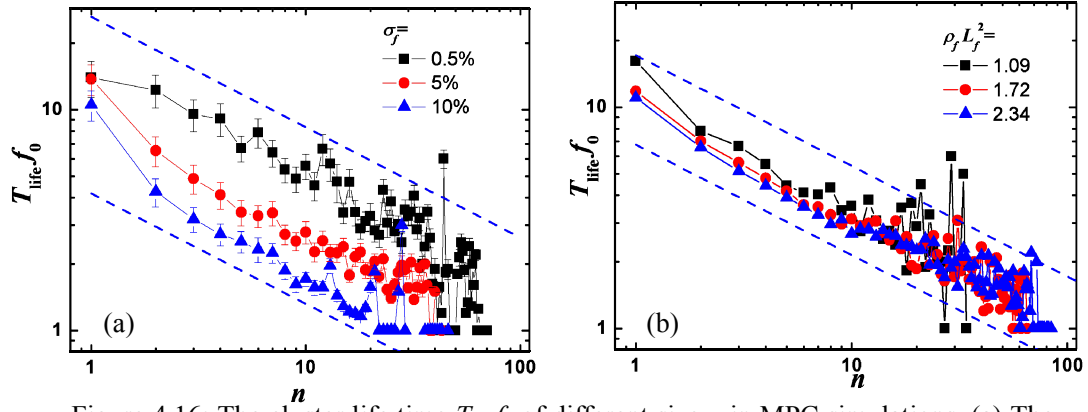
Figure 4.16: The cluster life time $T_{life}f_0$ of different size n in MPC simulations. (a) The systems with same flagella density $\rho_f L_f^2 = 1.5625$. (b) The systems with the same variance of frequency distribution $\sigma_f = 3\%$. The blue dash lines in (a) and (b) are power-law functions with the exponent of -0.4.

of flagella is only from 50 to 250. Thus, for most simulations, we do not have as good statistics for large clusters. The average life time decreases with the cluster size. In the rod simulations, the cluster of size 1 always has a longer life time due to the lack of break-up. However, in MPC fluid, due to the hydrodynamic interaction, $T_{life}(1)$ does not always have the largest value (e.g. $\sigma_f = 0.5\%$ in Fig. 4.16a). We set aside $T_{life}(1)$ and the scattered data for large n, and only consider the range where the data are consistent with a power-law relation (as in the case for rSPP). Fig. 4.17 shows the exponent β_{life} of this tentative power law of $T_{life}(n)$. The values of β_{life} are scattered around -0.55 and does not strongly depend on ρ_f and σ_f, as in the rod simulations.

T_{life} is a function not only of cluster size n, but also of the flagella density ρ_f and the variance of frequency distribution σ_f. The greater σ_f is, the shorter is the time needed to generate a large enough phase difference to break down the cluster.

Fig. 4.18 shows $T_{life}(n)$ for $1 \leq n \leq 5$ as a function of the flagellum density ρ_f. The
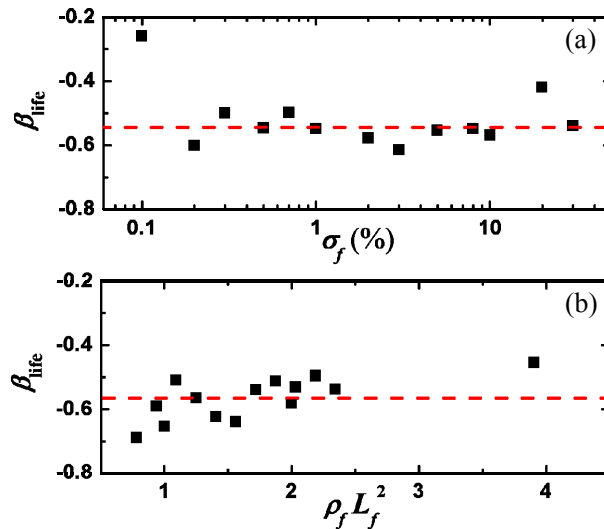

Figure 4.17: The exponent β_{life} of the cluster life time function $T_{life}(n)$ for small cluster sizez n. β_{life} is nearly independent of (a) the variance of frequency distribution σ_f, and (b) the flagellum density $\rho_f L_f^2$. The dash lines indicate the average value of β_{life}.
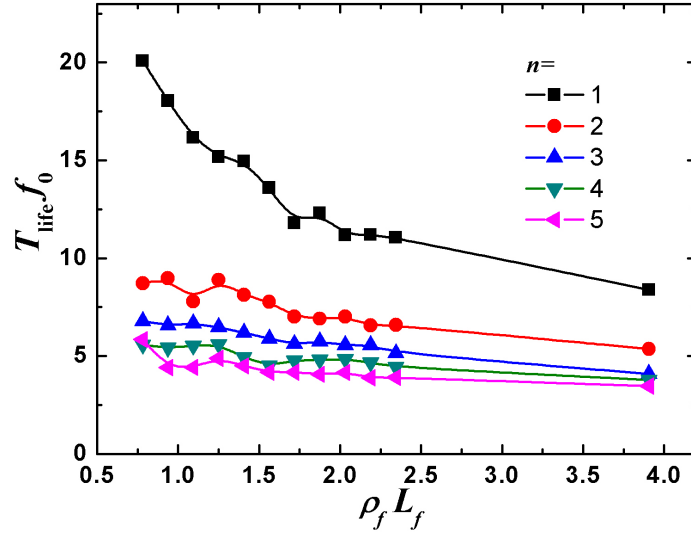
Figure 4.18: $T_{\text{life}}f_0$ for $1 \leq n \leq 5$ as functions of the flagellum density $\rho_f L_f^2$ in MPC simulations.

life time $T_{\text{life}}(n)$ for $2 \leq n \leq 5$ decreases slightly with ρ_f. As an exception, the life time of the single flagellum changes a lot with density (the same as Fig. 3.18b for rSPP).

Fig. 4.19 shows $T_{\text{life}}(n)$ for $1 \leq n \leq 5$ as a function of the variance σ_f of the frequency distribution. Data for both MPC simulations and AF simulations are shown. In rod simulations, the life time of clusters of size n decreases with the environmental noise (see Fig. 3.18a). In our flagellum simulations, σ_f can be regarded as the internal "noise" of the flagella. The decay of T_{life} in AF simulation (Fig. 4.19b) is purely due to this noise. In a cluster of n flagella with different frequencies, the phase difference between neighbor flagella increases with time. Due to the synchronization effect and volume exclusion, the cluster breaks at the place where the phase difference is too large to keep the flagellar cooperation. Similar as the self-propelled-rod systems, T_{life} for different n decreases roughly as a power-law of σ_f in AF simulations.

The most profound difference between Fig. 4.19a and 4.19b is the curves for $T_{\text{life}}(1)$. $T_{\text{life}}(1)$ decreases with the same exponent as other curves in AF simulation, while in MPC simulations it clearly decreases much slower for $\sigma_f < 3\%$. $T_{\text{life}}(1)$ is
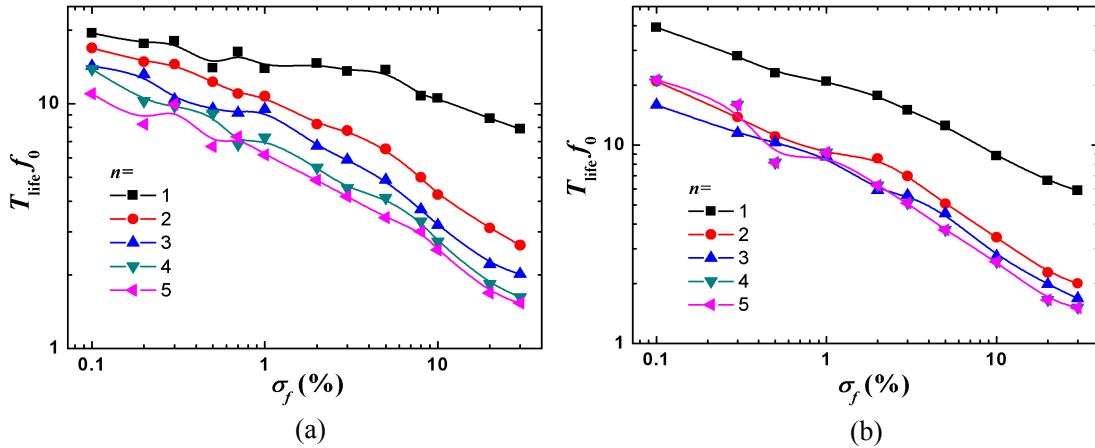

(a)	(b)

Figure 4.19: $T_{\text{life}}f_0$ for $1 \leq n \leq 5$ as functions of the variance of frequency σ_f (a) in MPC fluid and (b) with AF. The flagella density is $\rho_f L_f^2 = 1.5625$.

inverse to the collision rate of a single flagellum with other cluster and flagella. The slower decrease of $T_{life}(1)$ can be the result of two aspects, a decreasing collision cross section or a weaker attraction between swimmers. In MPC simulations, the large clusters have extended structures as discussed in Section 4.3.1. Their collision cross section is much larger than in AF simulations. With increasing σ_f, the collision cross section decreases with decreasing average cluster size. In addition, a large cluster with the extended structure creates a strong flow field to attract the nearby small clusters. A single flagellum can be easily caught by the flow field of a very large cluster. Due to these two reasons, $T_{life}(1)$ decreases slower for small σ_f in MPC simulations. For large σ_f, HI acts more like an environmental noise and the synchronization effect break up the clusters quickly. The extended large clusters have too low probability to form. Thus the decrease of $T_{life}(1)$ becomes faster.

4.3.6 Finite-size effects

As mentioned in Section 3.7 for the rod simulations, the finite system size affects the results. Thus, we investigate now the dependence on the simulation box size with fixed flagella density and variance of the frequency distribution. We choose two densities ($\rho_f L_f^2=1$ and $\rho_f L_f^2=2$) and two frequency deviations ($\sigma_f=3\%$ and $\sigma_f=10\%$). The total flagella number is proportional to the square of the side length. Note that, because of the small flagella number, the frequency distributions for the small systems deviate from the Gaussian distribution. For small systems with less than 20 flagella, the deviations from our anticipated frequency distribution are larger than 5%.

Fig. 4.20 and Fig. 4.21 show the PDF of cluster size with different size of the simulation boxes. As explained in Section 3.1, PDF1 has a power-law part for small n and an exponential part for large n. When the simulation box is not large enough, PDF only shows part of the power law region, and decreases near the total number of the
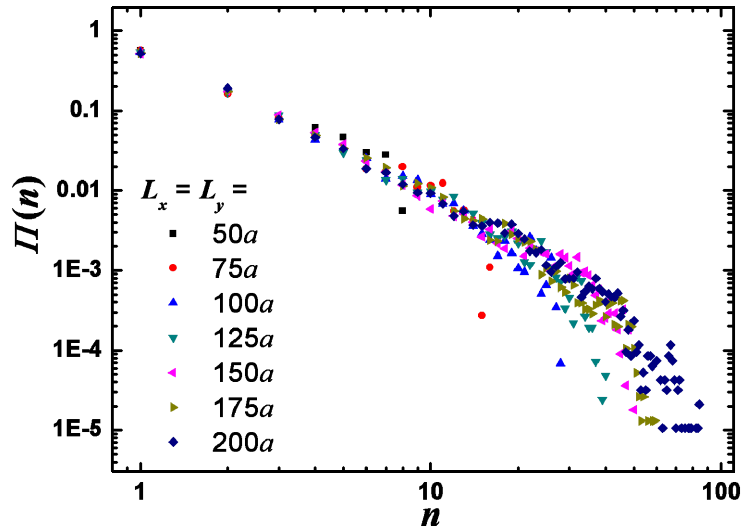
Figure 4.20: The distribution function of system with $\rho_f L_f^2=2$ and same $\sigma_f = 3\%$ and different simulation box sizes, as indicated.
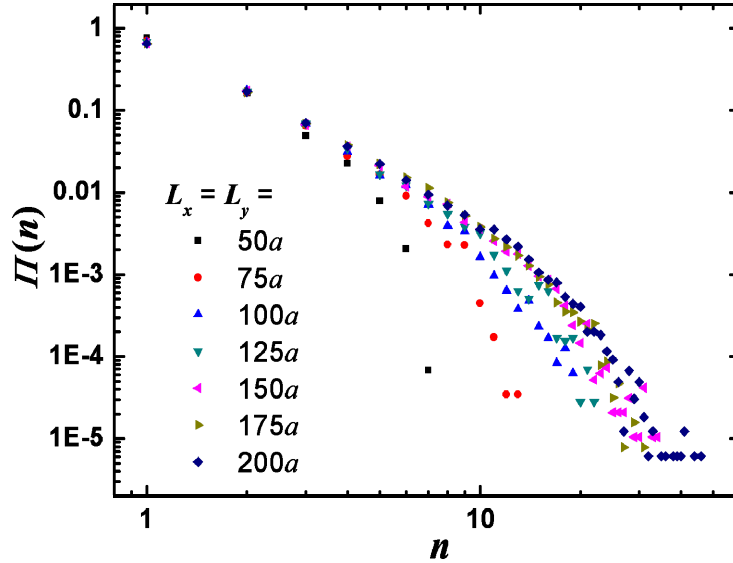
Figure 4.21: The distribution function of system with $\rho_f=2$ and same $\sigma_f = 10\%$ and different simulation box sizes, as indicated.

agents. The exponential part only exists when the system is large enough. In Fig. 4.20 with smaller σ_f, although all systems have PDF1, none of the simulation boxes is large enough. The power-law region continues to increase with increasing system size. In Fig. 4.21 with larger σ_f for the side length larger than $150a$, the system is large enough that the power-law region is fully developed and exponential region emerges.

The value of the exponent β scatters a lot when we change the system size, as shown in Fig. 4.22. The strong deviation from a Gaussian distribution induces large error to the exponent β. As known from rod simulations, β of PDF1 approaches to a finite and non-zero value with increasing the system size.

The stationary average cluster size $\overline{n}$ and the stationary average cluster weight $\overline{w}$ are also influenced by the system box size as shown in Fig. 4.23. In most of
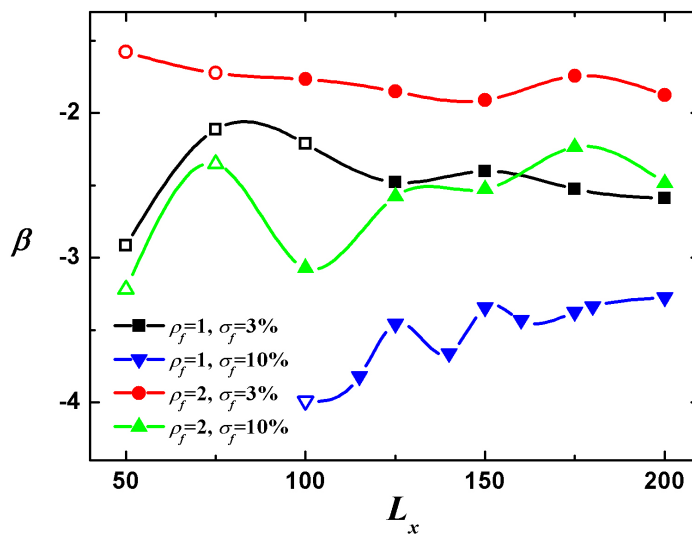
Figure 4.22: The exponent β of PDF as a function of the side length L_x of the simulation box. The open symbols denote the systems with a total flagellum number less than 20.
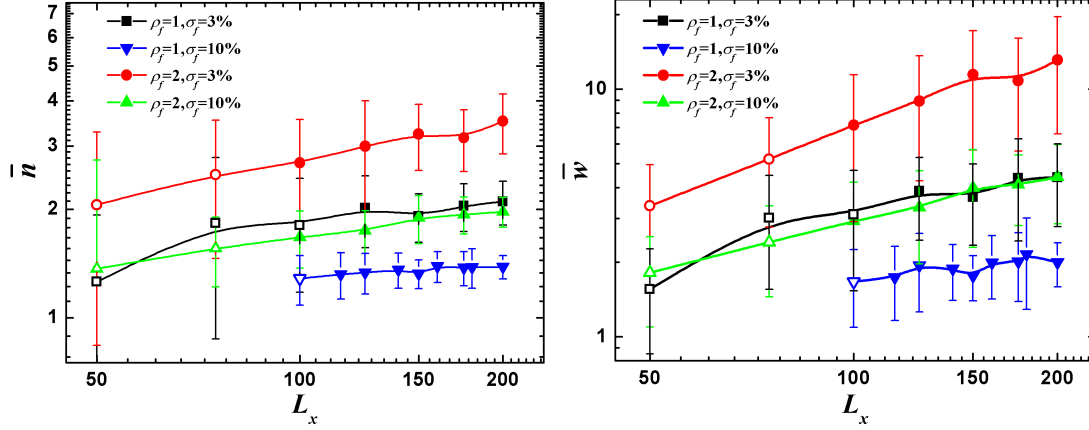
Figure 4.23: The stationary average cluster size $\overline{n}$ and the stationary average cluster weight $\overline{w}$ as functions of the side length L_x of the simulation box. The empty symbols denote the systems with a total flagellum number less than 20.

observed systems, $\overline{n}$ and $\overline{w}$ are not converged yet. Only for the system of $\rho_f L_f^2 = 1$ and $\sigma_f = 10\%$, $\overline{n}$ has reached the limiting bulk value. $\overline{w}$ depends more on the density of large clusters, and has not yet convergent for all system. The corresponding dependence of $\overline{n}$ and $\overline{w}$ of rSPP on system size is discussed in Section 3.7.2.

The analysis of the finite-size effects shows that the results have to be interpreted carefully. Most of the simulation systems have a flagellum density $\rho_f L_f^2 = 1.5625$ and the variance of frequency distribution σ_f ranging from 0.1% to 30%. Some systems (usually those with small σ_f) are not large enough to avoid finite-size effects. Systems of PDF1 with small σ_f or large ρ_f have not shown the full power-law region yet. Systems of PDF2 have even stronger dependence on the simulation box size as discussed in Section 3.7 for rSPP. Thus, statistical quantities, such as $\overline{n}$ and $\overline{w}$, deviate from their values for infinitely large systems.

However, according to our analysis of rSPP systems, some statistical properties are still reliable. The type of PDF does not change. A system with PDF2 will not have PDF1 by decreasing the system size. Also, in order to distinguish the contribution of HI on the swarm behavior by comparing MPC and AF simulations, the influence of simulation box size is not important if the same box size is used for all simulations.

4.4 Curved-flagellum system

A curved flagellum means that the average spontaneous curvature along the whole configuration is not zero. In our coarse-grained model, a curved flagellum is modeled by a non-zero value for c_0 in Eq. 2.5. In order to mimic the tail shape of sea-urchin sperm, we choose the flagellum length to be $50a$, and wave number $q = 4\pi/50a$. Thus there are two complete sine waves on the flagellum. The average spontaneous curvature is chosen to be $c_0 = 0.04/a$. The diameter of the trajectory of a single flagellum is then $45a$ with AF, approximately the length of the flagellum.

A couple of flagella with straight initial configuration are put into the simulation
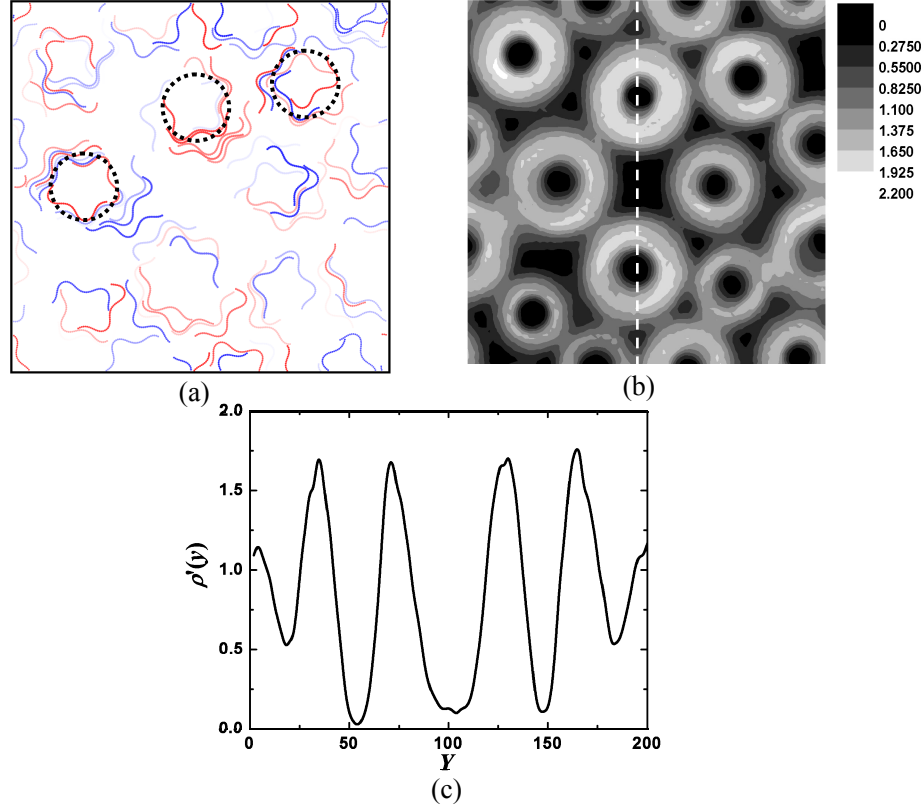
Figure 4.24: (a) A snapshots of the stationary state of curved-flagellum system with AF and $\rho_f L_f^2$=6.25, σ_f=0%. The simulation box size is L_x=L_y=200a. The circles of dotted lines indicate the curvature of some clusters. (b) The density function $\rho'(\mathbf{r})$ of system in (a) averaged over 1000 beats. (c) The density function ρ' on the dashed line in (b).

box with random initial positions and orientations. Once they start to beat, due to the positive c_0, they all tend to make a clockwise motion on circular trajectories. If the density is high, the flagella collide with each other and aggregate into clusters.

A snapshot of the stationary state in AF simulations in Fig. 4.24a shows that the curved structure avoids the formation of large clusters. The small clusters are localized due to the circular motion. In addition, the clusters have no random diffusion due to the absence of the environmental noise. After a short while, the system comes to a stationary state where the flagella form a number of localized vortices. A vortex may break up due to the collision with other vortices. Thus, there is mass transportation between vortices. The flagella in the same layer in a vortex are synchronized due to volume exclusion. However, flagella in different layers are usually not synchronized.

The density function $\rho'(\mathbf{r})=\rho(\mathbf{r})/\rho_f$ exhibits rings corresponding to the vortices, as shown in Fig. 4.24b. The flagella in the same vortex rotate together and push other vortices by VE. Considering a high density of the vortices, one can quickly imagine a hexagonal array. However, the flagellum density is not high enough to show a hexagonal array yet. The rings in Fig. 4.24b are randomly distributed as in a glassy

state.

The density correlation function $<\rho'(\mathbf{r})\ \rho'(\mathbf{r}+\Delta\mathbf{r})>-1$ of the AF simulation is shown in Fig. 4.25. The width of the first peak represents the thickness of the rings in Fig. 2.4b, which is approximately $15a$. The second peak is located at $\Delta r=32a$, corresponds to the average diameter of the vortices (the distance between the peaks of density in Fig. 4.24c). The diameter of the vortices is much smaller than the diameter of the circular trajectory of a single curved flagellum. The third peak at $\Delta r=61a$ corresponds to the average distance between the centers of the vortices. It is much larger than the size of vortices ($32a+15a=47a$). Thus volume exclusion between vortices is not strong enough to exhibit a hexagonal array of vortices. The vortices arrange themselves in a glassy state, so that the correlation function approaches 0 very fast.

The angular velocity ω of layers in a vortex is a function of the radius r of the layer. The velocity of flagella in the same layer, ωr, is drawn as the function of the radius in Fig. 4.26. The velocity for r smaller than radius of the vortex radius ($r<16a$) increases with an approximately linearly with r, thus the angular velocity ω is nearly a constant for r less than the radius of the vortices. The velocity for $r>16a$ approaches a plateau of single flagellum velocity. Thus, inside a vortex, the flagella in the inner layer ($r<16a$) tend to be synchronized due to VE. However, VE is not sufficient to maintain the synchronization. Thus there is still some difference in ω in the inner layer. The flagella in the outer layer ($r>16a$) have different ω and are not synchronized.

In MPC simulations, those vortices are not stable due to too strong HI in 2D. A snapshot of the system with the same parameters, but now in MPC fluid is shown in Fig. 4.27. For small σ_f, the cluster size is obviously larger than in AF simulations, and
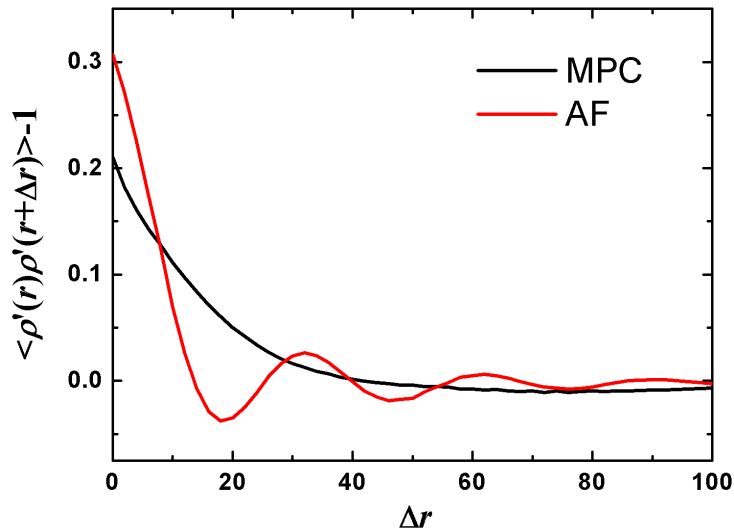
Figure 4.25: The density correlation function $<\rho'(\mathbf{r})\rho'(\mathbf{r}+\Delta\mathbf{r})>-1$ of the density function with $\rho_f L_f^2=6.25$ and $\sigma_f=0\%$.
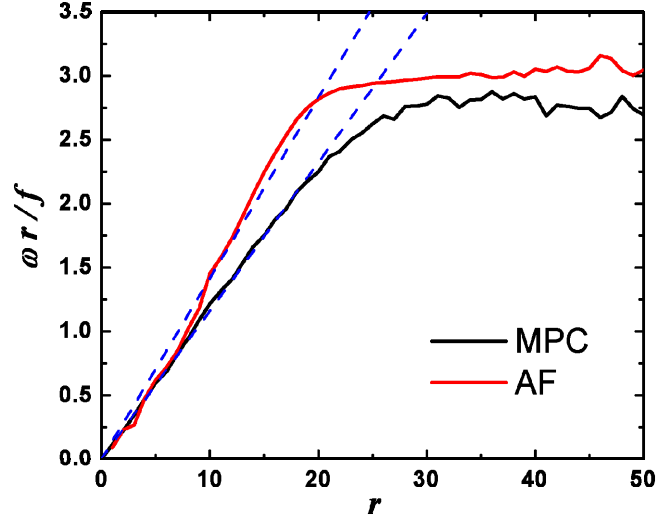
Figure 4.26: The rotating velocity $\omega r/f$ of vortices at different layers of radius r in the system with $\rho_f L_f^2$=6.25 and σ_f=0%. The blue dash lines are linear fitting of r<15.

the flagella are well synchronized. The better linear relation of $\omega r/f$ with r (see Fig. 4.26) indicates a better synchronization in MPC fluid. However, the curvature of the cluster structure strongly depends on cluster size and phase differences between flagella. The cluster curvature has a wide distribution. Also, HI as environmental noise is too strong and breaks the vortex structure, although it also helps to keep synchronized flagella together. The density correlation function $<\rho'(\mathbf{r})\,\rho'(\mathbf{r}+\Delta\mathbf{r})>-1$ of the same system shown in Fig. 4.27 approaches zero monotonically, without special structures.

The vortices in AF simulation are very similar to the phenomenon in experiments of sea-urchin sperm [32]. Riedel et al found experimentally that the vortices emerge when the density of sea-urchin sperm at the substrate reaches a critical value. The sea-urchin sperm swim in a quasi-2D environment, thus VE effect is enhanced. Our 2D simulation suggests that VE plays an important role, while HI in 3D might mainly
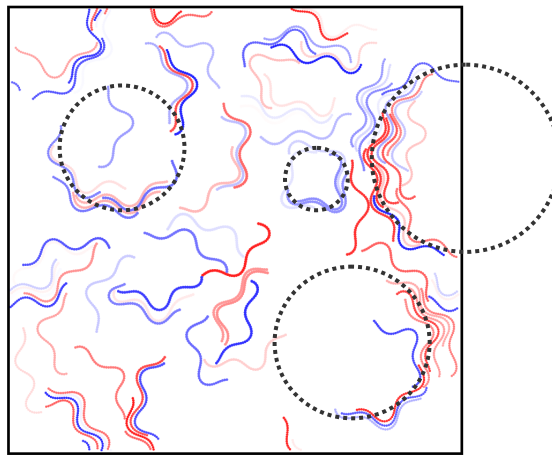
Figure 4.27: The snapshots of an MPC simulation of curved-flagellum system of $\rho_f L_f^2$=6.25 and σ_f=0%. Different flagella are denoted by different colors. The circles of dotted lines indicate the curvature of some clusters.

contributes to the correlation between beat phase and sperm position within a vortex, as found in Ref. [32].

4.5 Conclusion

We have simulated the aggregation and clustering behavior of sinusoidal beating flagella in a low-Reynolds-number fluid by the MPC method, and with the AF approximation. In MPC fluid, the flagella are interacting with each other through hydrodynamics, while no HI between the flagella is present in AF simulations. By comparing the results, we distinguish the different contribution of VE and HI to the swarm behavior.

VE in two dimensions is crucial for the swarm behavior of flagella. The hard-core repulsion acts as the strongest alignment mechanism to attune the moving directions of flagella to be parallel or anti-parallel. Despite the undulating motion, the basic swarm behavior of swimming flagella is very similar as that of point SPP with aligning mechanism [25][56] and rSPP with VE (Chapter III), such as the power-law decay in PDF of cluster size. We find both PDF1 and PDF2 by changing the variance of frequency distribution σ_f, and find the power-law dependence of the average cluster size on σ_f.

Although HI is not the essential reason for the swarm behavior, it has strong impact on the cluster configurations and on the shape of PDF. The clusters with HI in a MPC fluid consist of flagella which are well synchronized and tightly stacked, and the clusters extend strongly in their moving directions. In AF simulations, the clusters do not have such extended and compact structure. A huge cluster in MPC fluid looks like a huge "train" with all its components aligned in the same direction. This phenomenon is related to that found in the rodent sperm experiments [23]. The extended cluster in MPC is motile although the moving velocity decreases with its size. On the other hand, HI makes the PDF deviate from the power-law decay at small cluster size, and yields a different exponent from AF simulations in the power-law dependence of average cluster size on the variance σ_f of the frequency distribution.

We also present some simulations of curved-flagellum system. In AF simulations, the vortices of clusters are formed, which is similar to the vortices in sea-urchin sperm experiments [32]. However, in MPC simulation, the vortices are not stable due to the strong HI in 2D. Thus, we speculate that VE plays an important role in this sea-urchin-sperm experiment where sperm are swimming in a quasi-2D environment, while HI in 3D might mainly contributes to synchronization of sperm tails in a vortex.

V.   Coarse-grained sperm model in 2D

A sperm is a sinusoidal beating flagellum with a head attached in front. The head generates viscous resistance and breaks the symmetry of configuration. We consider sperm with an average spontaneous curvature $c_{0,tail}=0$ on tails and an average beat frequency $f_0=1/120$. For our sperm model, the tail length is $L_s=50a$, and the wave number $q=4\pi/L_s$. Thus there are two sine waves propagating on the tail to mimic the shape of a sea-urchin sperm tail. The sperm model swims smoothly forward with the velocity $u_{single}=0.016\pm0.001$. Like for flagella, the diffusion coefficient of a sperm due to the thermal fluctuations of the MPC fluid is very small because of its large size, on the order of 10^{-4}[95]. This implies that the time a sperm needs to cover a distance of half the length of its flagellum by passive diffusion is more than a factor 10^4 larger than the time to travel the same distance by active swimming. Therefore, diffusion plays a negligible role in our simulations. The energy consumption per unit time is $P_{single}=25.2\pm2.4$, corresponding to the energy consumption per beat about 3000. We estimate a Reynolds number $Re=2A_{tail}u_{single}/v\approx0.03$ for our sperm model, where $A_{tail}=3.2a$ is the beating amplitude of the tail.

5.1 Flow field of trapped sperm

We trap the center of head and the common particle of mid-part and head by strong harmonic potentials. Thus the sperm is captured. It cannot move forward against the harmonic potentials, but still can push the surrounding fluids backwards by the beating tail. Fig. 5.1a shows the flow field of one sperm. The flow field, as well as the sperm configuration, is the average over 500 beats at the same beating phase. The thermal fluctuations of MPC fluid are reduced by this averaging procedure. In

(a)   (b)
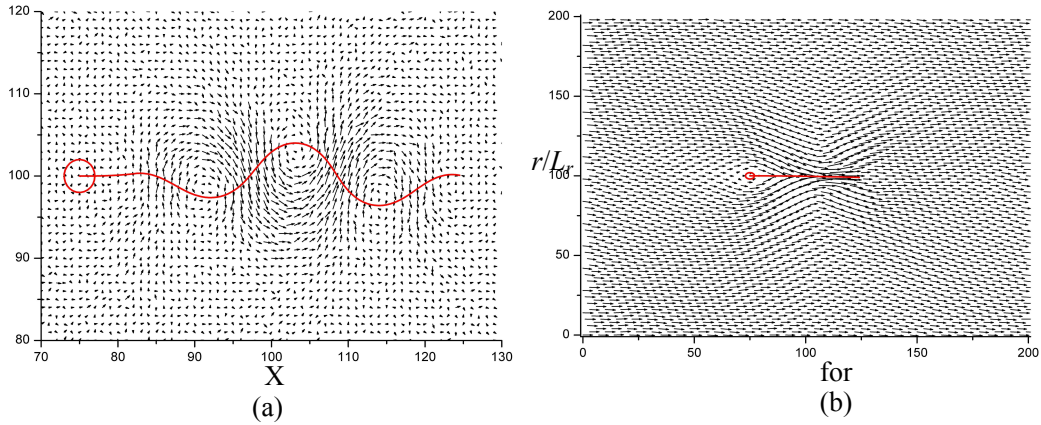
Figure 5.1: The flow field of a single swimming sperm. (a) The flow field of a special phase averaged over 500 beats (with average flow velocity subtracted). (b) The flow field averaged over a whole beat.
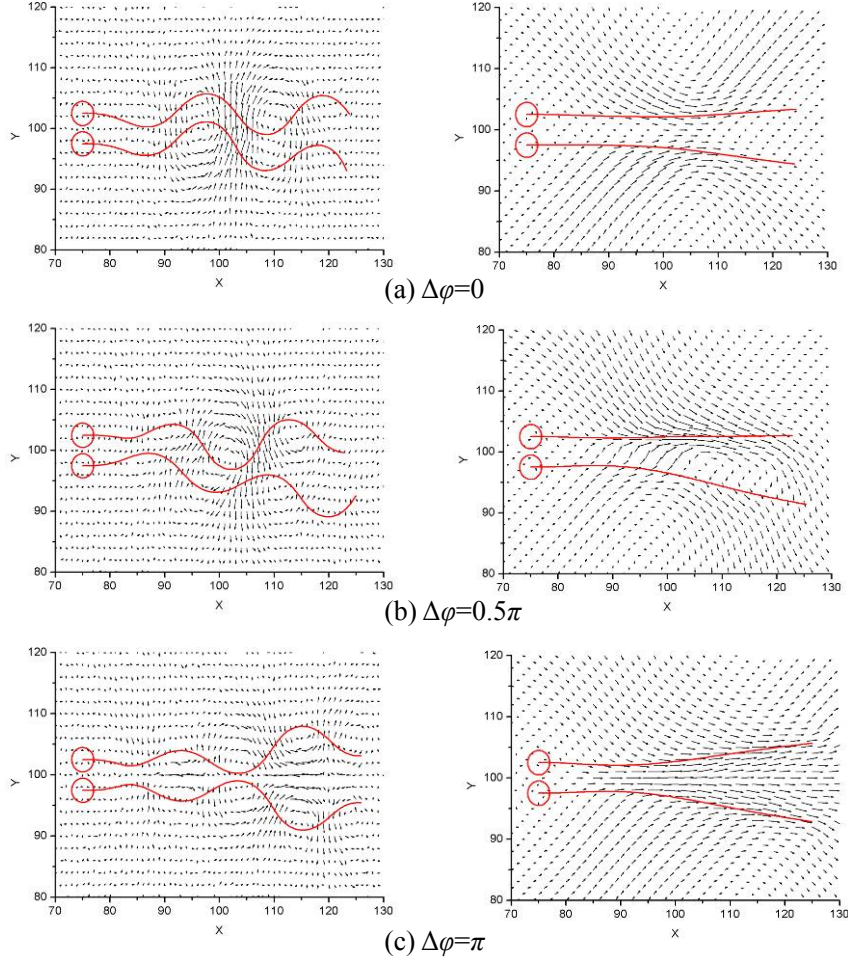
Figure 5.2: Flow field of the cooperating sperm with different $\Delta\varphi=\varphi_2-\varphi_1$. The plots on the left show the flow field at a specific phase. The plots on the right show the flow field averaged over a whole beat. All fields are plotted with average flow velocity subtracted. Note that the shape of the tail responds to the hydrodynamic forces generated by the other sperm.

addition, the flow field drawn here actually is the result of fluid velocity field of a captured sperm minus a constant field of average flow velocity of the fluid,

$$\mathbf{v}(x,y) = \mathbf{v}_{\text{flow}}(x,y) - <\mathbf{v}_{\text{flow}}>_{\mathbf{r},t}$$

where $\mathbf{v}$ is the vector field drawn in Fig. 5.1a, $\mathbf{v}_{\text{flow}}$ is the real flow field in the simulation and $<\mathbf{v}_{\text{flow}}>$ is the flow velocity averaged over the whole simulation box and time. Thus we transfer our reference system from the sperm to the center of mass of fluid, which corresponds to the experimental reference system.

The sperm moves forwards. The velocity of fluids inside the head is approximately the same as head velocity. Vortices of flow are formed by the beating tail. Note that the sperm is swimming at the low Reynolds number. The vortices will disappear immediately if the tail stops beating. The flow field of sinusoidal beating motion was visualized by Gray [12] in the nematodes experiments. The trajectories of colloids near the swimming nematodes embedded in a thin film of viscous fluid were

tracked. The pattern of the colloid trajectories, which corresponds to the flow line, is similar to our flow field diagram. The flow field of a sperm tail with only one complete sinusoidal shape in a two-dimensional fluid was calculated in the simulations of Fauci et al [15][31] also. The vortices are "pushed" backwards and the sperm moves forwards. An efficiency coefficient can be defined as $S_{slip}=(v_{wave}-v)/v_{wave}$ [12], where v_{wave} is the propagation velocity of the sinusoidal wave on the tail, and v is the forward velocity of swimmer. The smaller is S_{slip}, the more efficient the swimming is. In our sperm simulations, S_{slip} is approximately 92%. For Taylor's calculation at Re=0, the velocity of an infinite string beating in 2D is [16]

$$\frac{v}{v_{wave}} = \frac{2\pi^2 A_{wave}^2}{\lambda_{wave}^2}\left(1 - \frac{19}{4}\frac{\pi^2 A_{wave}^2}{\lambda_{wave}^2}\right)$$

where λ_{wave} is the wave length and A_{wave} is the amplitude of beating. Applying our parameters $\lambda_{wave}=25a$, $A_{wave}=3a$, we get $S_{slip}=90.8\%$ for Taylor's beating string is, which is roughly the same as our simulation result.

Fig. 5.1b is the flow field averaged over a complete beating period. The configuration of sperm is also averaged over the whole beat, thus the tail is straight. Different from Fig. 5.1a, the flow field takes the center of mass of the sperm as the reference system. In the averaged flow field diagram, the vortices made by the tail are averaged out. The fluid near the tail is pushed backwards. At the distance, the flow field is a constant, which corresponds to the swimming velocity of free sperm, or the transportation velocity of the tail.

A more interesting thing is to analyze the flow field of two sperm interaction through hydrodynamics. Two sperm with straight configurations are put parallel with a distance of $5a$ between their heads. Each sperm is localized by strong harmonic potentials in the same way as we did for a single sperm. Technically, we collect data of the third beat after they start beating to avoid the influence of the initial state. When the third beat is finished, we restart the system with new random numbers. The simulation is repeated for 500 times to get averaged fields. Since the strong hydrodynamic attraction effect will gradually pull synchronized tails to stick together, we cannot do the averaging on time. Note that all fields shown in Fig. 5.2 are the results of real flow fields minus a constant field of average velocity.

Fig. 5.2 shows the flow field of a cooperating sperm pair with different phase differences $\Delta\varphi$. When $\Delta\varphi=\varphi_1-\varphi_2=0$ (Fig. 5.2a), the sperm tails are beating synchronized and the elongated vortices are formed. Since the tails are locked in phase and close in space, they can be considered as a thick and large "tail". The flow field diagram as well as the average flow field diagram is very similar to that for a single sperm in Fig. 5.1, with only a few differences, such as the amplitude of velocities and the shape of vortices. Fig. 5.2b shows the flow field of two sperm with

$\Delta\varphi$=0.5π. Since the parallel mid-pieces are captured, the tails cannot get synchronized, but they are deformed. The beating amplitude of the tails is changed. The lower one has the smaller amplitude because the hydrodynamic force is pulling to the right to extend the tail, whereas the upper one shrinks a little and increases the amplitude because the total hydrodynamic force on it is pulling to the left. The interacting force through hydrodynamics between two sinusoidal beating strings in 2D was calculated in Taylor's work [16]. Imagine we release the sperm, the upper one will move relatively more forward due to the viscous force on the tail, while the lower one will move relatively less forward. Then they are synchronized. In the diagram of the average flow field of $\Delta\varphi$=0.5π, the extension and the shrinking of the averaged configurations of two tails are clearly seen. The flow field is not symmetric due to the phase difference. Fig. 5.2c is the flow fields of two sperm with $\Delta\varphi$=π. $\Delta\varphi$=π is a special case in which the tails are not synchronized but the system is symmetric. If the sperm are not trapped by harmonic potentials, the symmetry will be broken by the thermal fluctuations, and then two sperm can get synchronized.

5.2 Two-sperm simulations

5.2.1 Synchronization and attraction

We consider two sperm, S1 and S2, with the same beating frequency f=1/120, and the same spontaneous curvature $c_{0,tail}$=0. They are placed inside the fluid, initially with straight and parallel tails at a distance d=5a (*i.e.* with touching heads). They start to beat at t=0 with same frequency f=1/120 and different phases φ_1 and φ_2. The initial positions of sperm do not matter too much, because two freely swimming sperm always have the chance to come close to each other after a sufficiently long simulation time.

In the dynamical behavior of these hydrodynamic interacting sperm, the same effects seen in our flagellum simulation are found, short-time "synchronization" and a
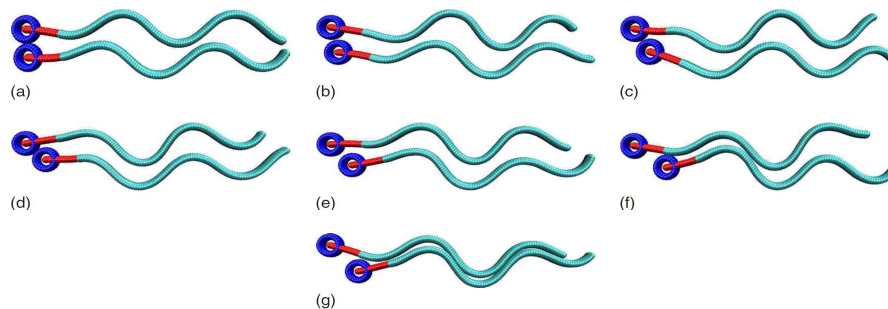
Figure 5.3: Snapshots of two sperm with same frequency and different phases φ_1 (upper), φ_2 (lower), and phase difference $\Delta\varphi$=$\varphi_2$$-$$\varphi_1$=0.5$\pi$. (a) tf=1/6 initial position; (b) tf=2/3; (c) tf=7/6; (d) tf=5/3; (e) tf=13/6; (f) tf=61/6; (g) tf=601/6. From (a) to (e), the synchronization process takes place. The tails are already beating in phase in (e). From (e) to (g), two synchronized sperm form a tight cluster due to hydrodynamic attraction. [Yang2008]

longe-time "attraction" process. If the initial phase difference $\Delta\varphi=\varphi_2-\varphi_1$ at time $t=0$ is not too large, an HI synchronization takes place, which is accomplished within a few beats. This process is illustrated in Fig. 5.3a-e by snapshots at different simulation times. The synchronization time depends on the phase difference, and varies from about two beats for $\Delta\varphi=\varphi_2-\varphi_1=0.5\pi$ (see Fig. 5.3) to about five beats for $\Delta\varphi=\pi$. A difference in swimming velocities adjusts the relative positions of the sperm. After a rapid transition, the velocities of two cells become identical once their flagella beat in phase. Because the initial distance between tails $d=5a$ is smaller than the beating amplitude $2A_{tail}=6.4a$, the sperm tails can touch when they start to beat for $0.6\pi<\Delta\varphi<1.4\pi$. This geometrical effect is reduced by the hydrodynamic interaction, which affects the beating amplitude. In case contact occurs, it accelerates the synchronization. In order to avoid this direct interaction due to volume exclusion, we have also performed simulations of two sperm with initial distance $d=10a$, and find the synchronized state achieved within several beats, as in the simulations with $d=5a$. Thus, the synchronization effect is of purely hydrodynamic origin. Since the beating phase at time t is determined by f and φ_s, which are kept constant in our simulations, our model sperm can only achieve synchronization by adjusting the relative position.

Our results are in good agreement with the prediction of Taylor [16], based on an analytical analysis of two-dimensional hydrodynamics, that the viscous stress between sinusoidally beating tails tends to force the two waves into phase. The same phenomenon has also been observed by Fauci and McDonald [15] in their simulations of sperm in the presence of boundaries, and has been called "phase-locking" effect. A similar effect of undulating filaments immersed in a two-dimensional fluid at low Reynolds number was seen by Fauci in Ref. [31].

Synchronization is a fast process, which is achieved in at most ten beats in our simulations. Hydrodynamic attraction, takes much longer time. Two synchronized and separated sperm gradually approach each other when they are swimming together, as if there was some effective attractive interaction between them. The only way in which the sperm can attract each other in our simulations is through the hydrodynamics of the solvent. This effect takes several ten beats to overcome the initial distance of $d=5a$ between the tails. The final state of attraction, in which the sperm tails are touching tightly, is shown in Fig. 5.3g.

In the simulations of Ref. [15] hydrodynamic attraction is not reported, because they considered a sperm pair confined between two walls. There is an evident tendency for a single sperm to approach the wall. When two parallel sperm are placed between the walls, as mentioned in Ref. [15], there seems to be a critical initial distance between the sperm, below which synchronization occurs, and above which swimming towards the wall occurs. Our understanding is that, in their simulations, the
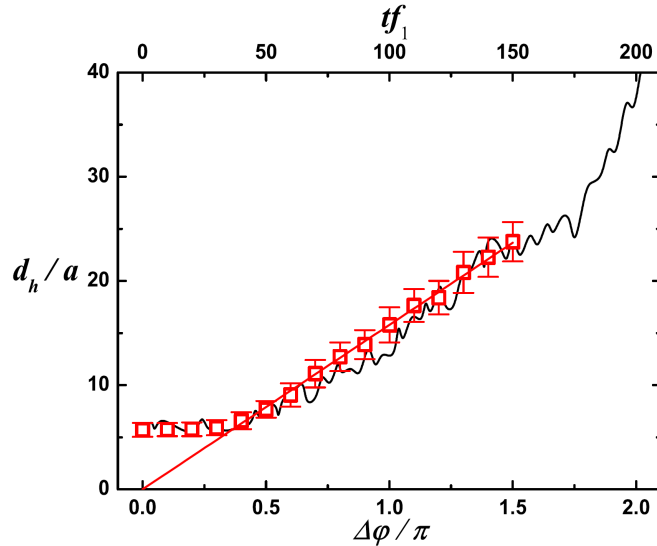
Figure 5.4: Head-head distance d_h of two cooperating sperm. Simulation data are shown for fixed phase difference (□), with error bars denoting the standard deviation. The interpolating (red) line is a linear fit for $0.4\pi<\Delta\varphi<1.5\pi$. The distance d_h is also shown as a function of time tf_1 (top axis) in a simulation with a 0.5% difference in the beat frequencies of the two sperm (solid black line).

viscous drag towards the walls was competing with the viscous attractive effect between sperm. Hence in some cases, they could only see a synchronization effect, and neither a clear towards-wall tendency nor a distinguishable attraction effect. The hydrodynamic attraction was masked by the presence of the walls.

To analyze the cooperating sperm pair in more detail, we choose the head-head distance d_h to characterize the attraction and synchronization, because it is easy experimentally to track the head position. The dependence of d_h on the phase difference is symmetric with respect to $\Delta\varphi=0$ because of the symmetry of the sperm structure. Thus, we show in Fig. 5.4 only results for $\Delta\varphi>0$. There is a plateau at about $d_h=5a$ for $\Delta\varphi<0.4\pi$, which corresponds to the sperm heads touching each other. For $\Delta\varphi>0.4\pi$, d_h increases linearly with $\Delta\varphi$. Finally, for $\Delta\varphi>1.5\pi$, the phase difference is so large that the attraction is not strong enough to overcome the environmental fluctuations and pull the sperm close together. Although synchronization still occurs at the beginning, the two sperm leave each other soon after.

Riedel et al. [32] also see such a linear relation in their experiments of sea-urchin sperm vortices. They define the beating phase of a sperm by its head oscillation, and an angular position of the sperm head within the vortex. In this way, the beating phase difference of the other sperm in the same vortex was found to have a linear relation with the angular position difference, which corresponds to the head-head distance in our simulations.

So far, we have considered sperm with a single beat frequency. In nature, sperm of the same species always have a wide distribution of beat frequencies. For example,
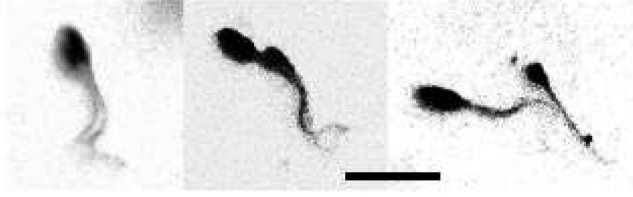
Figure 5.5: Snapshots of two synchronized human sperm in experiment at different times [63][93]. (Left) Two sperm with initially well synchronized tails and very small phase difference; (Middle) the sperm are still swimming together and are well synchronized after 4 seconds; a phase difference has developed; (Right) the sperm begin to depart after 7 seconds. The scale bar corresponds to a length of 25 μm.

the beat frequency of sea-urchin sperm ranges from 30Hz to 80Hz [29][29], and the frequency of bull sperm ranges from 20Hz to 30Hz [87]. Thus, we assign different beat frequencies to two sperm, $f_1=1/120$ and $f_2=1/119.4$, corresponding to $\Delta f/f_1 \approx 0.5\%$, but set the same initial phases $\varphi_s=0$. This implies that the phase difference of the beats between the two sperm increases linearly in time,

$$\Delta\varphi = 2\pi\left(f_2 - f_1\right)t$$

The black line in Fig. 5.4 shows the head-head distance versus time. It agrees very well with the data for fixed phase differences. At $tf_1=150$ where $\Delta\varphi \approx 1.5\pi$, the sperm trajectories begin to depart. This agrees well with our two-flagellum simulation (see Section 4.2).

Fig. 5.5 shows two cooperating human sperm swimming in an in-vitro experiment near a glass substrate [92][93]. The two sperm swim together for more than 6 seconds at a beat frequency of approximately 8Hz. Their tails remain synchronized during this time, while the head-head distance and phase difference increases with time. After a while, the sperm leave each other because the phase difference becomes too large. There is no indication of a direct adhesive interaction between the sperm.

5.2.2 Energy consumption

As we know from two-flagellum simulations (Section 4.2), the energy consumption of a cooperating pair is much less than two free ones. For our sperm model, although there is a large head present, HI between sinusoidal beating tails still dominants the swimmer's behavior. Thus, the energy consumption of two sperm also decreases through cooperation. Fig. 5.6 displays the energy consumption of two sperm with the same beat frequency $f=1/120$ as a function of the phase difference. As we experienced in the flagellum simulations, even for averages over 10 beats (Fig. 4.4), the data scatter noticeably. Note that all data in Fig. 5.6 are averages over two beats. Thus the error bar is the deviation of the average energy consumption in a time
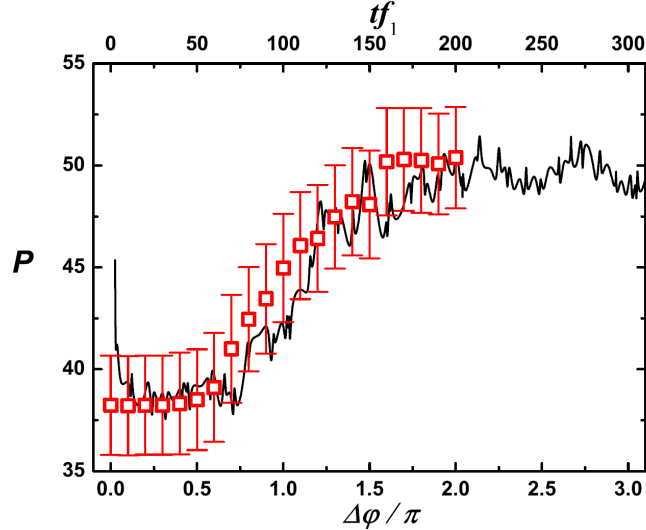
Figure 5.6: Energy consumption per unit time, P, of two cooperating sperm. Symbols show simulation data for fixed phase difference ($\square$), where error bars denote the standard deviation. The solid black line is P versus time t in a simulation with a 0.5% difference in the frequencies of two sperm.

interval of two beats.

The energy consumption P is nearly a constant at small phase difference. This plateau was not seen in the 2-flagellum simulation (Fig. 4.4). it is a consequence of the volume exclusion of the sperm head. P increases for $\Delta\varphi \geq 0.5\pi$ roughly linearly until it reaches another plateau for $\Delta\varphi \geq 1.5\pi$. The second plateau corresponds to two sperm swimming separately, so that the energy consumption is twice the value of a single sperm. Fig. 5.6 also shows the energy consumption of two sperm with $f_1 = 1/120$, $f_2 = 1/119.4$ and $\varphi_1 = \varphi_2 = 0$ as a function of time t. In this simulation, we start with two sperm which are parallel and at a distance $d=5$. For $tf_1 < 25$, the energy consumption decreases as the sperm are approaching each other. The data agrees quantitatively very well with the results for constant $\Delta\varphi$, and reaches a plateau when the cooperating sperm pair departs.

5.3 Multi-sperm MPC simulation

When two sperm with the same beating period happen to get close and parallel, they interact strongly through hydrodynamics and swim together. It is similar to the cooperation of two flagella through hydrodynamics. With this knowledge of HI between two sperm, we now study a system of 50 sperm in a simulation box of $200a \times 200a$. The initial position and orientation for each sperm are chosen randomly. Considering that in real biological systems the beat frequencies are not necessary the same for all sperm, we perform simulations with Gaussian-distributed beating frequencies. The initial phases of all sperm are $\varphi_s = 0$.

We consider a system of symmetric sperm ($c_0 = 0$). Fig. 5.7 shows some snapshots
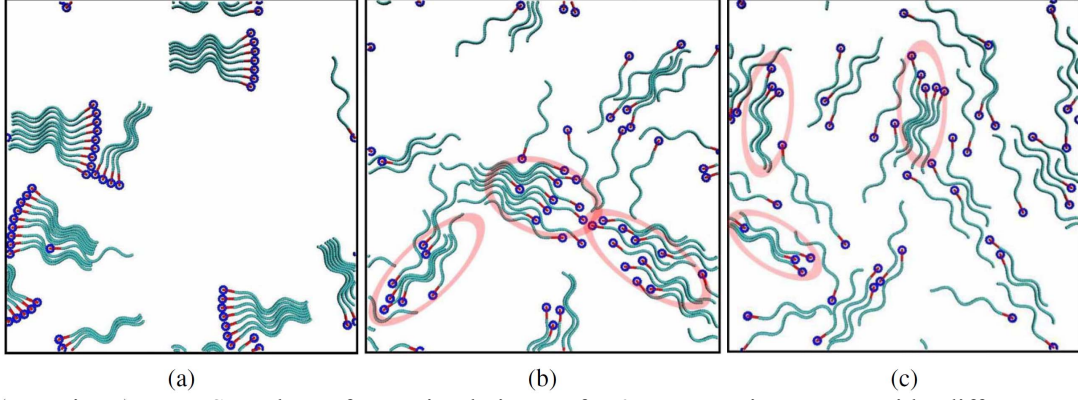
Figure 5.7: Snapshots from simulations of 50 symmetric sperm with different frequency deviation σ_f. (a) σ_f=0; (b) σ_f=0.9%; (c) σ_f =4.5%. The red ellipses in (b) and (c) indicate some sperm clusters. The black frames show the simulation boxes. Note that we employ periodic boundary conditions.

of the systems with different deviation $\sigma_f = \langle(\Delta f)^2\rangle^{1/2}/\langle f\rangle$ of the Gaussian distribution of frequencies. Here, $\langle(\Delta f)^2\rangle$ is the mean square deviation of the frequency distribution, and $\langle f\rangle$=1/120 is the average frequency.

For σ_f =0, once a cluster has formed, it does not disintegrate without a strong external force. A possible way of break-up is by bumping head-on into another cluster. For σ_f>0, however, sperm cells can leave a cluster after sufficiently long time, since the phase difference to other cells in the cluster increases in time due to the different beat frequencies. At the same time, the cluster size can grow by collecting nearby free sperm or by merging with other clusters. Thus, there is a balance between cluster formation and break-up, as shown in the movie of Ref. [94]. Obviously, the average cluster size is smaller for large σ_f than for small σ_f (see Fig. 5.7). The stationary state of balanced break-up rate and formation rate is very similar as the flagella system in Section 4.3.

5.3.1 Average cluster size

To analyze the multi-sperm systems, we define a cluster in a similar way used for flagellum clusters in Section 4.3. If the angle between vectors from the last to the first bead of the tails of two sperm is smaller than $\pi/6$, and at the same time the nearest distance between the tails is smaller than $4a$, which is approximately 1/10 of the length of the tail, then we consider these two sperm to be in the same cluster. Sperm in one cluster have synchronized beats. Due to VE of the large heads, the configurations of sperm clusters are not as tight as that of flagellum clusters (as shown in Fig. 4.5 and Fig. 5.7). The fan-like clusters in Fig. 5.7a is a special case for σ_f =0 and φ_s=0.

By the cluster definition, we find the evolution of the average cluster size $\langle n\rangle$ shown in Fig. 5.8. For σ_f =0, the average cluster size continues to increase with time. All systems in Fig. 5.8 with σ_f>0 reach a stationary cluster size $\bar{n}$ after about 50 beats,
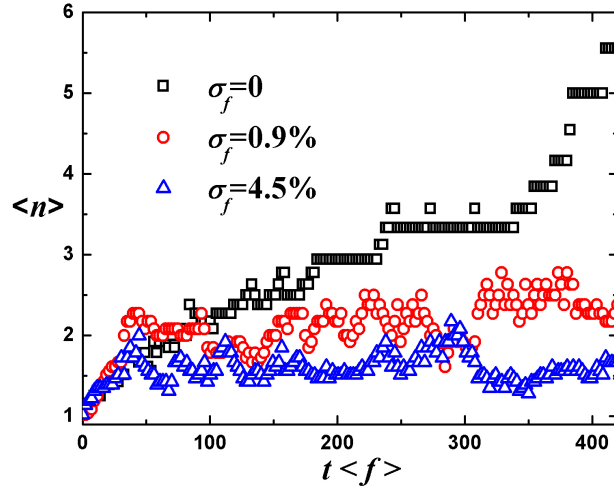
Figure 5.8: Time dependence of the average cluster size, $<n>$, in a system of 50 symmetric sperm with the frequency deviation σ_f, as indicated.
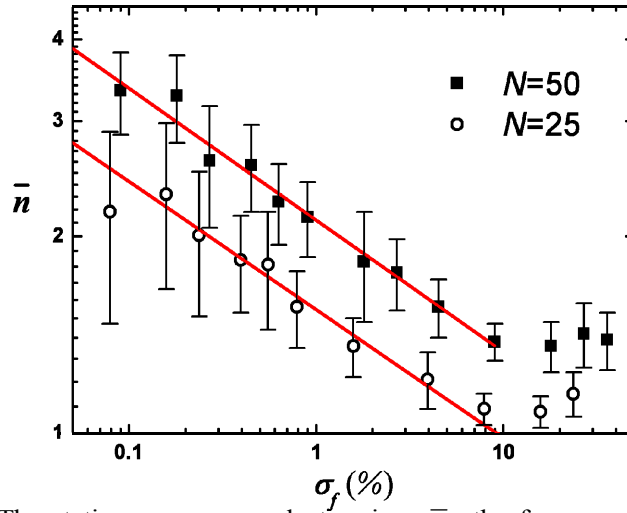
Figure 5.9: The stationary average cluster size, $\bar{n}$, the frequency deviation σ_f. The total number of sperm N is proportional to the number density of sperm. The red lines are fitting power functions with their exponents approximately -0.20.

where $\bar{n}$ is the time-averaged value of $<n>$. The stationary cluster size is plotted in Fig. 5.9 as a function of the frequency deviation σ_f. We find a power-law decay similar as in flagella simulation (Section 4.3.3). The negative power law indicates that the cluster size diverges when $\sigma_f \rightarrow 0$. This tendency is also implied by the continuously increasing cluster size for $\sigma_f = 0$ in Fig. 5.8.

5.3.2 Cluster size distribution

The cluster-size distribution in the stationary state is shown in Fig. 5.10. Cluster-size distributions have been studied in our rSPP and flagella simulations (see Chapter III, IV). A power-law decay of the cluster-size distribution has been found [55], followed by a rapid decay for large cluster sizes due to finite-size effects. A power-law decay of the cluster-size distribution is also consistent with our results for smaller cluster sizes, as shown Fig. 5.10. We attribute the exponential decay of the
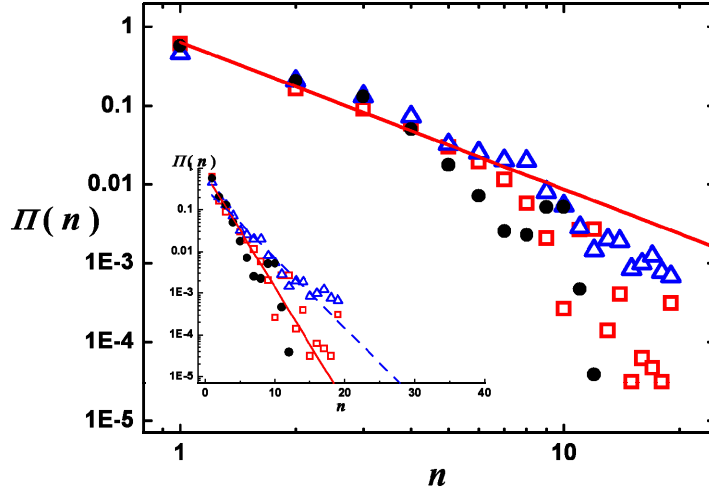
Figure 5.10: Cluster size distribution, $\Pi(n)$. Data are shown for 25 sperm in a $200\times200a^2$ box ($\bullet$), 100 sperm in a $400\times400a^2$ box ($\square$) [note that both systems have the same sperm density], and 50 sperm in a $200\times200a^2$ box ($\triangle$). The lines correspond to a power-law distribution $n_c^{-1.8}$. The inset shows the same data in a semi-logarithmic representation. The line indicates an exponential distribution.

cluster-size distribution for larger cluster size, which is apparent in the inset of Fig. 5.10, due to finite-size effects of simulation boxes. The sperm number from 25 to 100 is far from enough. And the data still scatter a lot for large clusters, which indicates not long enough simulation time.

5.3.3 Cluster forward velocity and energy consumption

To analyze the energy consumption of sperm clusters, we consider a special case where sperm of the same frequency are prearranged to pack tightly and to be synchronized, as shown in the inset of Fig. 5.11a. The phase difference between neighbor ones is $\Delta\varphi=0.4\pi$. A simple linear relationship between the energy consumption of the sperm cluster and the cluster size is shown in Fig. 5.11a. From the
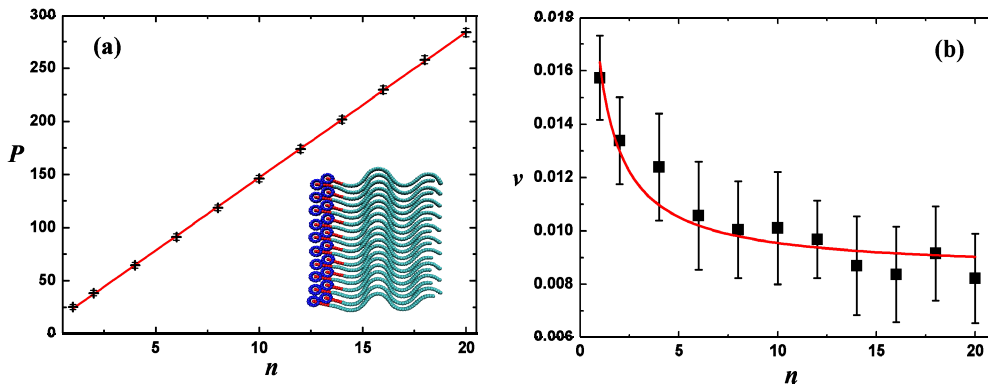
Figure 5.11: (a) Energy consumption per unit time, P, of sperm clusters as a function of cluster size n. Symbols indicate simulations results. The fit line (red) is given by $P=13.7n+10.1$. The inset shows an illustration of a prearranged cluster of 20 sperm. (b) Center-of-mass speed of sperm clusters as a function of cluster size n. The fit line (red) is given by $v = 0.00334\sqrt{6.42+16.4/n}$.

linear fit of the data, we obtain an energy consumption per sperm for an infinitely large cluster, P/n=13.7. Thus, a freely swimming sperm can reduce its energy consumption by almost a factor 2 by joining a cluster.

The swimming speed of a sperm cluster decreases slowly with increasing sperm number, as shown in Fig. 5.11b. When flagella are very close, with distances smaller than the size of a MPC collision box, hydrodynamic interactions are no longer properly resolved. Instead, the collision procedure yields a sliding friction for the relative motion of neighboring flagella. Thus, the energy of the beat is not only used for propulsion, but also to overcome the sliding friction. The energy consumption of tail-tail friction is proportional to the number of neighbor pairs, and the hydrodynamic resistance of moving the whole cluster is proportional to the cluster size and speed. Thus, the total energy consumption can be written as [63]

$$P = Cn_c v^2 + p_f(n_c - 1) \qquad\qquad [5.1]$$

where p_f is the energy consumption due to tail-tail friction, and C is a constant. With the relation P=13.7n_c+10.1 obtained above, the data for the cluster speed can be fitted to Eq. 5.1, which yields p_f=7.28 and C=8.96×10^4. Thus, the cluster speed reaches a non-zero asymptotic value $[(13.7-p_f)/C]^{1/2} \approx 0.0085$ for large cluster size, about a factor 2 slower than a single sperm.

Note that the estimation of the speed of an infinitely large cluster is an extrapolation for special case of a prearranged cluster. A cluster in a multi-sperm simulation with random initial state can have many different configurations. The rough estimation is just an attempt to understand the relation between the energy consumption and the forward velocity.

5.4 MPC simulation of bended sperm

In nature, sperm have an abundance of different shapes. In particular, these shapes are typically not perfectly symmetric. The asymmetric shape can cause a curvature of the sperm trajectory [20][76]. For example, sea-urchin sperm uses the spontaneous curvature of the tail to actively regulate the sperm trajectory for chemotaxis [90][91]. In our simulations, we impose an asymmetry of the tail by employing a non-zero spontaneous curvature c_0.

We consider curved sperm tails, with c_0 =0.04/a, which results in a mean curvature of the trajectory of a single sperm of $c_t a$=0.041±0.009. For sperm with curved tails, the head-head distance $d_h(\Delta\varphi)$ is not symmetric about $\Delta\varphi$=0, as shown in Fig. 5.12. Here $\Delta\varphi$ is defined as the phase of the sperm on the inner circle minus the phase of the sperm on the outer circle. The steric repulsion of the heads causes a plateau of the head-head distance at d_h=5a for small phase differences $\Delta\varphi$, as in Fig. 5.4 for symmetric sperm. For $\Delta\varphi<-\pi/2$ and $\Delta\varphi>\pi/4$, the head distance increases
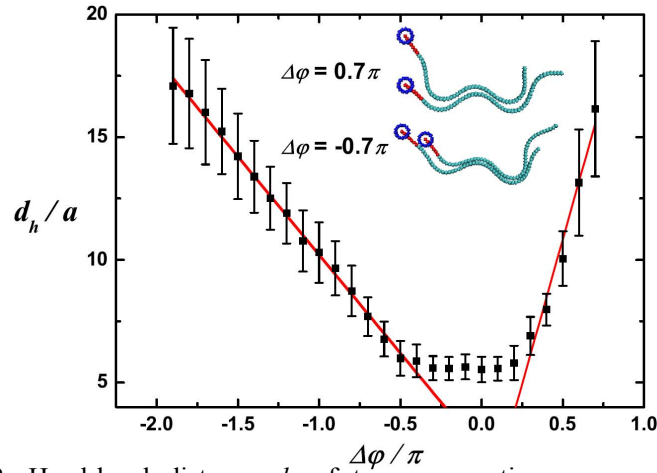
Figure 5.12: Head-head distance d_h of two cooperating sperm with spontaneous curvature c_{0l}=0.04/a as a function of the phase difference $\Delta\varphi$. The error bars represent standard deviations. Lines are linear fits to the data in the range -1.9π<$\Delta\varphi$<-0.5π and 0.3π<$\Delta\varphi$<0.7π, respectively. The inset shows two typical conformations with positive and negative phase difference.

linearly with increasing phase difference, with a substantial difference of the slopes for $\Delta\varphi$<0 and $\Delta\varphi$>0, see Fig. 5.12. The two sperm depart when $\Delta\varphi$>0.7π. For $\Delta\varphi\leq-2\pi$, the sperm pair briefly looses synchronicity, but then rejoins with a new phase difference $\Delta\varphi'$=$\Delta\varphi$+2π.

The energy consumption P for sperm with spontaneous curvature (see Fig. 5.13) also increases sharply at $\Delta\varphi$=0.8π and stays at the plateau with P=51.0$\pm$2.8 for larger $\Delta\varphi$, as the sperm are swimming separately. However, for $\Delta\varphi$<$-\pi/2$, P increases rather smoothly until the cooperation is lost for large phase differences.

The strong curvature of the tail breaks the symmetry of the head-head distance d_h and the energy consumption P in $\Delta\varphi$, but the effect of synchronization and attraction are still present and play an important role in the cooperation of sperm pairs.
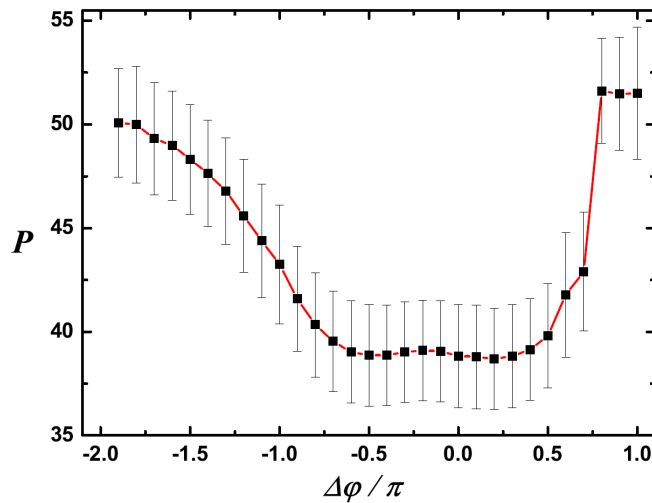
Figure 5.13: Energy consumption per unit time, P, versus phase difference $\Delta\varphi$ of two sperm with spontaneous curvature c_0 =0.04/a of their tails. The error bars represent standard deviations.

We also simulated systems containing many curved sperm. However, the hexagon array of vortices seen in the curved flagella simulation (Section 4.4) does not emerge in the sperm model case. For the flagellum system, 2D HI is too strong and prevents the formation of vortices. For sperm, the large head is another reason for the absence of vortices.

5.5 Conclusion

5.5.1 Comparison with flagellum simulation

The difference between the flagellum model and the sperm model is a large head added in front of the sperm tail. The head generates strong viscous resistance, so that the beat shape of the tail is modified and the sperm velocity is lower than the velocity of a single flagellum.

Although the head makes it tougher for sperm to move forward, HI between the sinusoidal beating tails is strong enough that the cooperation and swarming behavior of a multi-sperm system is basically the same as in a multi-flagellum system.

We have simulated the HI between sperm in 2D by the multi-particle collision dynamics (MPC) method. The same effects in flagellum cooperation, synchronization and attraction, are found in sperm simulations. When two sperm are close in space and swimming parallel, they synchronize their tail beats by adjusting their relative positions. This process can be accomplished in a very short time, less than 10 beats. Two such synchronized sperm have a tendency to get close and form a tight pair. This process takes much longer time than synchronization. It usually takes about 100 beats to overcome a distance of 1/10 tail length between two sperm in our simulations.

For a multi-sperm system, the average cluster size increases if the deviation of frequency distribution decreases. A distribution of frequencies leads to a stationary cluster-size distribution with a finite average cluster size, which decreases with a power law of the frequency deviation. Furthermore, the average cluster size increases with increasing sperm density. The probability to find a cluster of a given size decreases with a power law for small cluster sizes; an exponential decay for large cluster sizes in sperm simulations is attributed to finite-size effects of simulation boxes.

Although the existence of a head does not influence the 2D sperm cooperation qualitatively, there are quantitative differences. For example, plateaus in the head-head distance (Fig. 5.4) and the two-sperm energy consumption (Fig. 5.6) at small phase differences emerge. Also, the head leads to a looser cluster configuration than flagellum clusters, which decreases the stability of a large cluster.

5.5.2　Comparison with experiments

In sperm experiments, large bundles have been found in some species, like fish flies [36][35] and wood mice [23][37][23]. For fish-fly sperm, this has been attributed to some agglutination of the sperm heads to keep the size and structure of the bundles. Wood mouse sperm, released into an in-vitro laboratory medium initially in single cell suspension [37], form large bundles containing hundreds or thousands of sperm as motile "trains" within 10 minutes. Motile bundles of 50-200 sperm were also found in the after-mating female's body, as well as many non-motile single sperm. The hook structure on the head of wood mouse sperm is believed to favor the formation of such huge cluster in in-vitro experiments.

In our simulations, sperm clusters are always seen at sufficiently high concentrate, e.g. as marked in Fig. 5.7, after the system has reached a dynamically balanced state of cluster sizes. Thus, we predict that volume exclusion and hydrodynamic interaction play an important role in the cluster formation of healthy and motile sperm.

However, there are few reports on sperm cooperation through hydrodynamics and swarm behavior. This is due to several reasons. First, scientists so far were more interested in single sperm behavior and motion mechanisms, such as the response to the visco-elastic environment [28] and chemotaxis [90] etc. In experiments, the sperm are diluted thousands or even more times than their original concentration in vivo. At a really low density of moving agents, according to our results of rSPP and flagellum, the system is in a random state. The possibility for a sperm to find another is low, thus cooperation is hardly found. Also, large clusters are nearly impossible to find because the probability to find a cluster decreases with as a power-law function of its size. Second, as indicated by comparing with flagellum simulations, a head which has strong viscous resistance and VE will influence the clustering behavior quantitatively, although not qualitatively. If the head becomes very small, the sperm model transforms back to the flagellum model. If the head is very large, it is like a colloidal particle, and HI between tails is negligible. Third, since the cluster size decreases with increasing deviation σ_f of the distribution of beat frequencies, our results are consistent with the experimental observation that if the sperm are hyperactivated [37], which is an abnormal beat mode, or if some sperm are dead, the clusters fall apart. At large σ_f, hydrodynamic synchronization between simusoidal beating flagella breaks clusters quickly. The variance of frequencies of sperm from same species but different individuals might be large; however, the frequency distribution of sperm from an individual male is not known.

VI. Flagella and sperm simulations in 3 dimensions

The simulations of rod-like self-propelled particles, flagella and sperm in two dimensions (2D) have shown interesting swimming and swarming behavior, as described in Chapter III~V. Several of these dynamical properties resemble those of experimental systems in three dimensions. However, there are several reasons why a quantitative prediction of the behavior of real flagella and sperm requires simulations of these systems in three dimensions (3D).

First, particles in 3D have much more degrees of freedom. For example, the beating plane does not have to be confined in a plane. The tail distorts to cope with the viscous resistance. Also, the swimmer can rotate around its direction of motion, which is impossible in 2D. More freedom degrees imply more complicated behaviors.

Second, two important interactions for the swarming behavior in 2D, volume exclusion (VE) and hydrodynamic interaction (HI), are much weaker in 3D. For VE, it is well known for rod-like particles of length l and diameter d that a volume fraction ψ larger than $4d/l$ is necessary in equilibrium to go from the isotropic to the nematic phase, in which rods align spontaneously. This volume fraction is much larger than the overlap volume fraction $\psi \sim (d/l)^2$. Hydrodynamics in 3D is also very different. A point in 2D corresponds to an infinitely long string in 3D. Thus, the hydrodynamic interaction between point particles in 3D decays as a function of distance as $1/r$, while in 2D there is a much larger-ranged logarithmic decay.

In this chapter, we present some preliminary results of flagella and sperm in 3D. 3D simulations always require far more computer time. In 3D, there are plenty of open questions. Most of the results indicate the complexity of 3D sperm behavior.

6.1 Cooperation of two flagella

A flagellum is the limit of sperm with a very small head. According to our 2D simulation, the cooperation of sperm, especially the hydrodynamic contribution, is mainly due to the beat motion of their flagella. If two 3D flagella cooperate through HI, not-too-large heads will not destroy the similar behavior of two sperm. Thus, we also start from flagellum simulations to observe two-body cooperation in 3D. The beating frequency is $f=1/50$, and the wave number $q=4\pi/Nl_0$ where $N=100$.

6.1.1 Synchronization

Two parallel flagella with straight configuration are put into the MPC fluid with a distance $d=5a$, which is also the distance between their parallel beating planes. When they start to beat, the flagella do not touch each other. The can only interact though

hydrodynamics at the beginning.

Compared to 2D, there are more pathways to achieve synchronization in 3D. Fig. 6.1 shows two flagella with phase difference $\Delta\varphi=0.5\pi$ as an example. At the initial state, the beating planes are parallel, thus the active springs are on the same side in Fig. 6.1. During the process of synchronization, the flagella gain different velocities to shift their relative position and lock in phase, similar as the synchronization in 2D. In addition, they rotate their beating planes due to HI and thermal fluctuations. When the flagella are locked in phase and nearly touch each other, two states with different configurations are found. In most of the cases of our simulations, the flagella reach the state of parallel beating planes, as shown in Fig. 6.1b. The flagella swim together with the distance between front particles proportional to the phase difference. The active springs are on the same side (just as in 2D). Another state, in which the beating planes are anti-parallel, is shown in Fig. 6.1c. Two flagella rotate their beating planes in opposite directions and achieve the final state in which their active strings are on the opposing sides. This happens rarely in the initial state of parallel beating planes. In the simulation with a random initial state, two flagella meet each other with any possible angle between their beating planes. Since the final state of synchronization always has parallel or anti-parallel beating planes, they have to rotate to get synchronized and decrease the distance between their beating planes.

In 2D, two synchronized flagella with the same beating frequency swim together for a very long time because of the strong HI. In 3D, the cooperation is not persistent even for flagella with the same beating frequency. The hydrodynamic attraction effect is weak. The swimming velocity of a flagellum is 0.02. Thus the Péclet number is on the scale of 10^5. So the flagellum body is large enough that the diffusion of a single flagellum is negligible, comparing with its swimming motion.

We define the normal vector of the beating plane of a flagellum at time t as
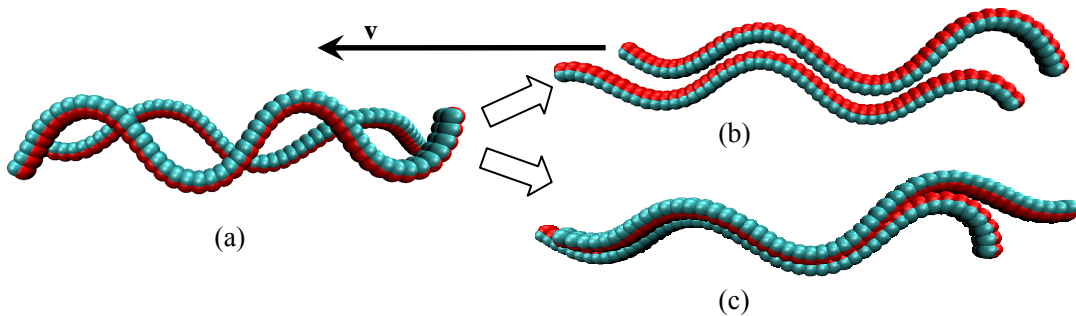
Figure 6.1: The snapshots to show the synchronization of two flagella with a phase difference $\Delta\varphi=0.5\pi$. (a) The initial configuration at $tf=1/12$; (b) phase locking with parallel normal vectors of beating planes; (c) phase locking with anti-parallel normal vectors of beating planes. The red beads are those connected by the active springs, while the cyan ones are connected by inactive springs. The solid arrow indicates the swimming directions
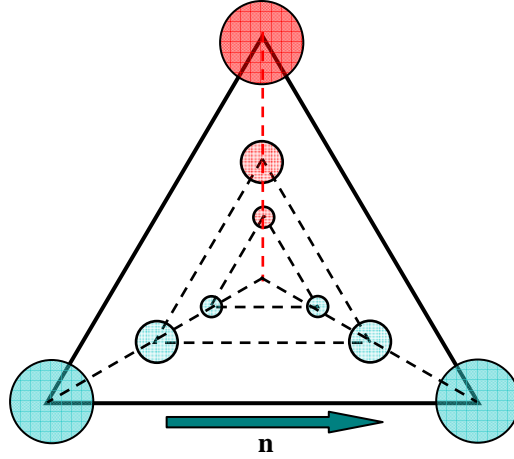
Figure 6.2: The illustration of the definition of the local normal vector **n** of the beating plane. The picture is looking from the front of our flagellum model to its end. The red line are active springs changing their relax length with time. The red beads are connected by the active springs.

follows. The local normal vector **n** at same position x_i along the flagellum is in the direction of the bond opposite to the active filament, as illustrated in Fig. 6.2. For a flagellum not distorted too strongly, we define the normal vector $\mathbf{N}_i$ of its average beating plane of the i-th flagellum as

$$\mathbf{N}_i = \frac{1}{N_{tail}} \sum_{x_i}^{N_{tail}} \mathbf{n}(x_i)$$

When two flagella are synchronized, their beating planes are parallel or anti-parallel. Thus, $\mathbf{N}_1 \cdot \mathbf{N}_2$ is 1 or −1. Fig. 6.3 shows the $\mathbf{N}_1 \cdot \mathbf{N}_2$ of the cooperating pair in Fig. 6.1b as a function of the simulation time. The cooperating pair has parallel beating planes, thus $\mathbf{N}_1 \cdot \mathbf{N}_2$ shows very little fluctuations, less than 5°. Even though the cooperating pair is separated at time tf =200, the beating planes remain parallel due to the viscous resistance to rotate them.

Figure 6.3: $\mathbf{N}_1 \cdot \mathbf{N}_2$ as a function of time t of two cooperating flagella with same frequency and no phase difference, as illustrated in the insert.

6.1.2 Distortion

The correlation function of the normal vectors $\mathbf{n}(x_i)$ along a flagellum is

$$S(\Delta x_i) = <\mathbf{n}(x_i) \cdot \mathbf{n}(x_i + \Delta x_i)>$$

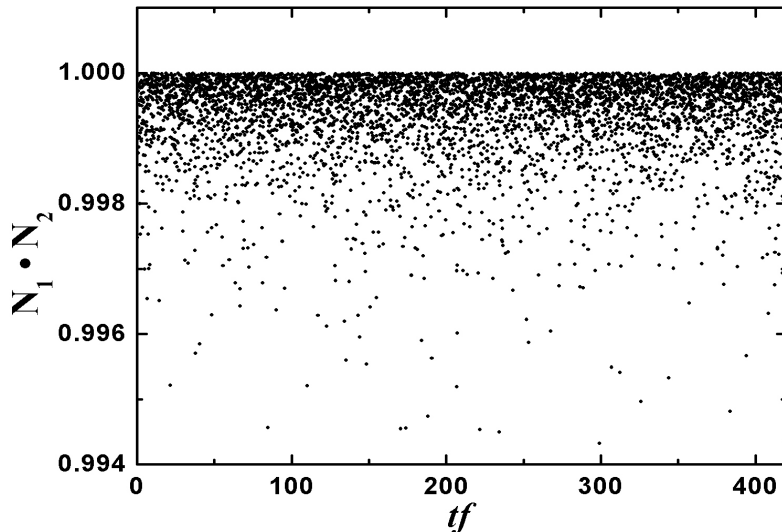where Δx_i is the distance between two segments on the flagellum. $S(\Delta x_i)$ represents the degree of distortion of the beating plane. S equals 1 at $\Delta x_i=0$ and 0 when $\Delta x_i \rightarrow \infty$, if the resistant distortion is finite.

We analyze $S(\Delta x_i)$ of the flagella of a cooperating pair, and compare it with that of a single flagellum, as shown in Fig. 6.4. In both cases, $S(\Delta x_i)$ decreases slowly with Δx_i. For a single flagellum, the average angle between the normal vectors at the front and at the end of a flagellum is approximately 16°. When two flagella form a cooperating pair, they are not only interacting through hydrodynamics, but also collide with each other from time to time. So $S(\Delta x_i)$ decreases faster for a cooperating pair than a single flagellum. For the cooperating pair in Fig. 6.4 the angle is approximately 18°. So, the distortion for flagella in cooperation is stronger than in single suspension.

A stronger distortion means more distortion energy stored in the body and a stronger distortion force. The distortion is not uniformly distributed in the swimmer body. It is strong at the point of collision when two flagella hit each other. Then, the distortion spreads along the flagellum and decays through viscous friction. Due to a weak attraction, two synchronized flagella tend to get closer. When they are very close, the higher probability to collide increases the probability of distortion. When the distortion is too strong, it breaks the cooperation. Two flagella sometimes leave each other due to a collision which slightly changes their swimming directions and beating planes. HI in 3D is not strong enough to recover the cooperation after the
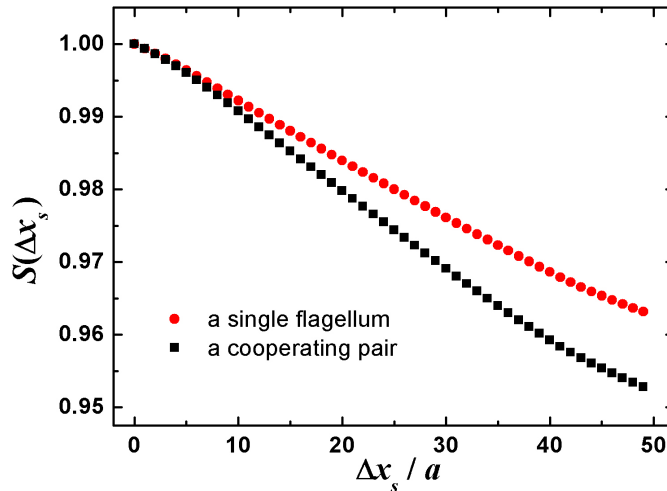

Figure 6.4: The correlation function S of the normal vectors of beating plane at different position on a flagellum. The black square (■) is the result of a cooperating flagella pair. The red bullet (●) is for a single flagellum simulation.

collision.

6.1.3   Influence of hard walls

The self-propelled rod-like particles, such as sperm [17] and nematodes [12], have an aggregation tendency at the boundaries. In a confined space, sinusoidally beating swimmers have strong HI with the boundaries. In 2D, it is found that the hard wall exerts a viscous drag to pull a swimming sperm to the boundary, and an elastic boundary has a shape deformation responding to the beating tail [15]. However, in 2D, the beating plane is always perpendicular to the boundary. In 3D, the beating plane of a single sperm near the hard wall prefers to be parallel to the substrate, because HI with the substrate and generates a viscous repulsion rather then a drag force towards the wall [20]. This repelling force lifts the tail, so that the sperm has a small angle against the wall, which implies a thrust force of sperm head towards the wall. Thus, HI between tail and wall in 3D also helps the sperm accumulation at boundaries, although the detail mechanism is very different from 2D.

We analyze the influence of hard substrates by putting our flagellum model into a confined space. Two hard walls are placed at $z=0$ and $z=30a$. The distance between the walls is smaller then the length of flagella, but is about 10 times of the amplitude of the flagella configuration. At beginning, the flagellum is parallel to the substrates with a straight configuration and at $z=15a$, where the distance to each substrate is equal. The normal vector of the beating plane is parallel to the substrates. VE between the substrate and the flagellum particles is applied by a shifted, truncated Leonard-Jones potential.

After the flagellum starts to beat, it rotates the beating plane to get parallel to the substrates in about 20 beats, although the beating plane is perpendicular to walls initially. The rotation speed is much faster than a single flagellum simulation without substrates. Thus, the rotation is not induced by thermal fluctuations. There is no VE with wall during the rotation. Thus, it is HI with the substrates, which rotates the beating plane.

After the flagellum rotates its beating plane, it declines and approaches one of the substrates. Once it hits the substrate, the flagellum stays at the substrate for a very long time with a constant angle θ against the wall, as illustrated in Fig. 6.5.

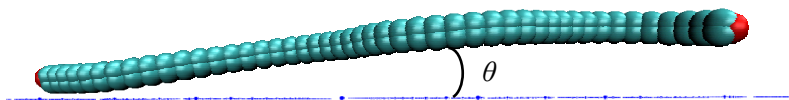Figure 6.5: The snapshot of a single flagellum at the substrate. The end of flagellum tail is lifted by HI, so the flagellum has an angle θ against the substrate. The front of the flagellum is on the left side.

This phenomenon is closely related to sperm motion near boundaries [20]. A sperm has a large head which generates strong viscous resistance force and induce the asymmetry in structure. Our flagellum model does not have the asymmetry on its structure. The asymmetry of our flagellum is the swimming by a propagating wave in fluid which is not time reversible. The angle θ between the beating plane and the substrate indicates that the viscous force induced by HI between the flagellum and the substrate is not uniform distributed on the flagellum body. The repelling force on the end of flagellum is stronger then on the front.

Note that the detail settings of the simulation may influence the results qualitatively. In our simulations, the interaction between the substrates and the flagellum is only volume exclusion. Also, the stiffness of the flagellum may affect to the aggregation tendency at the wall.

6.2 Single sperm simulation

For the study of two sperm cooperation, it is necessary to understand the general properties of our model for a single sperm. The behavior of the 3D sperm model strongly depends on the simulation parameters.

We keep the property of our MPC fluid, of which the total kinematic viscosity is v=1.60. A head of radius r=2a is chosen to generate strong viscous resistance. The beat frequency is f=1/20π. The length of the tail is $N_{tail}l_0$=25a. The length of the mid-part is $(N_{mid}-5)l_0$=5a. The part of the flagellum embedded in the head to stabilize the head-mid piece connection is not considered as the mid-piece. All the other parameters are described in Chapter II. In the single-sperm simulation, we only change the wave number q. $qN_{tail}l_0$ denotes the phase difference between the first and last segment on tail. Thus, the size, stiffness and beating frequency of a sperm are
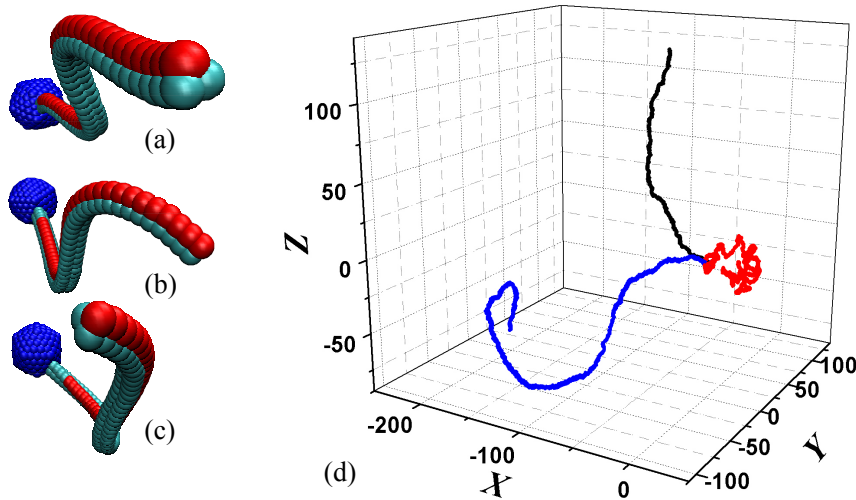

Figure 6.6: Snapshots of sperm with different number of waves on their tail with (a) q=3π/$N_{tail}l_0$; (b) q=2π/$N_{tail}l_0$; (c) q=1.2π/$N_{tail}l_0$. (d) The trajectories of sperm heads with q=3π/$N_{tail}l_0$ (black), q=2π/$N_{tail}l_0$ (blue) and q=1.2π/$N_{tail}l_0$ (red).
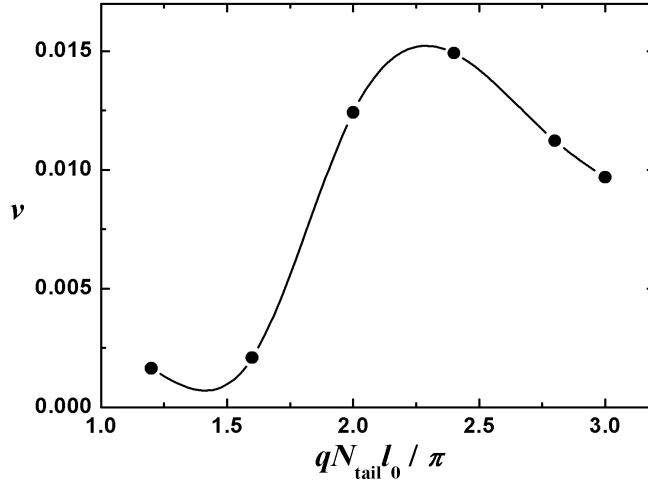
Figure 6.7: The velocity of a 3D sperm as a function of $qN_{\text{tail}}l_0$.

always the same.

The sperm models are put into MPC fluid with straight configuration initially. The tails beat and push the surrounding fluid in order to overcome the viscous resistance of the large head to move forwards. The shape of the tail and the orientation of the beating plane can adjust and distort according to the environmental forces.

Fig. 6.6 shows the snapshots as well as the trajectories of heads of sperm with different q. When q is large enough (see Fig. 6.6a), a quite flat beating plane is found. The tail has almost perfect sinusoidal shape constantly pushing the fluid backwards; thus the sperm moves on a nearly straight line. The head trajectory for $q=3.0\pi/N_{\text{tail}}l_0$ in Fig. 6.6d is weakly curved, although the beating plane is approximately flat. This curvature is mainly due to the asymmetry of our 3D flagellum. We have only one active filament to change the local spontaneous curvature on the tail, and the viscous force encountered by the tail is not quite symmetry due to the discretized structure. When q is smaller (see Fig. 6.6b), the tail is distorted, although its stiffness and length are not changed. The twisting causes an overall curvature of the tail, which makes a helix trajectory of the sperm head, as the blue curve shown in Fig. 6.6d. When q is reduced even further (Fig. 6.6c), the distortion gets stronger and stronger until the curvature on the tail is so large that the sperm gets localized (see Fig. 6.6d).

Fig. 6.7 shows the forward speed as a function of $qN_{\text{tail}}l_0$. The speed is calculated from the displacement of the head in 10 beats, so that the influence of thermal fluctuations is averaged out, and the curvature of the trajectories is taken into account. At small $qN_{\text{tail}}l_0$, where the tail is strongly distorted, the speed nearly vanishes. With increasing $qN_{\text{tail}}l_0$, the distortion of beating plane gets weaker, thus the forward velocity increases until it reaches the highest value at $qN_{\text{tail}}l_0=2.4\pi$. Although the further increasing in q implies less distortion of the beating plane, the amplitude of the tail beat decreases, so that the forward velocity decreases for $q>2.4\pi/N_{\text{tail}}l_0$. Thus, the velocity approaches zero in both limits of $q\to0$ and $q\to\infty$.

6.3 Comparison with single sperm in experiments

The wave number q, which describes the preferred shape of tail, is an internal parameter and is not necessarily the same for each individual in real systems. For example, in the hyperactivated state of human sperm, some individuals gain a higher frequency and higher swimming velocity, while others slow down or even become localized [93]. This might be caused by the diversity of individual structures. A possible way to regulate the sperm motion in hyperactivated state is by changing the wave number q. However, because of the beating mechanism of axoneme is not fully understood yet, it is hard to design an experiment to observe the influence of changing q.

The tail distortion also can be understood in this way. If the environment is too viscous and the bending and twist rigidity is not large enough, the tail prefers a distorted shape rather than its spontaneous configuration with lowest bending and distorting energy. This is the reason for why sinusoidal beat does not exist in bacteria. Although the basic "9+2" axoneme structure is same for bacteria and sperm, the bacteria flagella are much thinner and in a much lower Reynolds number region. Even though the flagellum employs a same motion mechanism as for sperm, the viscous resistance will make it distorted. Thus, a sinusoidal beating is not an efficient motion for small cells as bacteria. *E. coli* swim by rotating flagella of helix structures. The rotation is generated by the protein motors embedded in the cell body.

The experiments of single opossum sperm in different viscous media support our results. As shown in Fig. 6.8 from Ref [37], although the trails of sperm in a low viscosity fluid oscillate and fluctuate, the sperm still can swim forwards in their moving directions. In a highly viscous fluid medium, the sperm are captured by the viscous environment. The trails are localized into small circles, as shown in Fig. 6.8b. We conjecture that the sperm tails are strongly distorted in this case. The opossum

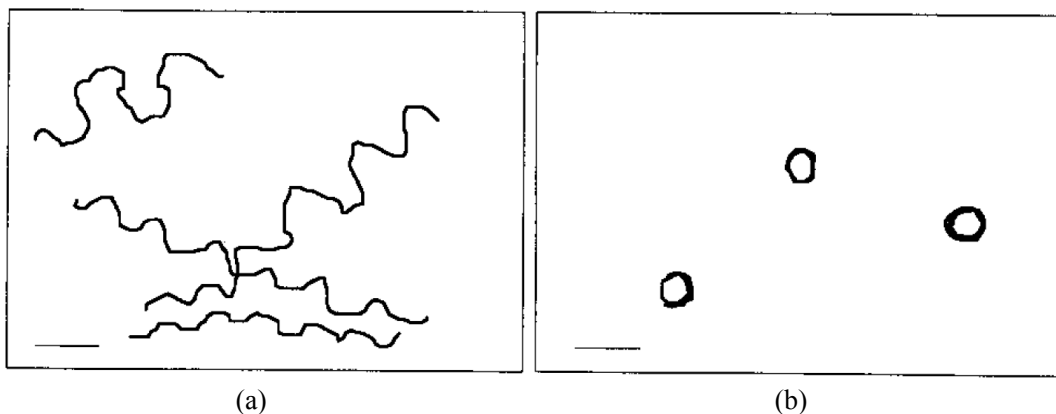(a)   (b)

Figure 6.8: The trails of single opossum sperm over 7 sec in fluid medium with different viscosity μ. (a) μ=2.28 poise; (b) μ=13.50 poise. The bar denotes 100μm. The diagrams are from Ref [Moore1995].

sperm shape was not analyzed in this experiment. By looking at the response of sperm trajectory to the viscosity of fluid medium, an experiment can be designed to analyze the rigidity of sperm tail.

The results of our simulations of a single sperm in 3D suggest that, the wave number q should not be too small; otherwise a tail of high rigidity is needed to keep the beat plane reasonably flat. Also, q should not be too large. It is good enough to use $q=2\pi$ to generate an approximately flat beating plane. A more important problem is that we do not have experimental data for the rigidity of the flagellum. The rigidity of our sperm model is not easily comparable to the experiments.

6.4 Multi-sperm simulation

Our 3D multi-sperm simulations employ a simulation box with the side length $L_x=L_y=200a$ and $L_z=30a$. Two hard walls are put at $L_z=0$ and $L_z=30a$. On x and y directions, we employ periodic boundary conditions.

The total length of a sperm from the head to the end of the tail is $51a$, with the radius of the head $r=1a$ and the length of mid-part $8a$. Thus, the side length of the simulation box on x and y directions are four times of the sperm length, while the distance between the hard walls is smaller than the sperm length. So, the sperm are impossible to be perpendicular to the walls. They are swimming in a strongly confined space that HI with substrates is strong.

Sperm are put into the simulation box with straight configuration, initially. The positions and orientations are not randomly chosen as in 2D, but in a regular array, as shown in Fig. 6.9. The frequencies are chosen from a Gaussian distribution of an average value $<\!f\!>=1/20\pi$. The rescaled standard deviation of the frequencies is $\sigma_f=0.1\%$. The initial phases are chosen from a uniform random number in $[-\pi,\pi]$. The beating planes are perpendicular to substrates.

Once the sperm start to beat, the synchronization and rotation take place. The relative positions of neighbor sperm are regulated according to their phase differences, and the beating planes rotate to get parallel to substrates. After some time, the system
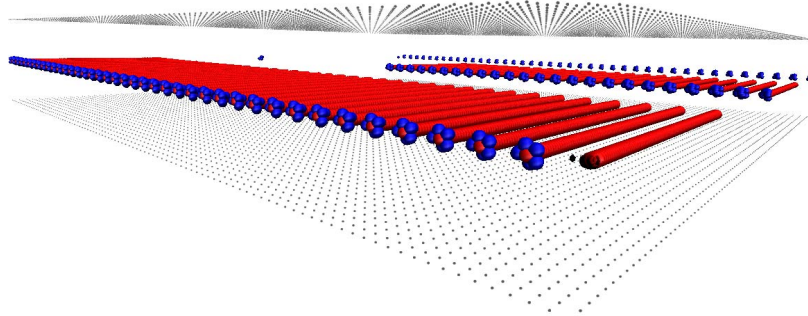

Figure 6.9: The snapshot of a 64-sperm system at time t=0. The sperm are put parallel to each other at the center of box.
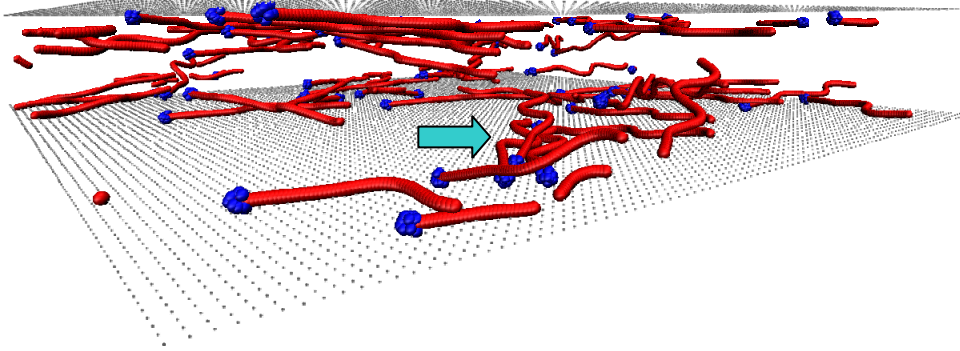
Figure 6.10: The snapshot of the stationary state of a 64-sperm system. The cyan arrow points out a cluster of three sperm with synchronized shape and swimming together. Note that we employ a periodic boundary condition in the directions other than that perpendicular to the substrates.

will at least come to a stationary state as shown in Fig. 6.10. In the stationary state, we see the aggregation near the substrate and some small clusters of cooperating sperm with synchronized configurations.

As our experience from 2D simulations, the simulation box with the side length of only four times of the swimmer length at the periodic direction is too small. The analyzation of the swarming behavior strongly depends on the simulation box size with a constant agent density. However, since our 3D simulations are at a trial stage at the moment, this box size is already good to show quite a lot of behaviors. Also, the swarm behavior needs very-long-time simulations to observe the evolution of system, but the simulation time goes cubic with side length. So, before we start the long-time simulation, we first try small box size and observe the quantities which do not strongly influenced by the periodic boundary condition. The system is much more complicated than in 2D. Thus we only tried two simulations with total sperm number N_s=64 and N_s=128, respectively.

6.4.1 Distortion on tails

The correlation function $S(\Delta x_i)$ of two normal vectors $\mathbf{n}(x_i)$ on the same sperm flagellum with distance Δx_i is shown in Fig. 6.11.

The curve for both systems with different sperm number decreases smoothly. The total number of sperm N_s is proportional to the sperm density. In Fig. 6.11, $S(\Delta x_i)$ decreases faster in system of higher sperm density. The sperm tails are more distorted in a system of higher density for three reasons.

First, the possibility to make cooperation with others is higher. As suggested by 2D simulations, the average cluster size increases with the swimmer density. The cluster size is larger, thus the distortion on tail is stronger.

Second, the collision with other sperm is more frequent. The collisions between sperm cause local distortions on tails. This distortion spread along the tail and decay

through viscous friction.

Third, a sperm is exposed in the flow field of all other sperm cooperating or not cooperating with it. The HI from sperm which are not cooperating can be considered as an environmental noise. The higher sperm density means a stronger environmental noise, which induce a stronger distortion on tails.
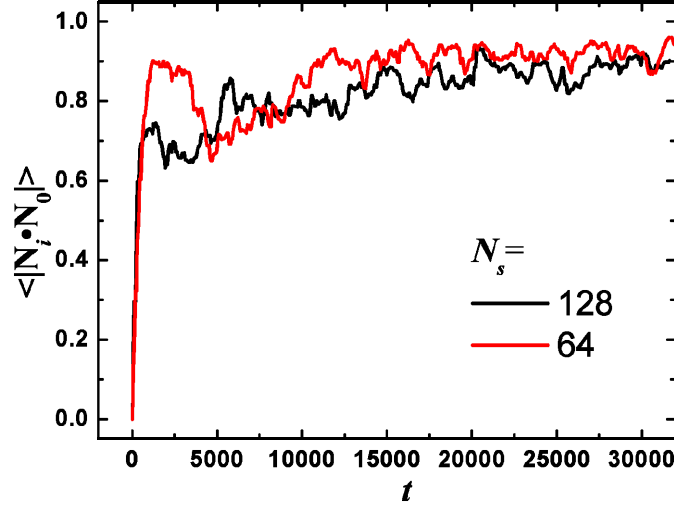
Figure 6.12: The dot product of normal vectors of beating plane and substrate $\langle \mathbf{n}_s \cdot \mathbf{n}_0 \rangle$.

6.4.2 Angle between substrate and beating plane

We define the normal vector of the plane of the substrate $\mathbf{N}_0 = (0,0,1)^T$. If the beating plane of the i-th sperm is parallel to the substrate, $|\mathbf{N}_i \cdot \mathbf{N}_0| = 1$.

Fig. 6.12 shows the evolution of $\langle |\mathbf{N}_i \cdot \mathbf{N}_0| \rangle$ as a function of time. The value of $\langle |\mathbf{N}_i \cdot \mathbf{N}_0| \rangle$ is zero at beginning, because the beating plane is perpendicular to the substrates as the initial state. Once the sperm start swimming, $\langle |\mathbf{N}_i \cdot \mathbf{N}_0| \rangle$ increases very fast. In both systems for $N_s = 64$ and $N_s = 128$, $\langle |\mathbf{N}_i \cdot \mathbf{N}_0| \rangle$ increases from 0 to more than 0.7 within $\Delta t = 1500$. Such a large increasing means that, the average rotation angle for sperm is more than 45° during the first 20 beats. This is much faster than the rotation
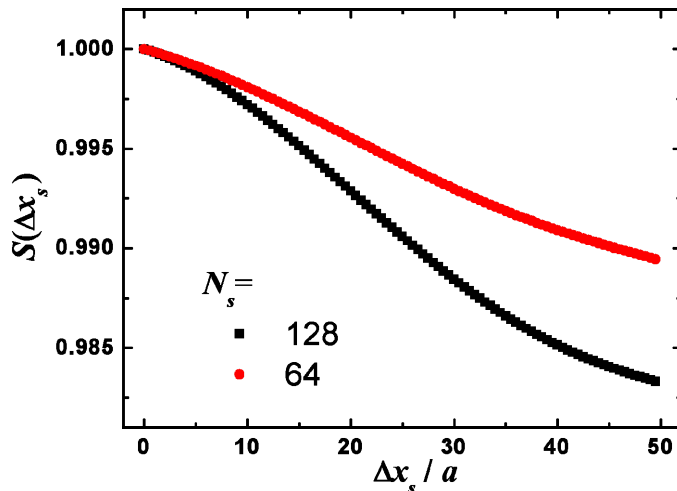
Figure 6.11: The correlation function S between the normal vectors of two segments at distance Δx_i on same flagellum. N_s is the total number of sperm in the simulation.

caused by the thermal diffusion. It is induced by two effects from HI.

The first is the HI with substrates. The sperm are confined in a small space that HI with the substrate is strong. In a single flagellum simulation with the same distance between substrates, HI with substrates rotates the flagellum quickly. This effect exists in the multi-sperm simulations also.

The second effect is the synchronization effect between sperm. In order to get lock in phase, the sperm not only shift their relative position as in 2D simulations, but also rotates to decrease the distance between their beating planes.

After the fast rotation at beginning, $<|\mathbf{N}_i \cdot \mathbf{N}_0|>$increases slowly with fluctuations and approaches to a none-zero value. In Fig. 6.12, the limit value of $<|\mathbf{n}_i \cdot \mathbf{n}_0|>$ for 64-sperm system is higher than of 128-sperm system. The higher sperm density makes a larger average angle between beating planes and substrates.

6.4.3 Aggregation towards the substrates

The average distance $<d_{sub}>$ between the sperm head and the nearest substrate is shown in Fig. 6.13 as a function of time t. In the 64-sperm system, all the sperm are initially at the position $z=15a$ with equal distance to each substrate. Thus $<d_{sub}>$ for 64-sperm system is $15a$ at $t=0$. In the 128-sperm system, due to not enough space to put all sperm at center of the simulation box, half of sperm are put at $z=10a$ and another half at $z=20a$. Thus, $<d_{sub}>$ for 128-sperm system is $10a$ at $t=0$.

In 128-sperm system, $<d_{sub}>$ increases at beginning. The hydrodynamic attraction between sperm pulls them to aggregate. In a long-time term, $<d_{sub}>$ for both systems decreases. The sperm move towards the substrates and aggregate at the hard walls. The decreasing of $<d_{sub}>$ in higher sperm density system is slower than in a lower density system. However, $<d_{sub}>$ is still decreasing in our simulation time. Thus, after about 500 beats, our system has not yet reached the stationary state yet.
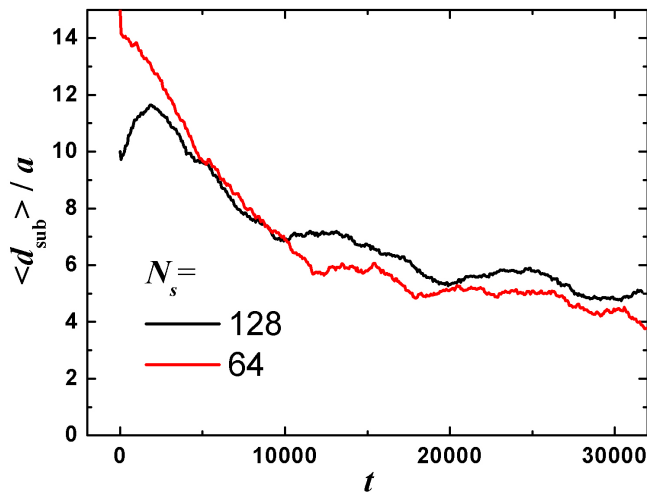
X

Figure 6.13: The average distance $<d_{sub}>$ between sperm head and the nearest substrate
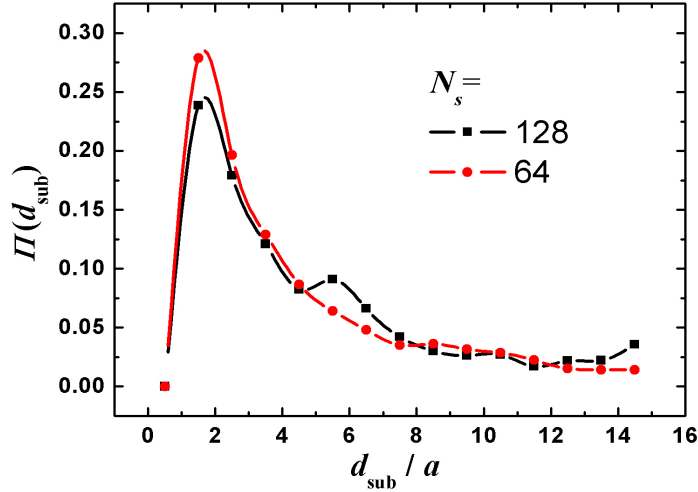
Figure 6.14: The distribution of the distance d_{sub} between the sperm head and the nearest substrate.

The aggregation at the substrate is also revealed by the probability density function of d_{sub}, as shown in Fig. 6.14. The distribution has a peak at the radius of the sperm head. Most of the sperm stay at the substrate with the head touch against the hard walls. Both systems have not yet reached the stationary state. The continually decreasing $<d_{sub}>$ with time indicates that the width of the distribution will decrease if we continue the simulation. The second peak at $d_{sub} \approx 6a$ for 128-sperm system is also probably due to the unbalanced system.

6.5 Discussion

We simulated the flagellum and sperm embedded in 3D MPC fluid. For multi-sperm systems, we employ hard walls in our simulation for the reason of saving computational labor. Also, in experiments, there are usually experimental boundaries such as glass containers.

Our simulation is different from realistic for several aspects. First, the Reynolds number is on the same order for nematodes in water, but is still higher than that for sperm. Second, we do not consider any mechanism to change the beat frequency and phase to cope with the hydrodynamics. Third, in experiments, especially for sperm, the fluid is usually a visco-elastic medium rather than a viscous one. The fluid has a memory of last moment due to the elasticity property raised from macro-molecule buffers.

Although our simulation model has a few detail differences from reality, there are still plenty of hints for us to understand the complicated experimental phenomenon.

First, the single sperm behavior strongly depends on the wave number on tail. By keeping all other parameters but decreasing the wave number, the curvature of the trajectory increases until the cell can only jiggle in a localized region.

Second, although not as strong as in 2D, HI between sinusoidal beating flagella –

synchronization and attraction – is still adequate to make cooperating clusters. Also, the synchronized state can be reached not only by shift the relative position, but also by rotating the beating planes.

Third, the hard substrates influence the behavior of flagella and sperm. HI between walls and flagella draws the beating planes to be parallel to wall, and helps the aggregation of swimmers at the substrates. However, our simulation time is not long enough yet to see if the walls can collect all sperm.

Thus we guess the sea-urchin sperm experiment [32], in which all sperm are condensed near substrate and form vortices, must have even strong confinements to force a high density of sperm at the substrate. Then the sperm are extensively confined in a quasi-2D space, vortices are direct consequence of curved rSPP as indicated in our 2D simulation.

Anyhow, our 3D simulation is just a trial for future works. Although the behavior in 3D is more complicated then in 2D, but it shows a promising prospect. Simulations with larger systems to observe the swarming behavior in bulk and under confinements is our next step.

VIII. Summary

We have analyzed the swarm behavior of rod-like swimmers propelled by a sinusoidal beating motion, such as nematodes and sperm, in a low-Reynolds-number fluid environment. The hydrodynamic interaction between swimmers is simulated by the multi-particle-collision dynamics (MPC) method, which is a particle-based meso-scopic simulation method for fluid dynamics. We also perform the simulations with anisotropic frictions (AF), which is a first order approximation of hydrodynamics, neglecting hydrodynamic interactions between swimmers. By comparing the results in a MPC fluid and with AF, the hydrodynamic interaction is shown to be very important for the aggregation and clustering behavior of these swimmers.

The side length of the simulation boxes must be several times of the characteristic length of the system, such as the length of swimmers, to avoid finite-size effects. From a simulation viewpoint, sperm swimming in a two-dimensional fluid is a less demanding problem than in three dimensions, and allow much more detailed studies of cooperative behaviors. In addition, sperm and nematodes in experiments usually swim in a quasi-two-dimensional space due to aggregation at the surfaces. Thus we focus on simulations in two dimensions.

The swimmers are simplified as straight rods with a constant propelling-force along the extended directions. The hydrodynamics is approximated as AF. A white-noise force as environmental noise is applied to rods, while the thermal fluctuation is neglected.

Without any attractive potentials, the system of self-propelled rods exhibits aggregation behavior. The volume exclusion between rods acts as the aligning mechanism, so that the rods are aligned by collision and aggregate into clusters. Started from a random initial state, the system reaches a stationary state when the rate of cluster formation is balanced by the break-up rate.

Three types of cluster size distribution functions with different shape are found at different density and environmental noise regions. Different distribution functions correspond to different cluster configurations in the system. With low rod density and strong environmental noise, the clusters are motile ones with all rods polarized in the same cluster; with high density and weak noise, giant and immobile clusters consisting of blocked rods are found. Quantities directly related to the PDF, such as average cluster size and weight, change with the rod density and the environmental noise. Especially, the average cluster size shows a power-law relation with the variance of environmental noise if the system starts with a disordered state. Giant density fluctuations, which are a characteristic fingerprint of aggregating systems of

self-propelled particles, are also found in our rod simulation.

A flagellum has a wave propagating on its rod-like structure, thus propels itself though fluid medium. The flagella have different beating frequencies, because in nature, sperm and nematodes can have a wide distribution of beat frequencies. The frequency distribution can be considered as noise due to internal property.

The main difference between rods and flagella is that the sinusoidal beating induces hydrodynamic synchronization and attraction between flagella. With small variance of frequency distribution, the hydrodynamic effects make the flagella in the same cluster tightly packed and locked in phase. The clusters extend strongly in the direction of motion, and the probability to find small clusters is decreased. However, with large variance of frequency distribution, hydrodynamic interaction between clusters also acts as an environmental background noise to break up clusters.

The swarming behavior of sinusoidal undulating flagella is very similar as the self-propelled rods. In order to separate the contributions of volume exclusion between the rod-like body and the hydrodynamic interaction between the sinusoidal beating motions, we compare the swarming behavior of flagella in a MPC fluid and with AF, separately.

Since the flagellum has a rod-like structure, the volume exclusion in two dimensions is still the most important mechanism to align the swimmers and raise the swarming behavior. The power-law distribution functions of cluster size, and the power-law dependence of average cluster size on the diversity of beating frequencies, are the same as we found in rod simulations.

Although hydrodynamic interaction is not the essential reason for swarm behavior, it has a strong effect on the cluster configurations. Hydrodynamic interaction between flagella in different clusters acts as the environmental background noise. However, the synchronization and attraction due to hydrodynamic interactions make the flagella in the same cluster tightly packed and locked in phase, if the deviation of frequencies is not large. The large clusters in MPC fluid extend in the moving direction, while the clusters without hydrodynamic interactions in anisotropic friction simulations show more compact structures. A huge cluster in MPC fluid looks like a motile "train" with all its components aligned in the same direction. Due to their large scattering sections and the strong flow field created by them, the "train" clusters collect the nearby small clusters. Thus the probability to find small clusters is decreased, and the average cluster size increases. On the other hand, the blocked structure of huge, immobile cluster is prevented by hydrodynamic interactions.

The difference between a flagellum and a sperm is the large head added in the front. The head generates strong viscous resistance, so that the beat shape of tail is modified and the sperm velocity is lower than of a single flagellum.

Although the head make the swimming more difficult, the hydrodynamic interaction – synchronization and attraction - between sinusoidal beating tails is still dominating in two dimensions. The swarming behavior of a multi-sperm system is the same as a multi-flagellum system. However, the heads of large diameters make the cluster configuration much looser, thus the stability of a large cluster is decreased.

From our two-dimensional simulations, we conclude that the fundamental elements for the swarming behavior of the active particles with sinusoidal configurations are the rod-like shape and the self-propelled motion. The volume exclusion in two dimensions is a strong mechanism to induce the alignment. The hydrodynamic interaction raised by the beating motion regulates the shape of the clusters and the distribution function of cluster size.

The swimming behaviors in three dimensions are much more complicated than in two dimensions. The sperm behavior strongly depends on the elasticity and the wave number of the tail. The effect of volume exclusion is much weaker, but the hydrodynamic interaction still plays an important role.

The hydrodynamic attraction between beating flagella and a hard substrate help the aggregation in confinement. A single flagellum at a substrate has a thrust towards the wall with its end lifted by the viscous force from the wall.

The hydrodynamic interaction between beating flagella – synchronization and attraction – is still strong enough in 3D to make cooperating clusters. The flagella can get phase locked through different pathways - shifting the relative position as the synchronization process in two dimensions, and rotating the beating planes. The existence of a not-too-large head does not destroy the cooperation between flagella. However, the cooperation in three dimensions is not as stable as in two dimensions, because a strong distortion of the tail and the higher collision rate during cooperation can easily separate a pair of swimmers. Our simulations in 3D show a rotation motion of beating planes, a three-dimensional package of swimmers in a cluster, and mass transport between the two walls in a slit geometry. Simulations with larger systems to observe the swarming behavior in bulk and under confinement are needed in the future.

Our results are in good agreements with the swarming of sperm and nematodes in a thin layer of fluid medium near surfaces. Some interesting experimental phenomena are reproduced. The coordinated movement of an aggregate of nematodes when on a damp surface of glass [12], as well as the huge "train" structure containing hundreds to thousands of rodent sperm at surface [37], have a similar extended and synchronized structure as we found in flagella simulations in a MPC fluid. Since the cluster size decreases with increasing variance of frequency distribution of flagella, our results are consistent with the experimental observation that if the rodent sperm

are hyperactivated, which is an abnormal beat mode, or if some sperm are dead, the clusters fall apart. The vortices arrays of sea-urchin sperm near a substrate is reproduced by curved flagella simulations with AF.

However, there are few reports on the hydrodynamic cooperation and swarm behavior of sinusoidal beating swimmers so far because research was focused on the behavior and motion mechanisms of single sperm, diluted thousands or even more times than their original concentration in vivo. At a really low density of moving agents, according to our simulation results, the cooperation is very weak.

Acknowledgements

Bibliography

[1] E. M. Purcell, *Am. J. Phys.* **45**, 3 (1977). *Life at Low Reynolds-Number.*

[2] P. Nelson, W. H. Freemann & Company (2003). *Biological Physics: Energy, Information, Life.*

[3] S. Nasseri and N. Phan-Thien, *Comp. Mech.* **20**, 551 (1997). *Hydrodynamic Interaction between Two Nearby Swimming Micromachines.*

[4] T. Ishikawa and M. Hota, *J. Exp. Biol.* **209**, 4452 (2006). *Interaction of Two Swimming Paramecia.*

[5] M. Kim, J. Bird, A. J. van Parys, K. S. Breuer and T. R. Powers, *Proc. Natl. Acad. Sci. U.S.A.* **100**, 15481 (2003). *A Macroscopic Scale Model of Bacterial Flagellar Bundling.*

[6] M. J. Kim and T. R. Powers, *Phys. Rev. E.* **69**, 061910 (2004). *Hydrodynamic Interactions Between Rotating Helices.*

[7] M. Reichert and H. Stark, *Eur. Phys. J. E* **17**, 493 (2005). *Synchronization of Rotating Helices by Hydrodynamic Inteactions.*

[8] E. Gauger and H. Stark, *Phys. Rev. E* **74**, 021907 (2006). *Numerical Study of a Microscopic Artificial Swimmer.*

[9] E. E. Keaveny and M. R. Maxey, *Phys. Rev. E* **77**, 041910 (2008). *Interactions between Comoving Magnetic Microswimmers.*

[10] A. Najafi and R. Golestanian, *Phys. Rev. E.* **69**, 062901 (2004). *Simple Swimmer at Low Reynolds Number: Three Linked Spheres.*

[11] C. M. Pooley, G. P. Alexander and J. M. Yeomans, *Phys. Rev. Lett.* **99**, 228103 (2007). *Hydrodynamic Interaction between Two Swimmers at Low Reynolds Number.*

[12] J. Gray and H. W. Lissmann, *J. Exp. Biol.* **41**, 135 (1964). *The Locomotion of Nematodes.*

[13] S. Camalet, F. Jülicher, and J. Prost, *Phys. Rev. Lett.* **82**, 1590 (1999). *Self-Organized Beating and Swimming of Internally Driven Filaments.*

[14] C. J. Brokaw, *Math. Method Appl. Sci.* **24**, 1351 (2001). *Simulating the Effects of Fluid Viscosity on the Behaviour of Sperm Flagella.*

[15] L. J. Fauci and A. McDonald, *Bull. Math. Biol.* **57**, 679 (1995). *Sperm Motility in the Presence of Boundaries.*

[16] G. I. Taylor, *Proc. Roy. Soc. Ser. A.* **209**, 447 (1951). *Analysis of the Swimming of Microscopic Organisms.*

[17] L. Rothschild, *Nature* **198**, 1221 (1963). *Non-Random Distribution of Bull Spermatozoa in a Drop of Sperm Suspension.*

[18] A. P. Berke, L. Turner, H. C. Berg and E. Lauga, *Phys. Rev. Lett.* **101**, 038102 (2008). *Hydrodynamic Attraction of Swimming Microorganisms by Surfaces.*

[19] D. M. Woolley, *Reprod.* **126**, 259 (2003). *Motility of Spermatozoa at Surfaces.*

[20] J. Elgeti, Ph.D. thesis. *Sperm and Cilia Dynamics*, Universität zu Köln (2007).

[21] T. Vicsek, *Nature* **441**, 421 (2001). *A Question of Scale.*

[22] S. Immler, H. D. M. Moore, W. G. Breed and T. R. Birkhead, *PLos One* **2**, e170 (2007). *By Hook or by Crook? Morphometry, Competition and Cooperation in Rodent Sperm.*

[23] H. D. M. Moore, K. Dvořáková, N. Jenkins and W. G. Breed, *Nature* **418**, 174 (2002). *Exceptional Sperm Cooperation in the Wood Mouse.*

[24] A. Baskaran and M. C. Marchetti, *Phys. Rev. Lett.* **101**, 268101 (2008). *Enhanced diffusion and ordering of self-propelled rods.*

[25] F. Peruani, A. Deutsch, and M. Bär, *Phys. Rev. E* **74**, 030904(R) (2006). *Nonequilibium Clustering of Self-Propelled Rods.*

[26] D. Saintillan and M. J. Shelley, *Phys. Rev. Lett.* **99**, 058102 (2007). *Orientational Order and Instabilities in Suspensions of Self-Locomoting Rods.*

[27] J. Gray, *J. Exp. Biol.* **32**, 775-800 (1955). *The Movement of Sea-Urchin Spermatozoa.*

[28] H. C. Fu, T. R. Powers and C. W. Wolgemuth, *Phys. Rev. Lett.* **99**, 258101 (2007). *Theory of Swimming Filaments in Viscoelastic Media.*

[29] J. Gray and G. J. Hancock, *J. Exp. Biol.* **32**, 802 (1955). *The Propulsion of Sea-Urchin Spermatozoa.*

[30] L. J. Fauci and R. Dillon, *Annu. Rev. Fluid Mech.* **38**, 371 (2006). *Biofluidmechanics of Reproduction.*

[31] L. J. Fauci, *J. Comp. Phys.* **86**, 294 (1990). *Interaction of Oscillating Filaments – A Computational Study.*

[32] I. H. Riedel, K. Kruse and J. Howard, *Science* **309**, 300(2005). *A Self-Organized Vortex Array of Hydrodynamically Entrained Sperm Cells.*

[33] R. Trivers, *Benjamin Cummings, California* (1985). *Social Evolution.*

[34] J. Sivinski, *In Sperm Competition and the Evolution of Animal Mating Systems* (ed. R. L. Smith) 223-249 (Academic, Orlando, 1984)

[35] F. Hayashi, *Functional Ecology* **12**, 347 (1998). *Sperm Co-Operation in the Fishfly, Parachauliodes Japonicus.*

[36] F. Hayashi, *J. Insect Physiol.* **42**, 859 (1996). *Insemination Through an Externally Attached Spermatophore: Bundled Sperm and Post-Copulatory Mate Guarding by Male Fishflies (Megaloptera: Corydalidae)*

[37] H. D. M. Moore and D. A. Taggart, *Biology of Reproduction* **52**, 947 (1995). *Sperm Pairing in the Opossum Increases the Efficiency of Sperm Movement in a*

Viscous Environment.

[38] I. Farkas, D. Helbing and T. Vicsek, *Nature* **419**, 131 (2002). *Mexican waves in an excitable medium.*

[39] D. Helbing, I. Farkas and T. Vicsek, *Nature* **407**, 487 (2000). *Simulating Dynamical Feaures of Escape Panic.*

[40] Z. Néda, E. Ravasz, Y. Brechet, T. Vicsek, A.-L. Barabási, *Nature* **403**, 849 (2000). *The sound of many hands clapping.*

[41] J. T. Bonner, *Proc. Natl. Acad. Sci. USA* **95**, 9355 (1998). *A way of following individual cells in the migrating slugs of Dictyostelium Discoideum.*

[42] E. Ben-Jacob, I. Cohen and H. Levine, *Advances in Physics* **49**, 395 (2000). *Cooperative Self-Organism of Microorganisms.*

[43] A. Kudrolli, G. Lumay, D. Volfson and L. S. Tsimring, *Phys. Rev. Lett.* **100**, 058001 (2008). *Swarming and Swirling in Self-Propelled Polar Granular Rods.*

[44] V. Narayan, S. Ramaswamy and N. Menon, *Science* **317**, 105 (2007). *Long-Lived Giant Number Fluctuations in a Swarming Granular Nematic.*

[45] B. Szabó, G. J.Szöllösi, B. Gönci, Zs, Jurányi, D. Selmeczi and T. Vicsek, *Phys. Rev. E* **74**, 061908 (2006). *Phase transition in the collective migration of tissue cells: Experiment and model.*

[46] J. Toner and Y. Tu, *Phys. Rev. Lett.* **75**, 4326 (1995). *Long-range order in a two-dimensional dynamical XY model: How birds fly together.*

[47] H. J. Bussemaker, A. Deutsch and E. Geigant, *Phys. Rev. Lett.* **78**, 5018 (1997). *Mean-field analysis of a dynamical phase transition in a cellular automaton model for collective motion.*

[48] F. Peruani, A. Deutsch, and M. Bär, *Eur. Phys. J. Special Topics* **157**, 111 (2008). *A mean-field theory for self-propelled particles interacting by velocity alignment mechanisms.*

[49] H. Chaté, F. Ginelli, G. Grégoire and F. Raynaud, *Phys. Rev. E* **77**, 046113 (2008). Collective motion of self-propelled particles interacting without cohesion.

[50] U. Erdmann, W. Ebeling and A. S. Mikhailov, *Phys. Rev. E* **71**, 051904 (2008). *Noise-induced transition from translational to rotational motion of swarms.*

[51] E. Forgoston and I. B. Schwartz, *Phys. Rev. E* **77**, 035203(R) (2008). *Delay-induced instabilities in self-propelling swarms.*

[52] G. Grégoire, H. Chaté and Y. Tu, *Physica D* **181**, 157 (2003). *Moving and staying together without a leader.*

[53] G. Grégoire and H. Chaté, *Phys. Rev. Lett.* **92**, 025702 (2004). *Onset of Collective and Cohesive Motion.*

[54] J. P. Hernandez-Ortiz, C. G. Stoltz and M. D. Graham, *Phys. Rev. Lett.* **95**,

204501 (2005). *Transport and collective dynamics in suspensions of confined swimming particles.*

[55] C. Huepe and M. Aldana, *Phys. Rev. Lett.* **92**, 168701 (2004). *Intermittency and Clustering in a System of Self-Driven Particles.*

[56] C. Huepe and M. Aldana, *Physica A* **387**, 2809 (2008). *New tools for characterizing swarming systems: a comparison of minimal models.*

[57] I. Llopis and I. Pagonabarraga, *Europhys. Lett.* **75**, 999 (2006). *Dynamic regimes of hydrodynamically coupled self-propelling particles.*

[58] T. Vicsek, A. Czirok, E. Ben-Jacob, I. Cohen and O. Shochet, *Phys. Rev. Lett.* **75**, 1226 (1995). *Novel Type of Phase Transition in a System of Self-Driven Particles.*

[59] A. Czirók, E. Ben-Jacob, I. Cohen and T. Vicsek, *Phys. Rev. E* **54**, 1791 (1996). *Formation of Complex Bacterial Colonies via Self-Generated Vortices.*

[60] C. Dombrowski, L. Cisneros, S. Chatkaew, R. E. Goldstein and J. O. Kessler, *Phys. Rev. Lett.* **93**, 098103 (2004). *Self-Concentration and Large-Scale Coherence in Bacterial Dynamics.*

[61] A. Sokolov, I. S. Aranson, J. O. Kessler and R. E. Goldstein, *Phys. Rev. Lett.* **98**, 158102 (2007). *Concentration Dependence of the Collective Dynamics of Swimming Bacteria.*

[62] X.-L. Wu and A. Libchaber, *Phys. Rev. Lett.* **84**, 3017 (2000). *Particle Diffusion in a Quasi-Two-Dimensional Bacterial Bath*; G. Grégoire, H. Chaté and Y.-H. Tu, *Phys. Rev. Lett.* **86**, 556 (2001); X.-L. Wu and A. Libchaber, *Phys. Rev. Lett.* **86**, 557 (2001).

[63] Y. Yang, J. Elgeti and G. Gompper, *Phys. Rev. E* **78**, 061903 (2008). *Cooperation of Sperm in Two Dimensions: Synchronization, Attraction, and Aggregation through Hydrodynamic Interactions.*

[64] P. Kraikivski, R. Lipowsky and J. Kierfeld, *Phys. Rev. Lett.* **96**, 258103 (2006). *Enhanced Ordering of Interacting Filaments by Molecular Motor.*

[65] H. H. Wensink and H. Löwen, *Phys. Rev. E* **78**, 031409 (2008). *Aggregation of Self-Propelled Colloidal Rods Near Confining Walls.*

[66] O. A. Igoshin, R. Welch, D. Kaiser and G. Oster, *Proc. Natl. Acad. Sci. U.S.A.* **101**, 4256 (2004). *Wave and Aggregation Paterns in Myxobacteria.*

[67] E. Ben-Jacob, O. Schochet, A. Tenenbaum, I. Cohen, A. Czirók and T. Vicsek, *Nature* **368**, 46 (1994). *Generic Modelling of Cooperative Growth Patterns in Bacterial Colonies.*

[68] M. S. Alber, M. A. Kiskowski and Y. Jiang, *Phys. Rev. Lett.* **93**, 068102 (2004). *Two-Stage Aggregate Formation via Streams in Myxobacteria.*

[69] J. M. Kuner and D. Kaiser, *J. Bacteriol.* **151**, 458 (1982). *Fruiting Body*

Morphogenesis in Submerged Cultures of Myxococcus xanthus.

[70] M. Aldana, V. Dossetti, C. Huepe, V. M. Kenkre and H. Larralde, *Phys. Rev. Lett.* **98**, 095702 (2007). *Phase Transitions in Systems of Self-Propelled Agents and Related Network Models.*

[71] H. Chaté, F. Ginelli and R. Montagne, *Phys. Rev. Lett.* **96**, 180602 (2006). *Simple Model for Active Nematics: Quasi-Long-Range Order and Giant Fluctuations.*

[72] R. Kapral, *Adv. Chem. Phys.* **140**, 89 (2008). *Multiparticle collision dynamics : Simulation of Complex Systems on Mesoscales.*

[73] G. Gompper, T. Ihle, D. M. Kroll and R. G. Winkler, *Adv. Polym. Sci.* **221**, 1 (2009). *Multi-Particle Collision Dynamics: A Particle-Based Mesoscale Simulation Approach to the Hydrodynamics of Complex Fluids.*

[74] A. Lamura, G. Gompper, T. Ihle and D. M. Kroll, *Europhys. Lett.* **56**, 319 (2001). *Multi-Particle Collision Dynamics: Flow around a Circular and a Square Cylinder.*

[75] M. Ripoll, K. Mussawisade, R. G. Winkler and G. Gompper, *Europhys. Lett.* **68**, 106 (2004). *Low-Reynolds-Number Hydrodynamics of Complex Fluids by Multi-Particle-Collision Dynamics.*

[76] J. Elgeti and G. Gompper, *NIC proceedings*, Vol. **39** of NIC series, edited by G. Münster, D. Wolf, and M. Kremer, pp. 53-61 (2008).

[77] L. D. Landau and E. M. Lifschitz, Pergamon Press (1987). *Fluid Mechanics.*

[78] A. Malevanets and R. Kapral, *J. Chem. Phys.* **110**, 8605 (1999). *Mesoscopic Model for Solvent Dynamics.*

[79] A. Malevanets and R. Kapral, *J. Chem. Phys.* **112**, 7260 (2000). *Solute Molecular Dynamics in a Mesoscale Solvent.*

[80] E. Tüzel, M. Strauss, T. Ihle and D. M. Kroll, *Phys. Rev. E.* **68**, 036701 (2003). *Transport Coefficients for Stochastic Rotation Dynamics in Three Dimensions.*

[81] E. Allahyarov and G. Gompper, *Phys. Rev. E* **66**, 036702 (2002). *Mesoscopic Solvent Simulations: Multiparticle-Collision Dynamics of Three-Dimensional Flows.*

[82] T. Ihle and D. M. Kroll, *Phys. Rev. E* **63**, 020201(R) (2001). *Stochastic rotation dynamics: A Galilean-Invariant Mesoscopic Model for Fluid Flow.*

[83] T. Ihle and D. M. Kroll, *Phys. Rev. E* **67**, 066705 (2003). *Stochastic Rotation Dynamics. I. Formalism, Galilean Invariance, and Green-Kubo Relations.*

[84] N. Kikuchi, C. M. Pooley, J. F. Ryder and J. M. Yeomans, *J. Chem. Phys.* **119**, 6388 (2003). *Transport Coefficients of a Mesoscopic Fluid Dynamics Model.*

[85] R. P. Burchard, *Ann. Rev. Microbiol.* **35**, 497 (1981). *Gliding Motility of Prokaryotes: Ultrastructure, Physiology, and Genetics.*

[86] J. Gray, *J. Exp. Biol.* **35**, 96 (1957). *The movement of the Spermatozoa of the Bull.*

[87] I. H. Riedel-Kruse, A. Hilfinger, J. Howard and Frank Jülicher, *HFSP*, **1**, 192 (2007). *How Molecular Motors Shape the Flagellar Beat.*

[88] M. Ripoll, K. Mussawisade, R. G. Winkler and G. Gompper, *Phys. Rev. E* **72**, 016701 (2005). *Dynamic Regimes of Fluids Simulated by Multiparticle-Collision Dynamics.*

[89] A. Czirók, H. E. Stanley and T. Vicsek, *J. Phys. A: Math. Gen.* **30**, 1375 (1997). *Spontaneously ordered motion of self-propelled particles.*

[90] B. M. Friedrich and F. Jülicher, *Proc. Natl. Acad. Sci. USA* **104**, 13256 (2007). *Chemotaxis of sperm cells.*

[91] T. Strunker, I. Weyand, W. Bonigk, Q. Van, A. Loogen, J. E. Brown, N. Kashikar, V. Hagen, E. Krause, and U. B. Kaupp, *Nature Cell Biol.* **8**, 1149 (2006). *A K+-Selective cGMP-gated Ion Channel Controls Chemosensation of Sperm.*

[92] The temperature in the human sperm experiment was about 35-37°C. The pictures were taken by fluorescence microscopy. The sperm was loaded with Fluo4 (concentration 10 millimole per liter), a calcium indicator. The measurement stage was moved to keep the swimming sperm in the field of view.

[93] We thank U. Benjamin Kaupp, Luis Alvarez (CAESAR Bonn), and Luru Dai (INB-1, Research Center Jülich) for stimulating discussions and sharing of their experimental data.

[94] See EPAPS Document No. E-PLEEE8-78-0818111 for movies of the dynamics of cluster formation and breakup in the stationary state. For more information on EPAPS, see http://www.aip.org/pubservs/epaps.html.

[95] K. Mussawisade, M. Ripoll, R. G. Winkler and G. Gompper, *J. Chem. Phys.* **123**, 144905 (2005). *Dynamics of Polymers in a Particle-Based Mesoscopic Solvent.*

[96] G. J. Elfring and E. Lauga, arXiv:0907.0962 (2009). *Hydrodynamic phase-locking of swimming microorganisms.*

[97] D. F. Evans and H. Wennerström, Wiley-vch Verlag Gmbh (1999). *The Colloidal Domain: Where Physics, Chemistry, Biology, and Technology Meet.*

Abbreviations and variable symbols used in thesis

Abbreviations

2D, 3D   two dimension, three dimensions

MPC   Multi-Particle Collision Dynamics

HI   hydrodynamic interaction

VE   volume exclusion

SPP   self-propelled particles

rSPP   rod-like self-propelled particles, self-propelled rods

Navier-Stokes equation

∇ gradient operator

ρ fluid density

η dynamic viscosity

$\mathbf{v}$ flow velocity

υ velocity of the main stream

p pressure

$\mathbf{f}_{\text{ext}}$ body forces per unit volume acting on the fluid

l a typical length of the system

Re   Reynolds number

MPC variables and parameters

a length unit of MPC method

t time

m mass of MPC solvent partiles

ρ average solvent particle number in each box of MPC fluid

$\mathbf{r}_i$ space position of the i-th MPC solvent particle

$\mathbf{u}_i$ velocity of the i-th MPC solvent particle

$\mathbf{u}_{\text{cm},j}$ center of mass velocity of the j-th box in MPC method

$k_B T$ temperature

v_{kin} kinetic viscosity

v_{coll} collision viscosity

α the rotation angle of MPC method

$\mathcal{R}_j(\alpha)$ the rotation maxtrix of j-th box which rotate a vector by an angle α around a direction

h rescaled mean free path of MPC solvent particles

$\Delta\tau$ collision time (time step) of MPC method

Simulation variables and parameters

v	velocity of particle
$\Delta\tau'$	molecular-dynamics time step
ε	the constant in Leonard-Jones potential
γ	friction coefficient
ξ	white noise
c	curvature
k	spring constant
κ	bending rigidity constant
F	force
M	torque
$\mathbf{R}_i$	the bond vector connecting particle i and $(i+1)$

System parameters

S	simulation box size
N	total particle (rod, flagellum or sperm) number of simulation system
N_{tail}	the number of monomers on a sperm tail
L_r	length of rods
L_f	length of flagella
L_s	length of sperm tails
ρ_r	the number density of rods
ρ_c	the number density of clusters
ρ_f	the number density of flagella
σ^2	the variance of the environmental noise in the rSPP simulations
f	beating frequency
σ_f	dimensionless variance of the distribution of beating frequencies
T	total simulation time
φ	initial phase of beating

Analyzed variables and quantities

$T_{\text{life}}(n)$	average life time of clusters of size n
β	the exponent of cluster distribution function
β_{dens}	the exponent of density deviation $\Delta N \sim \lambda^{\beta_{\text{dens}}}$ where λ is the anticipated particle number
β_{life}	the exponent of the power-law part of $T_{\text{life}}(n)$
Π	number density function or probability density function
P	energy consumption
$<n>$	average cluster size

$\bar{n}$	stationary average cluster size
$<w>$	average cluster weight
$\bar{w}$	stationary average cluster weight
β'	the exponent of power law part of $T_{\text{life}}(n)$ for small cluster size
G	orientation correlation function
Δs	the displacement of the center-of-mass of a cluster
x_s	the position of a segment on the flagellum model, with x_s=0 for the first segment.

Others

ϕ	angle in the polar coordinate system
$K(i,j)$	coagulation kernel of Smoluchowski equation
$K_+(i,j)$	cluster formation rate of two clusters of size i and j to form a cluster of size $i+j$
$K_-(i,j)$	the spontaneous break-up rate for a cluster of size $i+j$ into two clusters of size i and j
Pe	Péclet number

Kurzzusammenfassung

Eine Vielzahl von Mikroorganismen und Zellen, wie zum Beispiel Spermien und einige Arten von Spulwürmern (Nematoden), schwimmen durch Flüssigkeit, indem sie mit ihrem stäbchenförmigen Körper sinusförmige Schlagbewegungen vollführen. Die Fortbewegung dieser mikroskopischen Schwimmer wird durch die Viskosität der Flüssigkeit dominiert, wärend ihre eigene Trägheit vernachlässigbar ist. Sie kooperieren miteinander über hydrodynamische Wechselwirkungen und zeigen ein komplexes Schwarmverhalten, wie zum Beispiel Anlagerung in der Nähe von Oberflächen und Clusterbildung bei hoher Dichte. Diese interessanten und überraschenden Phänomene deuten darauf hin, dass für die Schwimmer zusätzlich zu der individuellen Bewegung noch andere, auf Kooperation beruhende Möglichkeiten bestehen, große Strecken und Hindernisse zu überwinden um ihr Ziel zu erreichen. Insbesondere trifft dies auf Spermien zu, den wichtigsten Zellen in der Fortpflanzung höherer Tiere.

Das Ziel dieser Arbeit ist es, die Bedeutung von hydrodynamischen Wechselwirkungen und Volumenausschluss Effekten für die Kooperation und das schwarm-typische Verhalten von mikroskopischen Schwimmern wie Spermien und Nematoden zu erklären, die sinusförmige Schlagbewegungen als Antrieb nutzen. Diese Schwimmer können zusammengefasst als stäbchenförmige selbst-angetriebene Teilchen (rod-like self-propelled particles, rSPP) in einer viskosen Umgebung betrachtet werden. Wir vergleichen in Simulationen das Schwarmverhalten gerader stäbchenförmiger Teilchen mit solchen, welche sich durch sinusförmige Schläge fortbewegen. Die hydrodynamischen Wechselwirkungen zwischen den Schwimmern werden über multi-particle collision dynamics (MPC) simuliert, eine teilchenbasierte, mesoskopische Simulationsmethode für die Dynamik von Flüssigkeiten. Wir führen desweiteren Simulationen mit richtungsabhängigem Reibungskoeffizienten (anisotropic friction, AF) durch, als eine Näherung der Hydrodynamik, welche hydrodynamische Wechselwirkungen zwischen den Schwimmern vernachlässigt. Die Beiträge von hydrodynamischen Wechselwirkungen und Volumenausschluss können identifiziert werden, indem die Ergebnisse von MPC- und AF-Simulationen verglichen werden.

Wegen der Anlagerung an der Oberfläche schwimmen Spermien und Nematoden in einem quasi-zweidimensionalen Raum. Spermien in einer zweidimensionalen Flüssigkeit zu simulieren ist weniger aufwendig als in drei Dimensionen, und ermöglicht somit sehr viel detailliertere Untersuchungen des kooperativen Verhaltens. Daher haben wir uns auf zweidimensionale Simulationen konzentriert.

Der gegenseitige Volumenausschluss ist der Schlüsselfaktor für das Auftreten von kollektiver Ausrichtung und Clusterbildung von selbst angetriebenen Stäbchen in viskoser Umgebung in zwei Dimensionen. Zwei Arten von Clustern können beobachtet werden: Bei niedriger Stäbchendichte und starkem Umgebungsrauschen treten freibewegliche Cluster auf, in denen alle Stäbchen polarisiert sind, wärend bei hohen Dichten und schwachem Rauschen riesige, unbewegliche Cluster sich gegenseitig blockierender Stäbchen auftreten. Erreicht das System ein Gleichgewicht zwischen Clusterbildungsrate und -zerfallsrate, bildet sich eine stabile Verteilungsfunktion der Clustergröße heraus. Es werden drei verschiedene Verteilungsfunktionen unterschieden, die den drei Zuständen des Systems entsprechen. In Systemen mit freibeweglichen Clustern hat die Verteilungsfunktion immer einen Abschnitt, der einem Potenzgesetz folgt. Die durchschnittliche Clustergröße folgt einem Potenzgesetz des Umgebungsrauschens. Auch werden riesige Dichtefluktuationen in den Stäbchensimulationen gefunden, welche eine charakteristische Eigenschaft von Systemen aggregierender selbstangetriebener Teilchen sind.

Der Hauptunterschied zwischen selbstangetriebenen Stäbchen und Flagellum-Systemen ist, dass die sinusförmig schlagenden Flagellen sich über hydrodynamische Wechselwirkungen gegenseitig synchronisieren und anziehen. Diese hydrodynamischen Synchronisations- und Anziehungseffekte sorgen dafür, dass Flagellen innerhalb eines Clusters sehr dicht gepackt sind und die Phasen ihrer Schlagbewegung koppeln. Die Cluster sind in ihrer Bewegungsrichtung deutlich länger ausgedehnt, und die Häufigkeit kleiner Cluster ist gering. Die hydrodynamischen Wechselwirkungen zwischen den Clustern wirken als Hintergrundrauschen. Das Schwarmverhalten von sinusförmig schlagenden Flagellen gleicht im wesentlichen dem selbstangetriebener Stäbchen. Die Verteilungsfunktion der Clustergröße folgt einem Potenzgesetz. Natürliche Spermien und Nematoden können eine sehr breite Verteilung von Schlagfrequenzen aufweisen, was als durch innere Eigenschaften bestimmtes Rauschen angesehen werden kann. Die durchschnittliche Clustergröße folgt einem Potenzgesetz der Varianz der Verteilung der Schlagfrequenzen.

Ein Spermium ist ein sinusförmig schlagendes Flagellum mit einem Kopf an der Vorderseite. Obwohl die Köpfe starke viskose Reibungskräfte verursachen, dominieren weiterhin die hydrodynamischen Wechselwirkungen – Synchronisation und Anziehung – zwischen den schlagenden Flagellen. Auch das Schwarmverhalten eines System aus vielen Spermien gleicht dem aus Flagellen, wobei die Köpfe für eine sehr viel lockerere Bindung der Cluster sorgen, und somit deren Stabilität reduzieren.

Daher schlussfolgern wir, dass in zwei Dimensionen die anisotrope Form und die

selbstangetriebene Bewegung die grundlegenden Elemente des Schwarmverhaltens von aktiven stäbchenförmigen Teilchen wie Spermien und Nematoden sind. Der Volumenausschluss ist ein starker Mechanismus, der zu paralleler Ausrichtung führt. Die hydrodynamischen Wechselwirkungen aufgrund der sinusförmig schlagenden Bewegung bestimmen die Form der Cluster und die Verteilungsfunktion der Clustergrößen.

In drei Dimensionen ist die hydrodynamische Wechselwirkung noch immer stark genug um zu kooperierenden Clustern von Flagellen und Spermien zu führen. Die Flagellen können über unterschiedliche Abläufe synchronisiert werden – sie können ihre relative Position verschieben oder in ihrer Schlagebene rotieren. Dennoch ist die Kooperation in drei Dimensionen nicht so stabil wie in zwei Dimensionen.

Unsere Ergebnisse befinden sich in guter Übereinstimmung mit experimentellen Beobachtungen des Schwarmverhaltens von Spermien und Nematoden in einer dünnen Schicht einer Flüssigkeit nahe der Oberfläche. Interessante, experimentell zu beobachtenden Phänomene, wie die gestreckten Cluster von Maus-Spermien und die Wirbel von Seeigel-Spermien, werden reproduziert.

Erklärung

Ich versichere, dass ich die von mir vorgelegte Dissertation selbständig angefertigt, die benutzten Quellen und Hilfsmittel vollständig angegeben und die Stellen der Arbeit, einschließlich Tabellen, Karten und Abbildungen, die anderen Werken im Wortlaut oder dem Sinn nach entnommen sind, in jedem Einzelfall als Entlehnung kenntlich gemacht habe; dass diese Dissertation noch keiner anderen Fakultät order Universität zur Prüfung vorgelegen hat; dass sie – abgesehen von unten angegebenen Teilpublikationen – noch nicht veröffentlicht worden ist sowie, dass ich eine solche Veröffentlichung vor Abschluss des Promotionsverfahrens nicht vornehmen werde. Die Bestimmungen dieser Promotionsordnung sind mir bekannt. Die von mir vorgelegte Dissertation ist von Prof. Dr. G. Gompper betreut worden.

Curriculum Vitae

Yang, Yingzi

Personal Information

Gender: Female   **Birth Place:** Shanghai

Birth data: 18th May 1981

Address: Raderstr. 19, Jülich, Germany, D-52425

Tel: 0049-2461-612972   **Email:** yang.yingzi@gmail.com

Education

1996. 09 ~ 1999. 06	High School Affiliated to Fudan University
1999. 09 ~ 2003. 06	Bachelor on Physics, Department of Physics, Fudan University
2003. 09 ~ 2006. 06	Master on Macromolecular Chemistry and Physics, Department of Macromolecular Science, Fudan University Supervisor: Prof. Dr. Feng Qiu Title of thesis: "Theoretical studies on the morphologies and mechanical properties of asymmetric diblock copolymer thin films"
2006. 11 ~ present	Ph. D student, Theoretical Soft-Matter and Biophysics Group, Institute of Solid State Research (IFF), Research Center Jülich (FZJ)

Courses during PHD

2006. 11 ~ 2009. 11 International Helmholtz Research School on Biophysics and Soft Matter:

Lectures:
- Statistical Physics
- Molecules of Life – Introduction to the Chemistry and Biology of Cells
- Computer Simulations in Physics and Biology
- Introduction to Optical Microscopy
- Physical Chemistry of Polymers

Lab Course:
- Recording of Cell Activity

Student Seminar Presentation:
- 2007. 01. 07   "Semiflexible Polymer in Nanochannels"
- 2007. 11. 14   "Hydrodynamic or Non-hydrodynamic Effect? Cooperation in Sperm"

- 2008. 07   "Multi Sperm Behavior – Cooperative behavior in Sperm"
- 2008. 12   "Swarm Behavior of Self-Propelled Particles"

Spring school:
- 2008. 03. 03~14   Soft Matter – From Synthetic to Biological Materials, 39th IFF Spring School

Conferences Contributions

2008. 11. 11~14 Jülich Soft Matter Days (JSMD) 2009
Poster: "Cooperation of Sperm in Two Dimensions: Synchronization, Attraction and Aggregation through Hydrodynamic Interactions"

2009. 03. 18~20 Mesoscale Simulations of Soft Matter Out of Equilibrium (MESOSOFT)
Talk: "Multi-Sperm Behavior – Cooperative Behavior in Sperm"

2009. 05. 18~29 Spring School on Multiscale Methods and Modeling in Biophysics and System Biology, Shanghai, China
Poster: "Cooperation of Sinusoidal Beating Organisms: Synchronization, Attraction and Aggregation through Hydrodynamic Interactions"

Publications

[1] Y. Z. Yang, F. Qiu, H. D. Zhang, and Y. L. Yang, ACTA CHIMICA SINICA, 67(17), 1601-1606 (2004). Microphases of Asymmetric Diblock Copolymers in Confined Thin Films.

[2] Y. Z. Yang, F. Qiu, H. D. Zhang, and Y. L. Yang, POLYMER, **47**(6), 2205-2216 (2006). Cylindrical Phase of Diblock Copolymers Confined in Thin Films. A Real-Space Self-Consistent Field Theory Study.

[3] Y. Z. Yang, T. W. Burkhardt and G. Gompper, PHYSICAL REVIEW E, **76**(1), 011804 (2007). Free Energy and Extension of a Semiflexible Polymer in Cylindrical Confining Geometries.

[4] Y. Z. Yang, J. Elgeti and G. Gompper, PHYSICAL REVIEW E, **78**(6), 061903 (2008). Cooperation of Sperm in Two Dimensions: Synchronization, Attraction and Aggregation through Hydrodynamic Interactions.

[5] Y. Z. Yang and G. Gompper. Swarming Behavior of Sinusoidal Beating Flagella. (in preparation)

[6] Y. Z. Yang, V. Marceau and G. Gompper. Aggregation and Clustering of Self-Propelled Rods. (in preparation)